Politecnico di Torino

1859

Master of Science in Civil Engineering

Master's degree Thesis

Bond Behaviour in Corroded Prestressed Concrete Beams: Experimental and Numerical Study

Supervisor:
Prof. Francesco Tondolo

Co-supervisors:
Prof. Beatrice Belletti
Dr-Ing. Simone Ravasini

Candidate:
Mobin Faridian

October 2024

Acknowledgement

I would like to express my heartfelt gratitude to my supervisor, Prof. Francesco Tondolo, for his exceptional guidance, support, and mentorship throughout this journey. His invaluable expertise and encouragement have not only shaped the direction of this research but have also helped me grow in my academic career. For this, I am deeply thankful.

I would also like to extend my sincere appreciation to my co-supervisors, Prof. Beatrice Belletti and Dr.-Ing Simone Ravasini, for their insightful suggestions, constructive feedback, and constant willingness to assist whenever needed. Their contributions have greatly enriched this work, and I am truly grateful for your dedication and support.

Lastly, I owe a special thank you to my wife, Dr-Ing Aida Safabakhsh, whose love, understanding, and unwavering support have been my greatest source of strength during this process. Your belief in me and your constant encouragement have been essential in helping me navigate the challenges of this work. I am forever grateful for your presence in my life.

To all of you, I extend my deepest gratitude.

Abstract

The effect of corrosion on bond strength in strand-concrete interface in Prestressed Concrete (PC) beams is a critical factor influencing the structural performance and load-bearing capacity of these elements. This study presents the findings of an experimental campaign conducted at the laboratory of Politecnico di Torino, aimed at evaluating the bond behaviour and its impact on the load-bearing capacity and failure modes of naturally corroded Prestressed Concrete (PC) beams. The research focuses on three beam-end specimens extracted from a full-scale Prestressed Concrete beam, which had been in service for over a decade as part of a thermal power plant. During this period, the beam was subjected to repeated cycles of wetting and drying with marine water, leading to natural chloride-induced corrosion. Each beam-end specimen was tested sequentially until failure by setting proper boundary conditions, all of them triggering splitting failure mode. Following each test, the tested section was removed, and the remaining portion of the beam was prepared for subsequent testing. The testing procedure was displacement-controlled, and strain gauges, along with transducers, were used to monitor the strain and relative slip behaviour of the corroded prestressed strands under loading. Based on the data collected from these instruments during the test, bond strength at the strand-concrete interface and the corresponding slip was derived for the experimental case. Moreover, an analytical approach was employed to estimate the residual bond strength, considering the cross-sectional loss and reduced mechanical properties of the corroded strands, both of which were also estimated based on the residual prestress level of corroded strands. Besides, the bond strength for the uncorroded condition of the beam was estimated. Furthermore, Digital Image Correlation (DIC) techniques, utilizing high-resolution digital images and N_{corr} software, were employed to monitor vertical displacement at load application point and displacement distribution of both horizontal and vertical directions on the concrete surface and to detect crack initiation and propagation patterns as well as strain pattern at different load levels. Finally, Non-Linear Finite Element Analyses (NLFEA) were conducted using the PARC user subroutine in ABAQUS software to simulate the actual behaviour of the Prestressed Concrete (PC) beam under both uncorroded and corroded conditions. The results demonstrate a considerable reduction in bond strength in corroded Prestressed Concrete (PC) beams compared to uncorroded ones, with consequent decrease in the load-bearing capacity. Furthermore, the results of the Non-Linear Finite Element Analyses exhibited reasonable agreement with experimental and analytical approaches, by showing consistency with the experimental findings in terms of crack patterns and failure modes, which was splitting failure. Consequently, this research highlights the critical role of understanding bond behaviour at the strand-concrete interface in predicting the overall performance of Prestressed Concrete (PC) beams.

Contents

List of Figures

List of Tables

1 Introduction

1.1 Overview

Many existing structures and infrastructures have been constructed using reinforced concrete (RC) and prestressed concrete (PC). Therefore, durability and resistance capacity of these types of structures and infrastructures and the factors affecting their behaviour during service life have been of great importance in recent years. Thus, recognizing the factors deteriorating the existing structures and infrastructures and finding the most optimized way to maintain them against degradation have become a significant need. Corrosion of steel implemented in concrete has been known as one of the main factors reducing the ultimate and residual capacity and changing the failure mode of these structures. Corrosion has been impacting both economic and safety aspects of infrastructure and structures. In economic terms, corrosion of reinforced concrete (RC) and prestressed concrete (PC) elements leads to significant financial losses due to the requirements for recognition, maintenance and repair of damaged elements. Maintenance of reinforced concrete infrastructures exposed to corrosion costs around one hundred billion dollars annually globally (F. Li & Yuan, 2013). Safety concerns arise when there is a reduction in the resistance capacity of concrete elements and when the failure mechanism moves to experience brittle failure in which a suddenly collapse of infrastructure or structure occurs. This kind of collapse is considered as critically unacceptable, particularly in case of bridges because of the dangerous situation that will create for users and infrastructure itself. There are a wide range of cases especially bridges that have been collapsed due to degradation caused by corrosion worldwide (Figure 1-1). The Santo Stefano bridge in Sicily, Fossano bridge in Piemonte, Morani Bridge in Liguria, Congress Hall in Berlin could be mentioned as examples that encouraged research communities to make planned survey on the reasons of collapses (Belletti et al., 2020).

Figure 1-1 _ Collapse of Fossano bridge, 2017 (Micozzi et al., 2023)

Infrastructures used in road networks, because of their safety and economic significance, are crucial to be well-designed, built, regularly monitored and maintained. They may be subjected to varying phenomena and unexpected forces, such as dry and wetting cycles, earthquakes or strong winds. In these cases, it is vital that bridges remain functional, as they often serve as the sole access route to many urban areas (Safabakhsh et al., 2024). Corrosion effects on existing structures and infrastructures has been not only a national-wide, but also an international-wide issue. Although, a lot of research has been done to evaluate the safety, technical and economic effects of corrosion by public and private authorities and research communities, much further research should be allocated to corroded concrete member, especially the prestressed concrete (PC) elements because a few experimental, analytical and numerical research have been carried out in this field compared to the ordinary reinforced concrete (RC) elements. Bond behaviour between reinforcing steel and surrounding concrete can be considered as one of the main factors influencing the ductility and overall structural performance of reinforced concrete structures. Bond is essential for the effective transfer of stresses between steel and concrete, ensuring that the composite action between these materials is satisfied under various loading conditions. However, the bond properties can be significantly affected by presence of corrosion, which poses a serious threat to the integrity of reinforcing steel. The impact of corrosion on bond behaviour varies depending on type and severity of corrosion, as well as the characteristics of the reinforcing steel used, whether it is an ordinary steel bar or prestressed strand. Corrosion can lead to a reduction in the bond strength by causing the deterioration of the steel-concrete interface, leading to a loss of adhesion and, consequently, a reduction in the structural ductility and resistance. Therefore, the bond between reinforcing steel and concrete plays a significant role in determining the long-term durability and safety of reinforced concrete structures, particularly in environments where aggressive corrosion is a concern.

1.2 Definitions

1.2.1 Corrosion

Corrosion is known as a gradual destruction and degradation of materials, specifically metals, because of chemical or electro chemical reactions with the surrounding environment. This complicated process includes the transformation of the metallic material into a more chemically stable form like an oxide, hydroxide or sulfide. Generally, corrosion occurs due to reactions of metal with oxygen, moisture and aggressive components presenting in the air. Rust or iron oxide could be mentioned as a common example formed by reactions of iron with water and oxygen. Corrosion could be accelerated by several external factors such as high humidity, temperature, acidic or saline environment and some chemicals. The location of steel in the composite element, size of steel, type of concrete depending on amount of PH and internal chlorine in concrete, protective cover and quality of concrete are known as the internal factors affecting corrosion. There are different kinds of corrosion consisting of uniform corrosion where the metallic material degrades approximately equally across the surface, and localized corrosion like pitting and crevice corrosion where damage is concentrated in specific area. Galvanic corrosion can be mentioned as another kind of corrosion occurring when two different metallic materials are in electrical contact exposing to electrolyte, leading to one metal to corrode preferentially. Exposing to aggressive environments like marine and mountain environments which include potential agents like chloride ions and de-icing salt cause a type of corrosion called chloride induced corrosion leading to localized and pitting corrosion. When the localization amount of chloride overpasses the threshold limitation at steel in reinforced concrete (RC) elements, it influences the concrete alkaline area, and the protective layer of reinforcement will be demolished which allow the pits to increase. The exposure to chloride induced corrosion has been worse in recent years due to the climate change leading to rising the sea level and for instance, heavier snow in the mountainous environment in which more de-icing salts used to operate the transport lines.

Figure 1-2 _ Chloride-induced corrosion in a prestressed concrete (PC) beam

More importantly, chloride induced corrosion in prestressed concrete (PC) elements causes the more critical situation by allowing the pits to induce stress aggregation and localized failure. On the other hand, several reasons such as using more and more personal cars in urban areas and industrial factories increase the emission of greenhouse gases and especially carbon dioxide. The presence of carbon dioxide in the urban area and exposure of the structures to this environment for long time also causes carbonation induced corrosion. Structural elements using in the car parking are suffering more from this phenomenon. In general, when the reinforcing steel is in contact with aggressive and corrosive agents, deterioration of elements will occur by transforming reinforcing steel to rust. The mechanical properties and the geometry of RC and PC members are modified as well as the bond behaviour between reinforcing steel and concrete. Moreover, in the case of prestressed concrete elements, high stress levels in the strands can modify how they corrode. When strands are exposed to both high stress and a corrosive environment, they experience two types of corrosion, traditional electrochemical corrosion and stress corrosion. The combination of these factors can cause micro cracks to form on the surface of the strands. Stress corrosion consists of two main types, anodic dissolution stress corrosion and hydrogen-induced cracking stress corrosion. These micro-cracks can lead to brittle fractures in the strands, which can happen at much lower strengths than what the strands are normally capable of withstanding, a process referred to as stress corrosion. When there is high stress, it can cause the protective layer on the strands to crack, exposing fresh surfaces. The cracked area acts as an anode, while the unbroken protective layer serves as a cathode. The water in the pores of the components acts like an electrolyte, creating a closed-circuit electrolytic cell. As the anode dissolves, the cracks continue to grow inward. Because of the high stress, these cracks keep expanding, making it difficult to create a new protective layer. This ongoing electrochemical reaction causes the strand's surface to dissolve further, leading to deeper cracks. The brittle fracture strength of the strands is significantly lower than their tensile strength, resulting in a type of corrosion known as anodic dissolution stress corrosion. Additionally, during manufacturing, strands can absorb hydrogen and chloride ions, which react to produce hydrogen. This hydrogen increases at the fracture surfaces due to high stress. When the concentration of hydrogen builds up to a certain level, it can make the strands brittle and cause cracks to form at the fracture points. Continuous cracking can result in weakness in the strands, leading to hydrogen brittle fracture, which is known as hydrogen-induced cracking stress corrosion. Finally, Preventative approaches like protective coating and using corrosion resistance materials and knowing the methods to decrease the corrosion are necessary to mitigate the influences of corrosion and increasing the lifespan of metal components (Wang, 2023).

1.2.2 Bond behaviour

Bond is known as the adhesive and frictional interaction between reinforcing steel and concrete that guarantees they behave together as a single unit in a reinforced concrete member. The bond is crucial for concrete structures to perform in a correct way. Deterioration of bond between steel and concrete will result to decrease in capacity and ductility of elements. Chemical adhesion and cementation process which plays a role at the molecular level, frictional resistance which prevent the relative displacement between steel and concrete and the textured surface of steel which is design to interlock the rebars with the surrounding concrete by for example formation of ribs in rebars and some methods relating to strands usually define bond properties. The concrete usually withstand against compressive loads and steel is more effective to sustain the tensile stress, therefore, having an acceptable bond between two elements is necessary to effectively transfer stress between each other to perform a composite reaction against different load types and preventing from some issues like material separation and slippage to not have unexpected failure. Bond strength depends on various factors such as quality of material, surface condition, geometry of steel, construction quality of elements, bond length and importantly presence of corrosion in the section.

1.2.3 Prestressed Concrete (PC) members

Prestresses concrete (PC) elements are a new type of reinforced concrete (RC) construction and specialized components of concrete elements designed to sustain higher loads and stresses by applying internal compressive stresses before applying the element under service load. They have potential to strengthen the crack resistance and stiffness of elements. This could be satisfied by applying high-strength steel wires inside the concrete, improving considerably the structural performance by strengthening the elements against the tensile force which causes generally cracking. Prestressed concrete (PC) elements are commonly being used in several civil engineering applications in which high resistance capacity, slender structural elements and long spans are needed. It helps conserve materials and decrease the overall weight of structures. By using high-strength materials efficiently, prestressed concrete enables smaller dimensions for the cross section of structural components, which in turn reduces the total dead load. This is particularly valuable for bridges with long spans, as the weight of the structure plays a major role in their design and performance. Prestressing can serve as a way to link different parts of structures, encouraging the creation of new design methods and building techniques particularly for bridges. The structure's ability to withstand fatigue can be also enhanced, which is advantageous for bridges that experience live loads. Using prestressing technology in concrete construction can help work out usual problems like cracking and deformation of the concrete. This leads to better stability and a longer lifespan for the concrete structure, which ultimately enhances the overall quality of the structure or infrastructure. Bridges, as mentioned, and car parking garages are the major applications of these elements which are also exposed to corrosive environment.

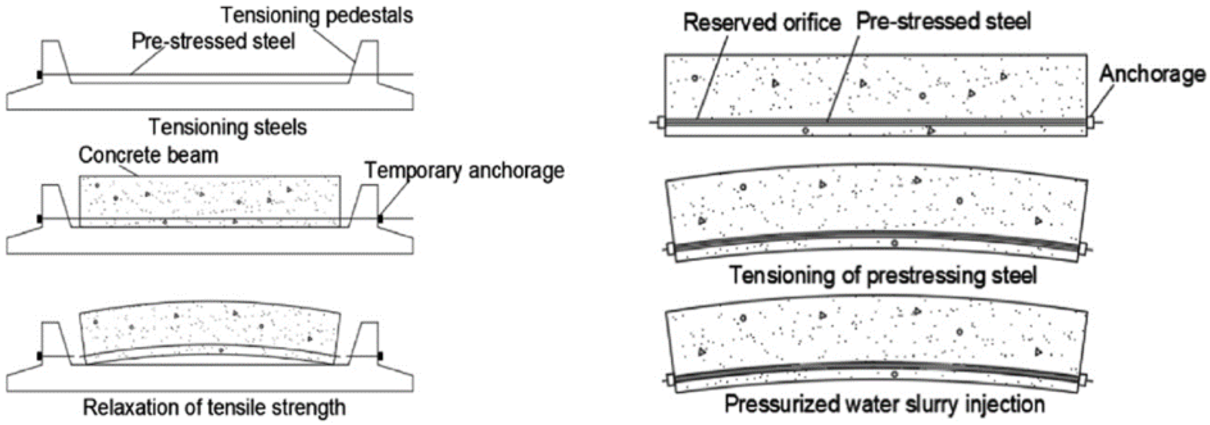

(a) (b)

Figure 1-3 _ (a) Pre-tension method, (b) Post-tension method (Wang, 2023)

There are two major construction methods including pre-tensioning method, where steel wires are held in tension before casting the surrounding concrete. The tension in wires will be released after concrete hardening, which causes compression in the surrounding concrete because the tensioned wire tends to come back in their previous condition that had before tensioning. Post-tensioning could be mentioned as another method, in which the steel wires placed in the ducts inside the concrete element after casting and hardening of concrete. The compressive stress is applied then to concrete by tensioning the wires and anchoring at the ends, Figure 1-3. As the technical and economic benefits of prestressed concrete (PC) elements, increasing the load-carrying capacity, improving resistance against higher loads without experiencing tensile crack, reduction of material usage by capability to construct thinner elements and improving the ductility of concrete elements could be mentioned.

1.3 Aim and Scope of This Research

The primary objective of this thesis is to investigate the bond behaviour between naturally corroded steel strands and the surrounding concrete and it’s effect on the beam capacity in prestressed concrete (PC) beams. This study aims to provide a comprehensive understanding of how natural corrosion affects the bond strength and overall performance of these structural elements. To achieve this goal, three experimental beam-end specimen tests were conducted, focusing on beams with naturally corroded strands. These tests were meticulously designed, executed, and monitored to capture detailed data on the bond characteristics. The results obtained from these experiments were systematically recorded and analysed to evaluate the impact of corrosion on bond performance. In addition to experimental investigations, this research utilizes the Model Code 2010 and the bond stress-slip relationship model introduced by (Wang, 2023) to gain deeper insights into the influence of corrosion on bond behaviour in prestressed concrete beams. The experimental tests were complemented by Digital Image Correlation (DIC) techniques, which were employed to monitor and record the deformation and displacement of the test specimens with high precision. This advanced imaging technology enabled detailed observation of the displacement in the beam-end specimen. Furthermore, Non-Linear Finite Element Analyses were conducted using Abaqus software to simulate the experimental tests. This computational approach allows for a more nuanced understanding of the bond mechanisms and the influence of corrosion on bond behaviour. The Finite Element Model was calibrated based on experimental data, providing valuable insights into the performance of corroded strands in prestressed concrete beams. Through this multi-faceted approach, the thesis aims to enhance the understanding of bond degradation in corroded PC beams and contribute to the development of more accurate predictive models for assessing the durability and safety of these critical structural components.

2 Literature Review

Apart from the corrosion type, it has several effects on the durability, capacity and failure mechanism of reinforced concrete (RC) and prestressed concrete (PC) elements and the degradation process is being accelerated because of climate change and global warming. One parameter that is affected crucially by corrosion is the bond behaviour between reinforcing steel and surrounding concrete which plays an important role to govern the interface behaviour of reinforcing steel and concrete (Dang et al., 2014a). Corroded steel bond behaviour needs to be studied very carefully because it has direct effect on the serviceability and ultimate load-carrying capacity of RC and PC elements due to anchoring needs. The interaction between steel and concrete modified by corrosion influences the transmission process of tension and compression stresses between two elements. The corroded strand surface will be covered by rust and loose oxide which causes decreasing cementation and chemical action. Moreover, corrosion will lead to volume expansion of steel depending on the corrosion level.

Subsequently over time, the corrosion process progresses, resulting in a reduction of the rebar's cross-sectional area, which consequently diminishes the steel's strength and deformation capacity. In the later stages of corrosion, spalling of the concrete cover may occur, leading to a decrease in the confinement provided to the longitudinal rebars (Miano et al., 2024). Consequently, frictional resistance and bond between reinforcement and concrete increases in the initial stages, but by developing and propagating of the corrosion level, the expansion amount will overpass the concrete resisting limit and the cracks start which eventually decreases the bond between steel and concrete (F. Li & Yuan, 2013). Also, the subsequent strand and reinforcement cross-section reduction which leads to more bond loss in the interface of steel and concrete is critically crucial not only for safety reasons, but also due to enormous potential social economic hazards. Corrosion of strand in prestressed concrete (PC) needs to be studied more seriously than ordinary reinforced concrete (RC) due to being exposed to high level of stress and conduction with cross sectional loss caused by corrosion leading to unsafe and brittle failure (Rinaldi et al., 2010). Extensive research has been conducted to investigate the various impacts of corrosion on reinforced concrete (RC) and prestressed concrete (PC) elements specially in term of bond properties. Studies are consisting of experimental campaign on artificially and naturally corroded steel, analytical and numerical study to understand how bond behave when steel damaged by corrosion and consequently how the structure suffering from bond deterioration behaves.

2.1 Experimental Review

A lot of experimental efforts have been done in recent years to understand the bond properties of corroded reinforced concrete elements. The studies typically involved controlled laboratory experiments where different test set-ups are applied. The geometry of specimen and test set-up have been different in literature. Bond behaviour tests can generally be categorized into local bond tests and anchorage efficiency assessment tests. Local bond tests focus on assessing the local bond-slip relationship between steel and concrete, typically using a restricted embedment length at the interface, pull-out test. In these tests, the reinforcement is subjected to tension, while the concrete is under compression. Pull-out test also allows for the examination of the impact of specific parameters on the bond performance of reinforced concrete (RC) structures, isolated from other influencing factors. A similar approach is the modified concentric pull-out test, which also aims to analyse the local bond relationship between steel and concrete. Unlike the standard pull-out test, the modified version places the concrete surrounding the bars under tension rather than compression. This distinction is significant for understanding the serviceability of reinforced concrete (RC) structures, especially in terms of assessing crack widths in service load. In contrast, there is another type of test that involves a longer bonded length than pull-out tests. These tests are designed to assess the performance of reinforcement anchorage in concrete. The bond strength is measured as the average force exerted along the entire anchorage length. This type of test is often known as a beam-end test and is particularly valuable for evaluating the ultimate capacity of RC structures. Both long and short embedment length tests have been conducted, with and without confinement with different corrosion conditions (Mancini & Tondolo, 2014). Furthermore, various methods and techniques are available to assess and analyze specimens and cases exhibiting degradation that require repair, including both destructive and non-destructive techniques. Non-destructive methods, such as Infrared Thermography, Electrical Resistivity Tomography, and Laser Scanning, are commonly employed for on-site testing (Puppio et al., 2023). However as mentioned above, tests specifically related to corrosion levels and corrosion-induced degradation are typically conducted in laboratory settings, where corrosion processes and their effects are simulated for more controlled analysis. Twenty pull-out specimens, both with and without stirrups, were subjected by (Wang et al., 2017) to accelerated corrosion to induce concrete cracking. The results showed that corrosion-induced cracking significantly decreased the bond between the strand and concrete. However, stirrups helped delay this bond deterioration. Bond stiffness and strength declined immediately after cracking, but cracks smaller than 0.35 mm had no impact on these properties when stirrups were present. As crack widths increased, bond stress distribution became more uneven, with stirrups playing a crucial role in preventing further degradation and causing the maximum bond stress to shift toward the free end once cracks exceeded a critical width. In the same way (Zheng et al., 2022), 35 reinforced concrete (RC) pull-out specimens were exposed to accelerated corrosion using electroosmosis, steady current, and dry-wet cycling methods, followed by pull-out testing. The study examined how variations in the degree of corrosion of longitudinal rebar and stirrups, cover thickness, stirrup spacing, and rebar diameter affected bond performance. The analysis showed that corrosion decreases the bond strength and failure mechanism tended to show brittle failure.

Eccentric pull-out tests were conducted by (Hanjari et al., 2011a) to examine the impact of severe corrosion, extensive cover cracking, and the role of corroded and non-corroded stirrups on the anchorage of deformed bars. The specimens underwent a low-rate electrochemical corrosion process over three periods, resulting in up to 20% weight loss in the main bars and 35% in the stirrups. Pull-out tests were then performed on either the two corner bars or the middle bar in each specimen to assess bond capacity. Results indicated that corner bars had lower bond capacity than middle bars, suggesting reduced confinement for corner bars. This difference in bond capacity became more noticeable in the absence of stirrups. Among corroded main bars, the highest anchorage capacity was found in the middle bar with uncorroded stirrups, while the lowest was in the corner bar without stirrups. A complex failure mode was observed in specimens with stirrups due to the interaction between stirrups and main bars at the corner angles. Without stirrups, failure in corroded specimens was primarily due to the splitting of the concrete cover. Although delamination cracks developed, the corrosion damage did not lead to complete cover delamination.

A beam- end test has been done by (Sarhan et al., 2018) to analyze the effect of concrete cover and type of reinforcement on bond properties. The experimental campaign consisted of five samples appropriately designed as beam-end elements. Specimens were reinforced by deformed steel bar and also steel plates separately. Consequently, it was shown that a pullout together with splitting crack occurred generally in the failure mechanism of beam-end specimens. Moreover, the results showed that larger bond area of reinforced steels can help to have less slip and better stiffness.

The specimens, designed as beam-ends, were subjected to an accelerated corrosion process by (Hanjari et al., 2011b) using an imposed current carefully maintained at the lowest feasible current density throughout the laboratory testing. The research focused on the initiation and propagation of cracks, as well as the delamination of the concrete cover. The study achieved significant levels of corrosion, with up to 20% in the main reinforcing bars and 34% in the stirrup legs. The investigation examined the influence of the bar's placement (both middle and corner), the amount of transverse reinforcement, and the extent of corrosion in both longitudinal and transverse reinforcements. Crack patterns and widths were analyzed, revealing notable differences between corroded and non-corroded specimens.

Corrosion from natural processes occurs slowly, prompting researchers to use accelerated tests to replicate its effects within a shorter timeframe. However, these accelerated tests often differ significantly from real-world conditions, especially in terms of current density used to hurry up corrosion. The type of oxide produced during these tests, influenced by the current rate and moisture conditions, can differ greatly from those formed under natural corrosion, leading to different expansion behaviours than those observed in actual structures. High current densities used in these tests may cause additional material degradation that doesn't accurately reflect the bond degradation in real structures. Moreover, real-world corrosion occurs gradually after an initiation period and interacts with the structure’s ongoing loading and unloading cycles. This cyclic load is not fully captured in accelerated tests. Research has shown that being under cyclic load, reveal a reduction in bond-slip performance, and the presence of corrosion worsen this degradation. In structures exposed to many loading cycles, such as bridges, it is crucial to consider both mechanical loading and chemical actions together. Corrosion tends to localize around transverse cracks, in addition to causing distributed damage. This localization is due to fretting fatigue near transverse cracks, where relative slip between concrete and reinforcement occurs. The resulting local bond effects at crack locations, combined with potential temperature increases from friction, can accelerate the corrosion process further in those specific areas (Mancini & Tondolo, 2014). Therefore, it could be understood from literature that accelerated corrosion could not be considered as exactly appropriate method to simulate the natural corrosion. Replicating natural degradation in accelerated corrosion tests is approximately difficult.

(Lundgren et al., 2019) proposed a methodology as an effective alternative to accelerated test by using degraded samples from decommissioned structural elements. The methodology outlies methods for choosing and designing tests to examine the bond and anchorage between steel and concrete in such samples, aimed at providing essential data for developing general evaluation methods for structures. The methodology consisted of selecting an appropriate existing structure for specimens, selecting the test method, designing the test setup and designing the test method. Given the typically large variability in test results, the chosen test method should allow for many tests by being robust, fast and reasonable. It is suggested to document the position of samples in the base structure, record cracks and sample uncorroded bars for reference in quantifying the corrosion level of corroded bars. The methodology emphasizes that careful planning is necessary to design experiments that produce reliable data. Obtaining data from decommissioned structures will enhance our comprehension of the structural behaviour of existing structures and improve investigating methods.

Moreover, another study on an existing sample which was a part of bridge edge beam has been done by (Lundgren et al., 2015) to evaluate the anchorage capacity of naturally corroded specimens. Beam specimens, exhibiting varying degrees of corrosion from nothing to extensive damage, were subjected to a four-point bending test using suspension hangers for indirect support. The beams were reinforced with transverse reinforcement to prevent premature failure. Eight tests were conducted, all of which exhibited diagonal shear cracks followed by a splitting-induced pull-out failure, confirming the intended anchorage failure. Results indicated that corroded specimens had approximately 10% lower capacity compared to non-corroded references. The average bond stress in the anchorage zone was found to be 16% lower in beams with corrosion cracks and 9% lower in beams with cover spalling, with greater difference in the damaged specimens. These findings enhance our understanding of the structural behaviour of corroded reinforced concrete under real-world conditions.

Several research on naturally corroded specimens also has been done. Twelve pull-out samples corroding naturally for seventeen months have been tested by (F. Li & Yuan, 2013) to evaluate the effect of corrosion on bond behaviour of strand. The results showed that bond stress-slip graph regarding uncorroded strand had three parts including moving up at first, almost horizontal and then dropping part. While only two parts including moving up and then dropping part are observed regarding corroded strand. Moreover, the inclination of dropping part increases by increasing the corrosion level. It is also observed that in case of corroded strand, the crack width was more critical than ordinary corroded reinforcement.

(Zhang et al., 2009) examined reinforced concrete beams exposed to a chloride environment for 14–23 years under service loading. The experimental results showed that a Serviceability Limit State (SLS) criterion based on significant steel–concrete bond reduction could be proposed. Corrosion in chloride environments causes localized loss of steel cross-section and a decrease in steel–concrete bond strength. Early in the corrosion process, beam deflection is more easily affected by chloride-induced corrosion than ultimate capacity, due to the loss of bond strength between the steel and concrete, despite there is a correlation between the two. This sensitivity to corrosion-induced bending stiffness reduction suggests that excessive deflection is a suitable SLS criterion. In later stages, when the bond is severely developed, ultimate capacity is affected by steel cross-section loss, while serviceability remains unaffected due to the localized nature of pitting attacks. Once the critical bond is lost in high bending moment areas, further pitting does not impact serviceability but continues to reduce ultimate capacity. Therefore, significant steel–concrete debonding can be known as a reliable SLS criterion.

Beams were exposed to naturally chloride corrosive environment for 26 years subjected to service load were tested by (Zhu et al., 2013) to simulate realistic structural and environmental scenarios.

Detailed documentation of the crack patterns and widths was conducted for two severely corroded short-span beams, which were then subjected to failure testing using a three-point loading system. Additionally, two similarly aged beams without corrosion were tested as reference specimens. A short-span setup was selected to assess the impact of reduced steel area and bond strength on shear capacity. The load-deflection response and tensile bar slip were monitored to gain insights into the mechanical behaviour of the corroded beams. After testing, the corroded reinforcements were extracted, and corrosion maps and area loss were documented. Tensile tests on the main longitudinal reinforcements were also performed. The study discusses the residual mechanical behaviour of the beams considering the experimental data and crack patterns. The findings revealed that chloride-induced corrosion significantly affects the mechanical performance of short-span beams, with reductions in cross-sectional area and bond properties markedly impacting bending capacity.

A study done by (Almusallam et al., 1996) concentrated on the bond properties of RC members consisting of ultimate bond strength, free end slippage, and modes of failure during pre-cracking, cracking and post-cracking stages. The investigation also assessed how various crack width and rib profile deterioration because of different corrosion range affected bond strength. Findings revealed that ultimate bond strength grows in the pre-cracking stage (less than 4% corrosion) while in higher corrosion rate, slip reduced at ultimate bond strength. Bond deterioration was attributed to the conquering of concrete kyes close to the bar pulls. When the corrosion level reached 4-6% bond failure happened abruptly experiencing low free end slippage, and significant slip was observed as bond failure resulted from sample splitting. Above six percent of corrosion, bond failure was characterized by constant slip of steel. Ultimate bond strength first rose with corrosion level up to 4% before sharply declining to 6% of corrosion. Above 6%, bond strength remained relatively stable until 80% corrosion rate. Regarding rib profile, a significant drop in bond strength began when deterioration overpassed 25%, continuing until 45%, after which further rib profile deterioration had no notable impact on bond strength.

A standard test for strand bond has been done by (Dang et al., 2014b) to evaluate the bond stress-slip relationship of prestressed strand and how bond stress distributed along the strand. To reach this aim, twelve 17.8 mm and eighteen 15.2 mm specimens which were parts of prestressed strand coils were collected and cared from external environmental attacks. It has been shown that the slip in the free-end part of specimen is identical whereas, in the load-end part, it is linearly dependent on pull-out force. Moreover, there is a nonlinear relationship between bond stress-slip causing a not uniform distribution of bond stress along the bond length. Results showed that the load-end has more sensitivity to the pull-out test than the free-end part. The failure mode of anchorage and transmission length in prestressed concrete elements, highly affected by corrosion effect bond stress-slip relationship.

In an experimental study (Martí-Vargas et al., 2013), it was shown that when the anchorage length is more than the transmission length, the anchored steel force without end slip of strand is more that the transferred prestressing force. While in the case of less or similar anchorage length, the transferred prestressing force and strand force are equal. Moreover, the mean bond stress during the transmission length was more than that during the corresponding bond length and less than that during anchorage length with slip.

2.2 Analytical Models Review

The development of analytical models is crucial for understanding the bond behaviour between steel and concrete, as these models provide a systematic and predictive framework for evaluating the complex interactions between materials. Accurate analytical models enable engineers and researchers to anticipate how the bond will perform under various conditions, which is essential for ensuring the structural integrity and durability of reinforced concrete structures. Factors such as corrosion significantly modify the bond behaviour, leading to reduced adhesion, increased crack propagation, and eventual structural failure. By proposing robust analytical models, it becomes possible to quantify the effects of these factors, allowing for the design of more resilient structures and the development of effective mitigation strategies to counteract bond degradation. Also using appropriate models has economic benefits. For instance, a study in Sweden demonstrated that applying the model led to cost savings of around €3 million by eliminating the need for unessential repairing measures. The Swedish Road Administration oversees 20,000 bridges, and there are almost one million bridges across the EU27, many of which are constructed from reinforced concrete and situated in corrosive environments. Given this context, the potential societal cost savings could be substantial, provided the model is reliably implemented and accessible for engineering applications (Blomfors et al., 2018). Therefore, several researchers have tried to propose a reliable analytical model with this regard.

An analytical one-dimensional model has been introduced by (Lundgren et al., 2012) for the bond-slip response of corroded reinforcement. The introduced model is a development of the bond-slip model outlined in the CEB-FIP Model Code 1990 and is especially appropriate for structural analyses aimed at calculating the load-carrying capacity of structures exposed to corrosion. Additionally, the model calculated the bond length required to anchor the yield force based on the bond-slip relationship, considering a one-dimensional bond-slip differential equation. The model's predictions were compared with experimental data and the results from an advanced three-dimensional finite element model. The computed outcomes, including bond-slip curves, maximum bond stress, and the required bond length to anchor the yield force, generally aligned well with experimental observations, indicating a qualitatively accurate representation of physical behaviour. The proposed model tended to produce conservative results in most scenarios. However, it is important to note that for cases involving high rate of corrosion penetration and no transverse stirrups, relying on this model to estimate the required anchorage lengths may not be advisable. Specifically, when the concrete cover has completely spalled off. Moreover, for high corrosion penetrations (e.g., exceeding 400-500 microns), the model may result on non-conservative estimates, suggesting a need for refinements to account for interface degradation, such as rib reduction and the resulting modification in friction angle.

Another analytical model has been introduced by (H. Li et al., 2024) to illustrate the influence of steel strand corrosion on the decrease in bond strength. Initially, the corrosion-induced expansion force of the steel strand, both before and after the occurrence of corrosion cracking, was estimated. This was followed by an assessment of the reduced gripping influence of the concrete, the modification in the friction coefficient of the corroded strand, and the reduction of the bearing force. These factors were then integrated into the calculation of the pre-rib extrusion force. Eventually, the model accounted for the increase in bond strength due to the transverse confinement provided by stirrups, leading to the calculation of the ultimate bond strength of the corroded steel strand. The predicted bond strength was influenced by the extent of strand corrosion but is largely unaffected by the method of drawing. Also, a modified bond stress-slip model based on the experimental data of (Zheng et al., 2022) has been proposed. The model was based on design parameter, longitudinal and stirrup corrosion of corroded pull-out specimens.

An existing model for evaluating the bond capacity of corroded reinforced concrete has been developed by (Blomfors et al., 2018). The developed version is according to the local bond slip relationship driven from fib Model Code 2010 and has been defined to consider corrosion. The model has been validated against a comprehensive database of nearly 500 bond tests and through comparisons with an established empirical model from the literature. The findings reveal significant variability in bond test results, even within groups exhibiting the same levels of confinement and corrosion. Despite this variability, the developed evaluation model effectively represents the deterioration of anchorage capacity due to corrosion. This updated version of the model demonstrates an appropriate consistency with experimental data. Unlike many empirical models, this model accurately captures the physical behaviour, providing a complete demonstration of the local bond stress-slip relationship. Employing this estimation model enhances the capability of engineers to more accurately predict the bond capacity of corroded concrete structures. A significant reduction in bond strength occurring when corrosion causes the concrete cover to crack, particularly in cases with minimal stirrup content, was observed. The results also showed that the integration of Model Code 2010 into the assessment model now allows for consideration of the reinforcement bar's position within the cross-section, a feature that was absent in the previous model. By using Model Code 2010 as the foundation for ARC2010, the model also incorporates additional effects addressed in the code, such as longitudinal cracking. With this model, a complete local bond-slip graph could be obtained in addition to maximum bond strength. The model had acceptable consistency with the experimental database, including 0.05 precent difference for the cases without stirrups and 0.09 precent difference for cases with stirrups.

To replicate corrosion-induced cracks and specifically examine their impact on bond strength degradation, a novel method involving pipes filled with an expansive agent was introduced by (Syll et al., 2021). The study was supported by performing pull-out tests on concrete specimens with varying induced crack widths and different splitting patterns. Passing time, as the crack width increased due to the expansion of the aluminum pipe, a desired target crack width was achieved. The findings demonstrated that the kind of splitting significantly affects the decrease in bond strength, with "side-split" modes resulting in more serious degradation than "single-split" modes. Additionally, using surface crack width as a key variable, an analytical model was developed to anticipate bond strength deterioration caused by reinforcing steel corrosion. These predictive models showed strong correlation when compared to data available in existing literature.

In the similar way (Syll & Kanakubo, 2022) has proposed another empirical formula to analyze the bond strength for the specimens with the presence of stirrups compared to mentioned study (Syll et al., 2021), which was regarding the bond strength in the cases without stirrups. This study introduced a formula for bond strength degradation that accounts for the significant impact of stirrup degradation caused by corrosion. It was shown that bond strength reduces significantly with growing crack width in specimens lacking stirrups. However, the presence of confinement mitigates this deterioration. An empirical model was developed to evaluate bond strength deterioration based on the crack width and stirrup proportion. Comparisons with the latest information from corroded specimens indicated that the introduced model provides satisfactory consideration. Bond strength deterioration is primarily attributed to corrosion-induced cracks from the widespread corrosion products. Notably, a specific level of rebar corrosion can result in an extensive range of induced crack widths. The empirical model introduced by authors utilized cracked specimens (EAFP-induced cracks) without modifying the rebar profiles, enhancing the accuracy of bond strength results during pull-out tests.

2.3 Numerical Approaches Review

The use of numerical approaches, particularly nonlinear finite element analysis (NFEA), is vital in assessing the bond strength between steel and concrete. These advanced methods provide a detailed simulation of the complicated interactions between materials, capturing the intricacies of their nonlinear behaviour under various loading and environmental conditions. Such analyses are especially critical when considering the effects of corrosion, which can severely compromise bond strength over time. By using nonlinear FEA, engineers can predict potential failures and degradation patterns with high accuracy, offering insights that are often beyond the reach of experimental techniques. This not only enhances the reliability and safety of structural designs but also supports the optimization of materials and construction processes, ultimately leading to cost-effective and durable engineering solutions. Additionally, these numerical methods are invaluable in developing strategies to mitigate the adverse effects of corrosion, ensuring the longevity and integrity of concrete-steel bonds in harsh environments. A lot of researchers in recent years have tried to study numerical approaches to simulate and understand the bond behaviour of reinforcement.

Nonlinear finite element analyses (NLFEA) generally provide an accurate representation of material and structural behaviour, including the structure's additional load-bearing capacity. Using NLFA specially ABAQUS, there is a possibility of simulating and analyzing the specific components and also the complete structures and infrastructures framework such as bridges to evaluate several interested risks and aspects (Safabakhsh, 2024). However, the accuracy of NLFEA results is highly dependent on the assumptions made during the modeling process. To ensure that these methods are effective and reliable, it is important to test them by having different teams or individuals predict the outcomes of specific structural tests without knowing the actual results in advance (blind prediction). Then, by comparing these predictions to the real results and to each other, we can better evaluate how well the NLFEA methods work (Belletti, Stocchi, et al., 2017).

When a bond-slip relationship includes certain unknown factors and experimental data is available, these parameters can be identified using various numerical calibration techniques. Some methods operate under the assumption that slip and bond stress remain uniform along the entire embedment length. Nevertheless, in certain cases, it is crucial to account for the variation in slip and bond stress distribution along the embedment length, as this distribution may significantly influence the results. A numerical method to calibrate parameters of a given bond-slip relationship has been introduced by (Focacci et al., 2000). The introduced numerical method involved determining the parameters of a specific bond-slip relationship so that pullout test results could be accurately anticipated regarding the applied force and the resulting slips at both the loaded and free ends. This technique was applied to experimental information, with the results thoroughly analyzed. The computation time required for this method depended on the number of unknown factors in the selected bond-slip relationship.

The process becomes more straightforward and faster if the bond length is sufficient to prevent slip at the free end, potentially eliminating the most time-consuming calculation step. Understanding the local bond-slip law also enables the straightforward determination of anchorage length as a function of the law's parameters. This approach allowed for the general solution of structural issues, such as transfer and development length for any bar diameter in similar designs, thereby eliminating the need for empirical formulas.

Finite element analysis (FEA) using smeared crack formulations, such as the rotating crack model, often struggled to accurately simulate geometric discontinuities after the tensile softening of a finite element is complete. This issue results in an overly rigid response at the point of cracking due to unintended stress transfer, known as stress locking, and numerical unpredictability due to the violation of displacement continuity during spalling. One potential solution to address stress locking in smeared crack models is to remove finite elements from the mesh when they finish their tensile softening, allowing a gap to develop behind the microcrack and enabling the concrete on either side to elastically unload.

A similar method has been proposed by (Zandi & Lundgren, 2015) to account for modifications in mesh topology as corrosion-induced cracks evolve and create a delamination plane. The proposed approach involved a three-dimensional nonlinear FEA computation scheme with various calculation steps. Each phase applies a load step, and independent analyses are conducted with previous step results, typically stresses, serving as initial conditions. After each step, a new FE mesh is generated, except elements that have fully tensile softening or are part of a delaminated section. Nevertheless, elements are only removed from the mesh once a delamination plane has been created. This technique results in a more consistent analysis and significantly reduces computer demanding, effectively avoiding the issues associated with weak kinematic simulation in the discontinuous movement field about a delamination plane behind full tensile softening. The use of 3D finite element analysis in their study revealed that the corrosion of stirrups accelerates the onset of cracking and spalling, though the bond strength remains largely unaffected by stirrup corrosion post-cover spalling, provided early yielding of the stirrups has not occurred. Additionally, the analysis demonstrated that the stresses in stirrups caused by corrosion in nearby bars decrease significantly within a short distance from the primary bar. It was also found that the corrosion of stirrups has a more pronounced impact on shear capacity than the stresses induced in stirrups by the corrosion of the main bars.

A model has been proposed by (Lundgren & Gylltoft, 2000) to explain the bond between reinforcement and concrete. This model incorporates the three-dimensional splitting influence, leading to variations in load-slip curves based on factors such as whether the reinforcement begins to yield, as well as the geometry and strength of the surrounding concrete. To calibrate this model, steel-encased pull-out tests were employed, measuring tangential strain in the steel tubes. The analysis highlighted the significant effect of the concrete material model during cyclic loading, particularly on tangential strains even during the initial unloading phase. For more accurate calibration under cyclic loading, a material model specifically designed for such conditions is recommended. The selection of material model for the concrete also affects the results, with considerable differences observed. Fixed crack models, when used in scenarios where splitting cracks governed the failure, showed higher loads than those seen in experiments. The fixed crack direction in these models caused significant stress transfer. By employing rotating crack models, which obstacles the locking of crack directions, these high tensile stresses were mitigated, thereby improving the correlation between the numerical analyses and experimental findings. Comparison between bond mechanism and the failure mode of the model and experiments showed satisfaction. This model incorporated the splitting stresses associated with bond action, where bond stress was affected not only by slip but also by the radial deformation between the steel and the concrete. However, the mentioned bond model exhibited an issue of energy generation during certain specific loading-unloading sequences, prompting a revision in its formulation. With the modifications introduced by (Lundgren, 2005a), the 3D numerical model aligned with Coulomb friction principles, enhanced by a yield function to define the upper limit.

The modified bond model, in conjunction with nonlinear fracture mechanics for the concrete, was used to evaluate pull-out tests. These tests were chosen to demonstrate various failure modes, including pull-out failure, splitting failure, pull-out failure following reinforcement yielding, rebar crack, and cyclic loading scenarios. The outcomes indicated that the updated model effectively anticipates splitting failures and bond loss during reinforcement yielding, while also providing a realistic simulation of cyclic loading conditions. Consequently, in the more research, in the more research, another updated three-dimensional numerical model has been proposed by (Lundgren, 2005b) to consider the impact of both uniform and localized corrosion on bond strength. The findings demonstrated that localized corrosion required less average corrosion penetration to cause cracking of the concrete cover compared to uniform corrosion, and the resulting crack patterns were distinct. These analyses led to the conclusion that axisymmetric models are adequate for examining cracking caused by uniform corrosion. For studies focused on localized corrosion, three-dimensional modeling is necessary. Additionally, the model was applied to assess the influence of uniform corrosion on the bond length in the absence of transverse reinforcement.

An updated version of the PARC_CL 2.0 crack model has been introduced by (Belletti, Scolari, et al., 2017), implemented in Abaqus using the UMAT subroutine. The PARC_CL 2.0 model was a fixed crack model designed for anticipating the behaviour of reinforced concrete (RC) elements. The model has been enhanced by incorporating more sophisticated material constitutive relationships, allowing it to account for plastic strains. Comparisons with experimental data have shown that this model could closely anticipate the nonlinear behaviour of RC elements, largely due to its use of the tangent approach to incorporate plastic strains. The authors believed that the nonlinear shell and membrane modeling capabilities of the PARC_CL 2.0 crack model offer a valuable tool for estimating both local and global destruction signals, such as crack width and displacements. One significant advantage of a self-implemented model, compared to standard models in commercial finite element software, is the ability to assess multiple mechanical phenomena, leading to a more detailed and accurate analysis of structural element behaviour.

The updated PARC_CL 2.0 crack model has been also used by (Belletti, Stocchi, et al., 2017) as a physical approach for reinforced concrete modelling particularly adjusted to shear sensitive structures. The research aimed to assess the anticipative capability of the approach in capturing both global and local behaviours, with the goal of addressing the current gap between the requirement for nonlinear analysis in large structures and the practical application of these modeling techniques. The approach presented has proven effective in delivering reliable results for top displacement, floor acceleration spectra, interstorey drift, and eigenfrequency reduction. Furthermore, the use of shell elements in the modeling process has been shown to maintain computational costs at a reasonable level. Moreover, (Ravasini et al., 2023b) conducted a study to investigate the time-dependent characteristics of concrete. To achieve this, the researchers employed a Nonlinear Finite Analysis (NLFA) method, utilizing the UMAT subroutine within the Abaqus software. The use of the UMAT subroutine was necessitated by the limitations present in existing finite element software libraries, enabling a more accurate simulation of the problem. The study's results demonstrated a strong correlation with both analytical predictions and experimental findings.

3 Theoretical Explanation of Bond Strength

3.1 Model Proposed by fib Model Code 2010

3.1.1 Local Bond Stress–Slip Model

The word "bond" refers to the interaction and stress transfer between reinforcing steel and concrete. The bond stress–slip relationship is influenced by a wide range of factors, such as the geometry of the ribs (relative rib area), the strength of the concrete, the positioning and orientation of the bar in casting, the stress state, boundary conditions, and the concrete cover. The parameters provided in Table 3-1 apply to ribbed reinforcing steel with a relative rib area $f_r \geq f_{rmin}$, as specified by applicable international standards based on quality control, designation, geometrical properties, mechanical properties, technological properties, type of steel and assumptions used for design, (the detailed explanation is presented in fib Model Code 2010 (Model Code, 2010)).

The bond stress–slip curves depicted in Figure 3-1. for both confined and unconfined concrete can be taken into account as a generalized formulation that applies to a wide range of scenarios. To develop design bond stress–slip curves, additional reliability analysis is required. The initial ascending portion corresponds to the stage where the ribs embed into the mortar matrix, leading to local crushing and microcracking. For confined concrete, a sustained plateau follows, marked by advanced crushing and shearing of the concrete between the ribs. This stage indicates a residual bond capacity that persists only when an enormous concrete cover, dense stirrups help preserve some structural integrity. The descending part represents the decline in bond as the concrete corbels between the ribs are sheared off. In unconfined concrete, this often results in splitting failure, evidenced by a sudden decrease in bond stress before stabilizing at a steady residual level. The maximum bond strength associated with splitting failure is referred to as $\tau_{bu,slip}$, as illustrated in Figure 3-1 and defined in Equation 3-1 to Equation 3-6.

The following points should be considered when discussing the development of bond stresses:

In the regions where the bar is under compression and in the regions where bar is under tension located in the uncracked area of elements, both concrete and steel have the same strain ($\varepsilon_s = \varepsilon_c$). In cross-sections where there are cracks, tensile stresses are transmitted across the crack through the reinforcement. Generally, the exact displacements of the bar u_s and the concrete u_c near a crack are not the same. In the case of prestressed concrete elements also displacements are not similar during the transmission length l_{bpt}. The relative displacement s = u_s - u_c results in the generation of bond stresses between the concrete and the reinforcement or prestressing tendons. When s $\leq s_1$, these bond stresses are primarily determined by the slip s, but they are also affected by factors such as the steel surface characteristics, concrete strength f_{cm}, the positioning of the reinforcement during casting, and the confinement from the concrete cover, secondary reinforcement, and the stress state within the concrete surrounding the bar.

In the regions between cracks or along the transmission length l_{bpt}, portion of the tensile stress in the reinforcement at a cracked zone is transferred to the concrete through bond, resulting in the tension stiffening influence. The modification in relative displacement locally is described by the strain variation $\frac{d_s}{d_c} = \varepsilon_s - \varepsilon_c$. The coefficient a (0 ≤ a ≤ 1) in Equation 3-1 can be adjusted to model various bond stress–slip relationships, ranging from a constant bond stress (a = 0) to a linearly increasing bond stress (a = 1). The parameters listed in Table 3-1 mainly based on the failure mode, whether pull-out or splitting, with more discriminations made to accommodate different bond conditions within each failure mode.

Under specific and well-defined conditions, it is reasonable to assume an average "local bond" versus "local slip" relationship for short anchorage lengths that is statistically acceptable. This section focuses on the anchorage of ribbed reinforcing steel that meets the "high bond" classification requirements as outlined in section 5_2 of fib Model Code 2010. For monotonic loading, the reference bond stress value τ_b between the concrete and reinforcing bar, corresponding to pull-out and splitting failure, can be calculated based on relative displacement s along the bar axis as illustrated in Figure 3-1.

$$\tau_b = \tau_{bmax}^{(\frac{s}{s1})^a} \qquad \text{for } 0 \le s \le s_1 \qquad \text{Equation 3-1}$$

$$\tau_b = \tau_{bmax}^{(\frac{s}{s1})^a} \qquad \text{for } s_1 \le s \le s_2 \qquad \text{Equation 3-2}$$

$$\tau_b = \tau_{bmax} - (\tau_{bmax} - \tau_{bf})(s - s_2)/(s_3 - s_2) \qquad \text{for } s_2 \le s \le s_3 \qquad \text{Equation 3-3}$$

$$\tau_b = \tau_{bf} \qquad \text{for } s_3 < s \qquad \text{Equation 3-4}$$

Where the parameters are defined in in Table 3-1.

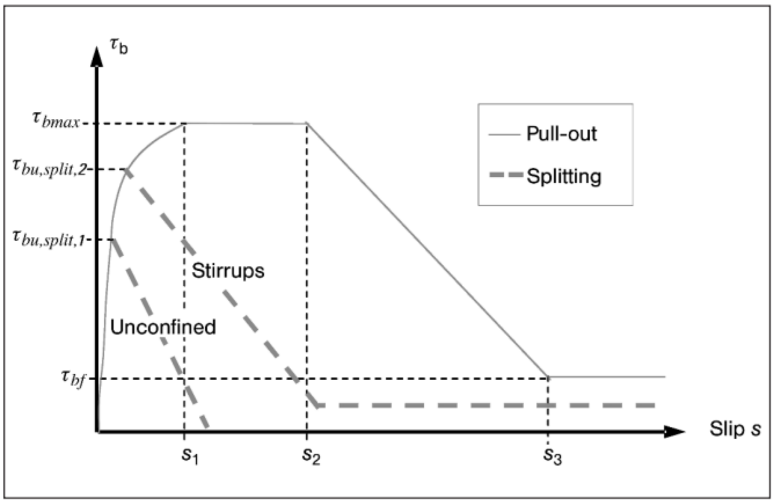

Figure 3-1 _ Bond-Slip relationship proposed by (Model Code, 2010)

Analytical bond stress–slip relationship (monotonic loading). $\tau_{bbu,slip,1}$,1 and $\tau_{bbu,slip,2}$ denote peak local bond resistance in the absence (Ktr = 0) and presence, respectively, of confining stirrups

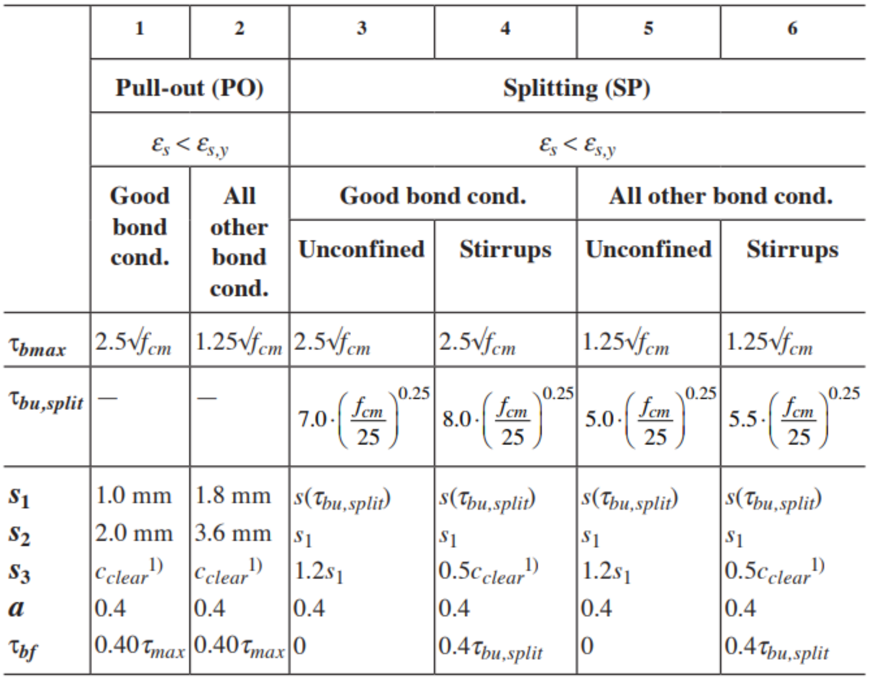

	1	2	3	4	5	6
	Pull-out (PO)		**Splitting (SP)**			
	$\varepsilon_s < \varepsilon_{s,y}$		$\varepsilon_s < \varepsilon_{s,y}$			
	Good bond cond.	**All other bond cond.**	**Good bond cond.**		**All other bond cond.**	
			Unconfined	**Stirrups**	**Unconfined**	**Stirrups**
τ_{bmax}	$2.5\sqrt{f_{cm}}$	$1.25\sqrt{f_{cm}}$	$2.5\sqrt{f_{cm}}$	$2.5\sqrt{f_{cm}}$	$1.25\sqrt{f_{cm}}$	$1.25\sqrt{f_{cm}}$
$\tau_{bu,split}$	—	—	$7.0\cdot\left(\frac{f_{cm}}{25}\right)^{0.25}$	$8.0\cdot\left(\frac{f_{cm}}{25}\right)^{0.25}$	$5.0\cdot\left(\frac{f_{cm}}{25}\right)^{0.25}$	$5.5\cdot\left(\frac{f_{cm}}{25}\right)^{0.25}$
s_1	1.0 mm	1.8 mm	$s(\tau_{bu,split})$	$s(\tau_{bu,split})$	$s(\tau_{bu,split})$	$s(\tau_{bu,split})$
s_2	2.0 mm	3.6 mm	s_1	s_1	s_1	s_1
s_3	c_{clear} 1)	c_{clear} 1)	$1.2s_1$	$0.5c_{clear}$ 1)	$1.2s_1$	$0.5c_{clear}$ 1)
α	0.4	0.4	0.4	0.4	0.4	0.4
τ_{bf}	$0.40\tau_{max}$	$0.40\tau_{max}$	0	$0.4\tau_{bu,split}$	0	$0.4\tau_{bu,split}$

Table 3-1 Parameters defining the mean bond stress–slip relationship of ribbed bars (according to Equation 3-1 _ Equation 3-4), (Model Code, 2010)

c_{clear} is the clear distance between ribs

The parameters of Table 3-1, columns 1 and 2 (related to pull-out failure) are applicable to well-confined concrete, where the concrete cover is at least 5Ø and the clear spacing between bars is at least 10Ø, or when adequate confining reinforcement is present. The parameters in columns 3 through

6 of Table 3-1 (associated with splitting failure) are calculated using Equation 3-6, which is derived from Equation 3-5 by assuming $\frac{l_b}{\emptyset}$ = 5. This assumes a uniform bond stress across this length and evaluates $\tau_{bu,slip}$ for Ø = 25 mm, with $\frac{c_{max}}{c_{min}}$= 2.0, c_{min} = Ø, and k_{tr} = 0.02 for bars confined by stirrups, or k_{tr} = 0 when no stirrups are provided.

$$f_{stm} = 54(\frac{f_{cm}}{25})^{0.25}(\frac{25}{\emptyset})^{0.2}(\frac{l_b}{\emptyset})^{0.55}\left[(\frac{c_{min}}{\emptyset})^{0.25}(\frac{c_{max}}{c_{min}})^{0.1} + k_m k_{tr}\right] \quad \text{Equation 3-5}$$

$$\tau_{bu,slip} = \eta_2(\frac{f_{cm}}{25})^{0.25}(\frac{25}{\emptyset})^{0.2}\left[(\frac{c_{min}}{\emptyset})^{0.33}(\frac{c_{max}}{c_{min}})^{0.1} + k_m k_{tr}\right] \quad \text{Equation 3-6}$$

Where:

η_2 is 1.0 for good bond conditions, = 0.7 for all other bond conditions

f_{cm} is the mean cylinder concrete compressive strength [N/mm2]

$\emptyset$ is the diameter of the anchored bar considered [mm]

c_{min} is min { $c_s$cs/2, c_x, c_y} (*Figure 3-2*)

c_{max} max {c_s/2, c_x} (*Figure 3-2*)

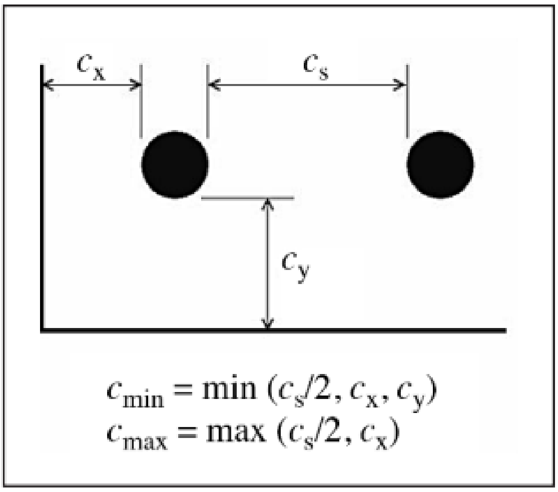

Figure 3-2 _ Notation for bar spacing and cover: straight bars, (Model Code, 2010)

k_m is the efficiency of confinement from transverse reinforcement and has a value of 12 where bars are confined inside a bend of links passing round the bar of at least 90°. Where no confining reinforcement is provided between bars and the nearest face, km = 0, as shown in *Figure 3-3*.

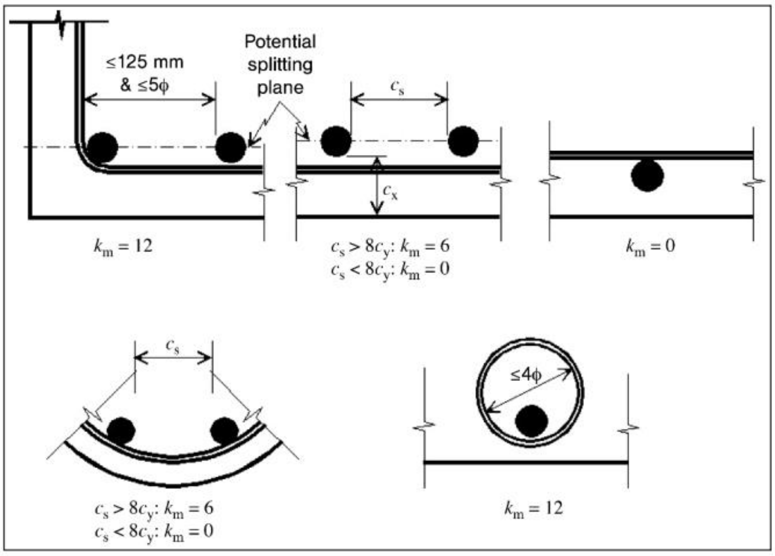

Figure 3-3_ Confinement coefficients for transverse reinforcement, (Model Code, 2010)

$$k_{tr} = n_t A_{st}/(n_b \emptyset\ s_t) \leq 0.05$$ Equation 3-7

Where:

n_t is the number of legs of confining reinforcement crossing a potential splitting failure surface at a section

A_{st} t is the cross-sectional area of one leg of a confining bar [mm2]

s_t is the longitudinal spacing of confining reinforcement [mm]

n_b is the number of anchored bars or pairs of lapped bars in the potential splitting surface

3.1.2 Influence of Transverse Cracking

Bond stress should be reduced by parameter λ for the reinforcements closer than 2Ø to the transversal crack:

Λ= 0.5 x/ Ø≤1 Equation 3-8

3.1.3 Influence of Yielding, Transverse Stress and Longitudinal Cracking and Cyclic Loading

Based on the Equation 3-1 to Equation 3-4, the bond stress could be changed by applying the effects of steel yielding, transverse pressure, cracking along axis of bar and cyclic loading.

$$\tau_{b,m} = \tau_{b0}\Omega_y\Omega_{p,tr}\Omega_{cr}\Omega_{cyc} \qquad \text{Equation 3-9}$$

Where the factors are related to:

Ω_y steel yielding

$\Omega_{p,tr}$ transverse pressure

Ω_{cr} cracking along axis of bar

Ω_{cyc} cyclic loading

And $\tau_{b,m}$ is bond stress according to the modified bond stress–slip curve

τ_{b0} is bond stress according to the bond stress–slip curve defined based on previous questions

3.1.3.1 Effect of yielding in reinforcing steel

The impact of the bar strains on local bond-slip when there is pull-out failure has been shown in *Figure 3-4* to demonstrate that bond reduces when steel reach to yielding.

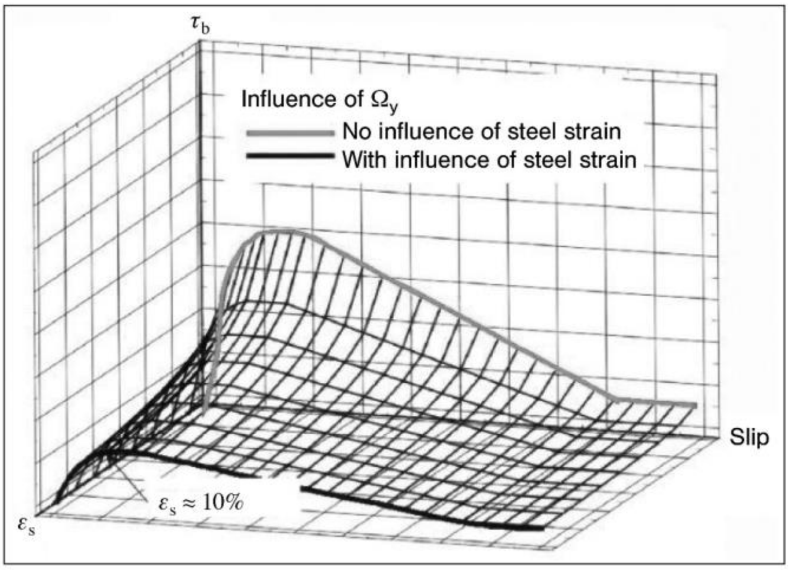

Figure 3-4 _ Bond reduction when steel reaches to yielding, (Model Code, 2010)

If there is yielding within the bond length, the yielding reduction factor Ω_y can be obtained as following:

$$\Omega_y = 1 \qquad For\ \ \varepsilon_s \leq \varepsilon_{sy}$$ Equation 3-10

$$\Omega_y = 1 - 0.85(1 - e^{-5a^b}) \qquad \varepsilon_{sy} \leq \varepsilon_s \leq \varepsilon_{su}$$ Equation 3-11

$$a = (\varepsilon_s - \varepsilon_{sy})/(\varepsilon_{su} - \varepsilon_{sy)}) \qquad b = (2 - \left(\frac{f_{tm}}{f_{ym}}\right))^2$$ Equation 3-12

3.1.3.2 Effect of transversal force

The bond capacity is reduced when there is transversal tensile stress and in the opposite way it is increased in the case of transversal compression stress. Impact of transversal stress is shown in *Figure 3-5* while there is pull-out failure.

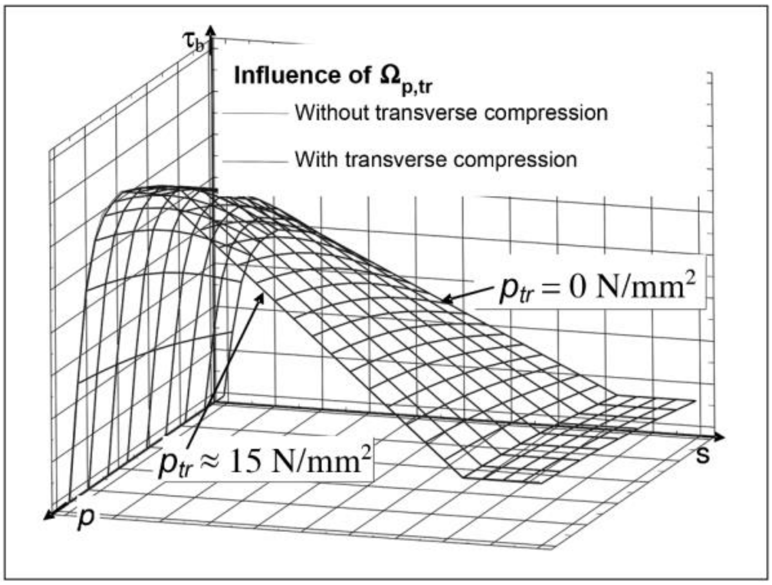

Figure 3-5 _ Transversal stresses effect in the case of pill-out failure, (Model Code, 2010)

The transverse pressure modification coefficient should be calculated according to following formula:

$$\Omega_{p,tr} = 1 - (\frac{0.3p_{tr}}{f_{ctm}}) \qquad f_{ctm} \geq p_{tr} \geq 0$$ Equation 3-13

$$\Omega_{p,tr} = 1 - tanh(\frac{0.2p_{tr}}{f_{cm}}) \qquad p_{tr} \leq 0$$ Equation 3-14

where:

p_{tr} is the mean stress in the concrete (orthogonal to the bar axis) averaged over a volume around the bar with a diameter of 3 Ø.

3.1.3.3 Effect of longitudinal cracks

The coefficient of modification related to cracks along the bar axis could be as following:

$\Omega_{cr} = 1$ concrete is uncracked parallel to the bar axis

$$\Omega_{cr} = 1 - 1.2\, w_{cr} \qquad \text{Equation 3-15}$$

concrete is cracked parallel to the bar axis and w_{cr} is the crack width in mm

A transverse tensile stress equal to the concrete's tensile strength can cause the concrete cover to split, resulting in a complete loss of bond resistance if no reinforcement crosses the splitting crack. Equation 3-15 describes the scenario where reinforcement intersects potential splitting cracks without being stressed beyond its yield strength. This equation is considered applicable for cracks up to 0.5 mm wide.

3.1.3.4 Effect of cyclic loading

Reserved cyclic loading decreases the bond capacity more than monotonic loading. The *Figure 3-6* will describe how dissipated energy is calculated in cyclic loading and monotonic one by showing bond-slip relationship and description of dissipated energy.

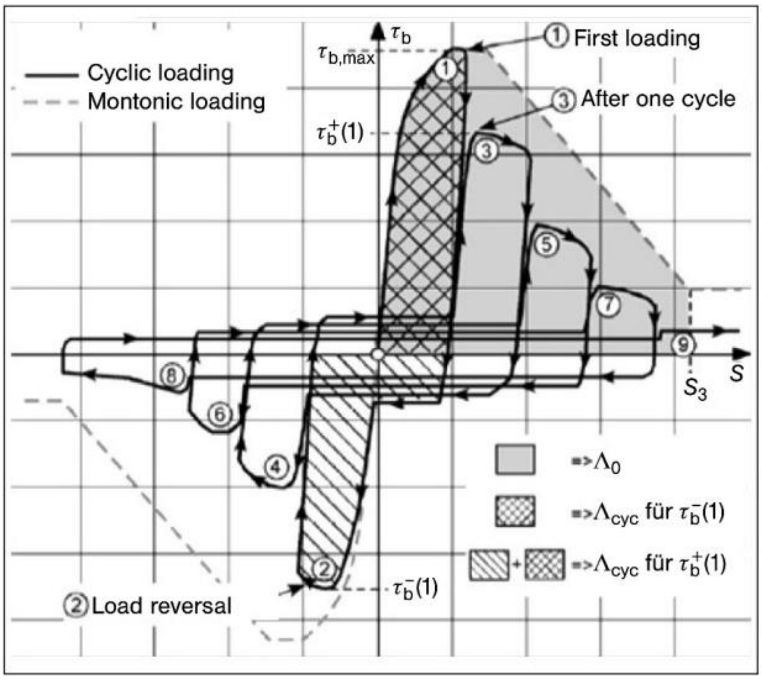

Figure 3-6 _ Description of dissipated energy in case cyclic and monotonic loading in terms of bond-slip relationship, (Model Code, 2010)

Ω_{cyc} is based on ratio Λ_{cyc}/Λ_0

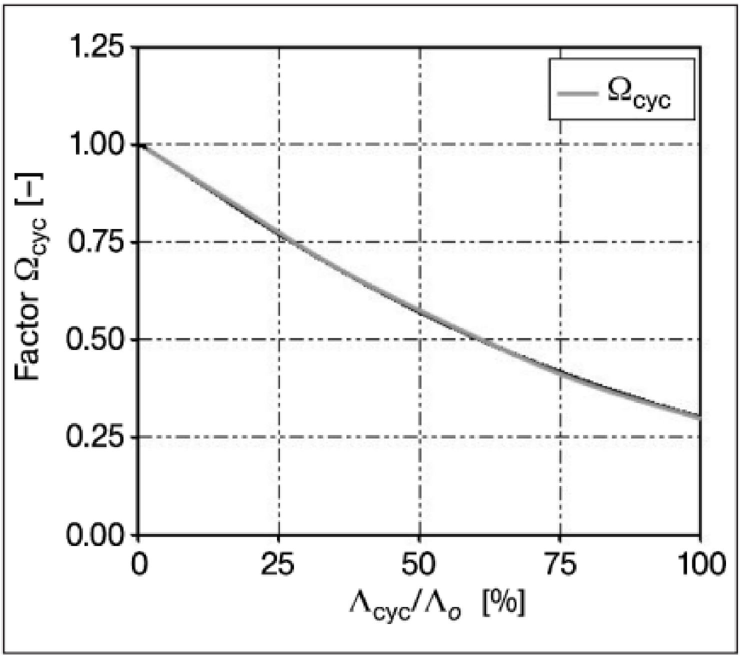

Figure 3-7 _ Ω_{cyc} trend vs ratio of dissipated energy in cyclic and monotonic load, (Model Code, 2010)

Ω_{cyc} based on ratio Λ_{cyc}/Λ_0

When the bond stress climbed to τ_{bmax} the modification of bond-slip curve can be done in pull-out failure according to Ω_{cyc}:

$\Omega_{cyc} = e^{\left(-1.2\left(\frac{\Lambda_{cyc}}{\Lambda_0}\right)^{1.1}\right)}$ Equation 3-16

Where:

Λ_{cyc} is dissipated energy during cyclic loading (Figure 3-7)

Λ_0 is dissipated energy during monotonic loading (Figure 3-7)

3.1.4 Unloading Part

There is a linear unloading part in the bond-slip graph and is acceptable for the growing the horizontal step of graph and the slope S_s (Figure 3-8) is not dependent on s and can be calculated by the following equation:

$S_s = 6\,\tau_{bmax}[N/mm3]$ Equation 3-17

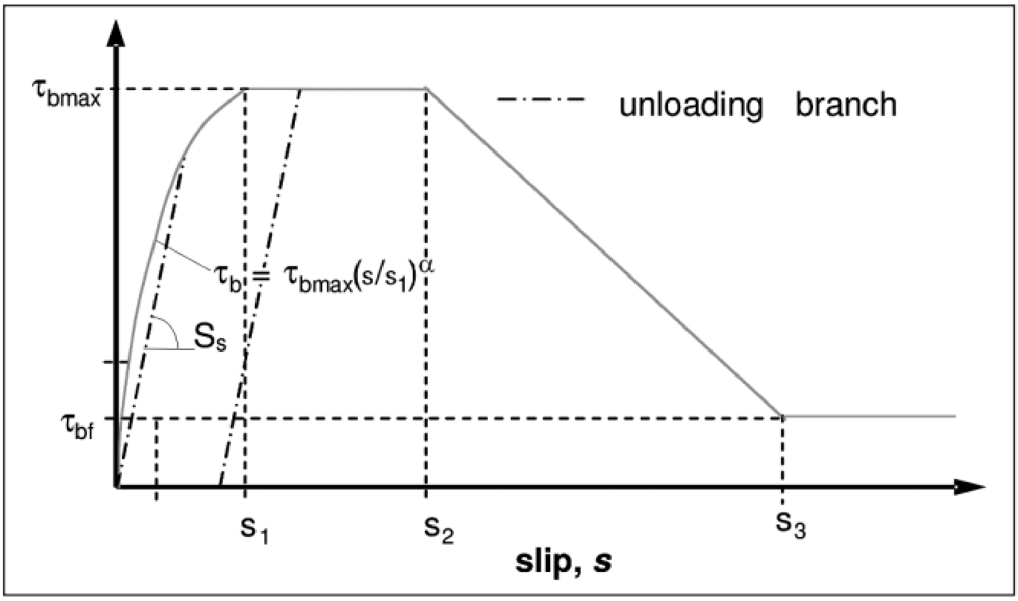

Figure 3-8 _ Bond-slip relationship in unloading part, (Model Code, 2010)

3.1.5 Basic Bond Strength

The reinforcing steel stress f_{ctm} could be obtained by a semi-empirical formula of Equation 3-5 when the ribbed bar is in a “good” concreting situation. This equation has been validated using the results of around 800 tests.

$$f_{stm} = 54(\frac{f_{cm}}{25})^{0.25}(\frac{25}{\emptyset})^{0.2}(\frac{l_b}{\emptyset})^{0.55}\left[(\frac{c_{min}}{\emptyset})^{0.25}(\frac{c_{max}}{c_{min}})^{0.1} + k_m k_{tr}\right]$$

$$f_{stmbd,0} = \eta_1\eta_2\eta_3\eta_4\left(\frac{f_{ck}}{5}\right)^{0.5}/\gamma_c \qquad \text{Equation 3-18}$$

By $f_{stm} \leq f_y$, and $f_{stm} \leq 2.5\sqrt{f_c}4(\frac{l_b}{\emptyset})$ or $f_{stm} \leq 12.5\sqrt{f_c}4(\frac{l_b}{\emptyset})$ in good and poor bond situation in order. The Equation 3-5 is applicable when 15 MPa < f_{cm} <110 MPa, 0.5 <$\frac{c_{min}}{\emptyset}$ < 3.5, 1< $\frac{c_{max}}{c_{min}}$<5 and k_{tr} < 0.05. The parameters are explained in Equation 3-6.

The f_{stm} represents an average value and might not be suitable for direct application in design processes. Equation 3-5 was formulated based on experiments conducted on bars with a relative rib area, f_r, ranging from 0.05 to 0.14. Different rib patterns might achieve greater bond strengths. Therefore, the correct η_1 value should be adjusted based on specific testing. The

Equation 3-18 is obtained from Equation 3-5 as following:

A_ A feature strength explanation is driven by modifying the coefficient of 54 in the mean strength explanation of Equation 3-5 to 41 via evaluation of statistical closeness of the explanation.

B_ The Equation 3-5 is rewritten to permit embedded length l_b to improve design strength of steel $f_y = f_{yk}/\gamma_c$ for determining by f_{yk} equal to 500MPa.

C_ $f_{bd,0}$_ has been driven via setting the section of Equation 3-5 in square brackets for an amount of 1 and dividing bar force by nominal bar surface when f_{yd} is improved, $(f_{yd}A_s/\emptyset\pi l_b)$.

D_ Numbers for cover and confining reinforcement that meet the minimum detailing needs are input, and the indices and coefficients are rounded to more practical values.

The bond strength of steel not located in a “good” concreting location may be weakened due to the compaction of fluid concrete beneath the steel. This decrease in bond strength is generally more pronounced in deeper pours. Strategies to reduce plastic settlement cracking can also help minimize the bond reduction in less favorable casting positions. The suggested coefficient for η_2 is on the preservative side of the values observed in laboratory tests.

The parameters of

Equation 3-18 are explained as following:

ŋ$_1$ is 1.75 for ribbed bar and 1.4 for fusion bonded epoxy coated steels

ŋ$_2$ is related to casting location of steel in concreting, and is 1 for good bond conditions and 0.7 for other situations

ŋ$_3$ is 1 for bar diameter less than 25mm and $(\frac{25}{\o})^{0.3}$ for bar diameter more than 25mm

ŋ$_4$ demonstrates the the characteristic strength of anchored or lapped bar and is 1 for f_{yk}=500 MPa, 1.2 for f_{yk}=400 MPa, 0.85 for f_{yk}=600 MPa, 0.75 for f_{yk}=700 MPa, 0.68 for f_{yk}=800 MPa.

γ_c is 1.5 which is a partial safety factor.

The design ultimate bond strength f_{bd} of ribbed bars might be changed from the basic value while concrete cover, bar spacing or transverse steel vary from their considered value or in the case that there is transverse pressure.

$$f_{bd} = (a_2 + a_3)f_{bd,0} - 2p_{tr}/\gamma_c < 2.5f_{bd,0} - 0.4p_{tr}/\gamma_c < 1{,}5\sqrt{f_{ck}}/\gamma_c$$

Equation 3-19

Where:

α2 and α3 reflect the effects of passive confinement due to cover (α2) and transverse steel (α3). If the minimum detailing needs are met, α2 can conservatively be assumed as 1.0, while α3 can conservatively be considered as 0.

p_{tr} is the average compressive stress that is perpendicular to the potential failure surface at the ultimate limit state. In cases where compression acts transversely and perpendicular to the bar axis over part of the embedded length, the bond strength can be enhanced within that section. The term p_{tr} becomes negative when there is compressive transverse force.

3.2 Model Proposed by Wang (Wang, 2023)

The bond behaviour between prestressed steel strands and concrete is crucial for the integrity of PC structures. For easier calculation, this bond can be simplified as the shear stress occurring on the steel interface. Steel strands are exposed to corrosion, particularly when exposed to chloride ions in harsh environments. Corrosion damages the contact surface and leads to cracking in the concrete, ultimately compromising the bond strength of the strands. Numerous studies have studied the bond behaviour of corroded reinforcement in RC structures, including experimental investigations, theoretical analyses, and numerical models. Most research on how corrosion affects bond strength has been experimental, with a significant focus on the central pull-out test. These experiments reveal that the bond strength of steel strands initially increases with the onset of corrosion but begins to decline after reaching a critical corrosion threshold, eventually stabilizing. Empirical formulas based on these test results have been developed to assess the reduction in bond strength due to corrosion. Nevertheless, these predictive results are strongly influenced by test conditions and have limited applicability in real-world engineering situations. In contrast to fib Model Code 2010 that focus more on ribbed reinforcements, Wang has introduced theoretical study on the corroded strands which could be more applicable in our research.

3.2.1 Effect of Rotation on Bond Strength of Strand

The seven-wire prestressed steel strand is commonly employed in bridge construction. This strand is composed of six outer wires twisted and wrapped around a central wire. Because of its twisted configuration, the strand often causes concrete splitting or rotation when it reaches its maximum bond strength. In pull-out beams using seven-wire steel strands, two common bond failure modes can be observed: concrete splitting failure and pull-out failure. The degree of confinement provided by the concrete around the strand defines which of these failure modes occurs, leading to variations in bond strength. Concrete splitting failure happens when the surrounding concrete fractures totally, as illustrated in Figure 3-9, typically occurring when the strand is not adequately confined by the concrete cover. Conversely, pull-out failure happens under conditions of adequate confinement. In such cases, the twisted structure of the strand causes it to slip rotationally before the concrete reaches its ultimate confinement stress, without causing complete splitting, as demonstrated in Figure 3-10. Several factors, including the strand's surface features, concrete cover value, and the concrete tensile strength, influence the failure mode. Moreover, the size of the aggregate may affect the failure mode by affecting the interlock of ribbed bars.

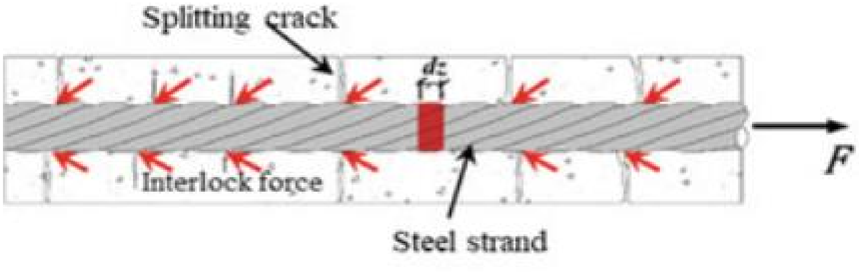

Figure 3-9 _ Splitting failure description, (Wang, 2023)

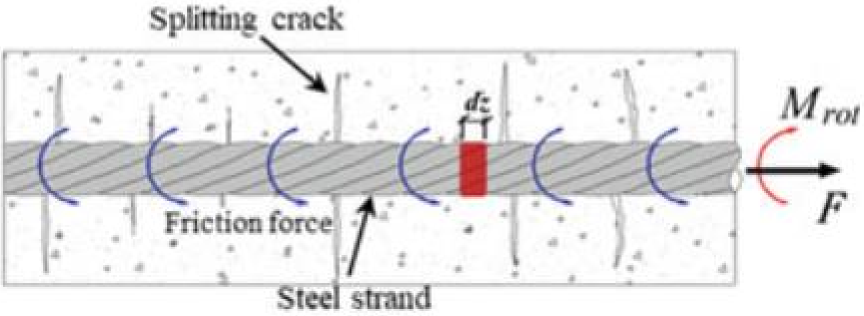

Figure 3-10 _ Pull-out failure description, (Wang, 2023)

Generally, to prevent splitting failure in PC structures, sufficient concrete cover and additional steel could be designed around the steel strands, causing pull-out failure being the more typical failure type. Nevertheless, the pull-out failure of strands varies from that of ribbed bars. When there is pull-out failure, the strands do not simply withdraw from the concrete block. Instead, the steel strand moves out in a helical pattern along a tunnel formed within the concrete. This rotational behaviour is dictated by the bond mechanism of the strand.

3.2.2 General Explanation for Bond Strength

This section introduces a predictive model for bond strength, focusing on the pull-out failure mode involving strand rotation. Typically, the bond stress between steel and concrete is considered a consistent shear stress along the bond interface. For an individual seven-wire steel strand, the average bond stress, denoted as τb, is expressed as:

$$\tau_b = F_p/(i.\pi.d.l_t) \qquad \text{Equation 3-20}$$

Where:

F_p is tensile force

l_t is bond length

D is nominal diameter of strand

I is perimeter factor which is equal to 1.33 for seven-wire strand

A steel strand is composed of six helical wires wrapped around a central straight wire. Because of the helical configuration of the outer wires, the cross-sectional visualization of the strand along its length do not perfectly align within the lay length. The lay length is defined as the distance that the outer wires traverse around the central wire. For analysis, the steel strand is divided longitudinally into some equal sections, each with a height of dz. Figure 3-11 illustrates a segment of the strand. As shown, the longitudinal extension of length dz corresponds to a rotation of dα on the strand's projection plane. It is assumed that the six outer wires twist consistently around the core wire. The relationship between dα and dz is given by Equation 3-21, where l_{lay} represents the lay length of the strand. Based on the ASTM A416 standard, l_{lay}can be almost estimated as 14d. Moreover, the rotation of the outer wires around the central wire creates an inclined angle δ (as shown in Figure 3-11), which can be expressed as Equation 3-22.

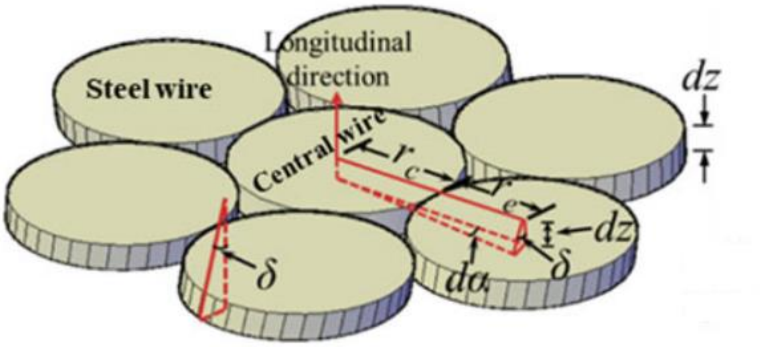

Figure 3-11 _ Schematic diagram of a strand segment with the height of dz, (Wang, 2023)

Where:

r_c is the core wire radius

r_e is the outer wire radius

$$\frac{d_a}{2\pi} = \frac{d_z}{l_{lay}} \qquad \text{Equation 3-21}$$

$$\tan\delta = \frac{(r_c + r_e)d_a}{d_z} \qquad \text{Equation 3-22}$$

Regarding strands with precise diameters and l_{lay}, the angle δ could be calculated using Equation 3-21 and Equation 3-22. Thus, when the lay length is 14d, δ is assumed to be 8.7° for various strand diameters. Mechanical interlock occurs on the helical ribs due to the sloped planes relative to the longitudinal direction. Figure 3-12a displays the projection of one segment along the strand's length, with the shaded area representing the region where the rib presents the interlocking force. This shaded area can be estimated as six fragmentary crescent shapes. Supposing each exterior wire of the strand exerts the same force, another crescent-shaped rib was selected for analysis, as illustrated in Figure 3-12b. The normalized crescent-shaped rib resembles the rib of a ribbed bar. Because of the helical nature of the exterior wires, the bearing surfaces are helical on the strand's longitudinal axis, leading to complicated boundary conditions. It is supposed that mechanical interlocking is due solely to the tangential displacement of the exterior wire, rather than the rotation of the core wire, allowing the helical face to be approximated as flat. Thus, the crescent-shaped rib can be used to simulate the rib of ribbed bars. The force evaluation for ribbed bars is analogous to that for the strand. Regarding a interior embedded strand, supposing that the boundary conditions for the six exterior wires are uniform at a given cross-section. Consequently, one steel wire is selected for mechanical tests. Note that the steel strand is treated as a whole, and the interactions between the steel wires are not considered.

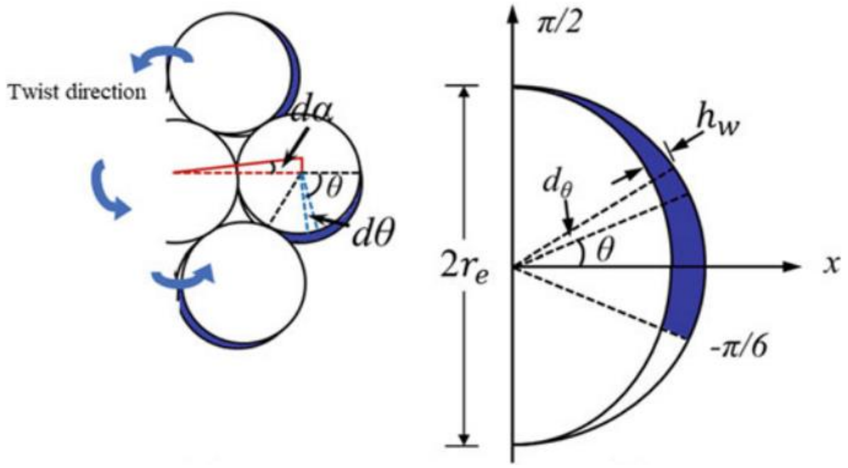

(a) (b)

Figure 3-12 _ (a) Projection of a part parallel to longitudinal direction of strand, (b) Effective bearing surface of exterior wire, (Wang, 2023)

Accounting the forces applying on a rib segment subtended via dθ, shown in the Figure 3-12.

The dA can be calculated as following:

$$d_A = \frac{h_w}{\sin\delta \,.\, r_e . d_\theta}$$ Equation 3-23

Where:

h_w is rib height

Θ is the effective coverage angle for not complete crescent (-п/6, п/2)

Figure 3-13 illustrates an evaluation of the mechanical interlock force affecting an individual rib.

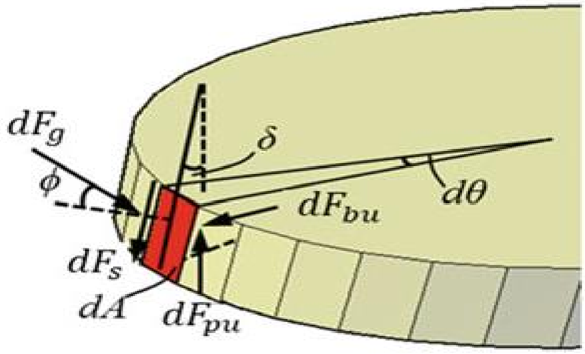

Figure 3-13 _ Force analysis on a single rib, (Wang, 2023)

The assumption is made that pull-out failure occurs when the shear stress at the bond interface surpasses the adhesion strength and the frictional resistance between the helical ribs and the concrete. The forces generated by the mechanical interlock on the rib's surface can be divided into two components: dF_g, which is angled at $\emptyset$ relative to the rib surface, and dF_s, which runs parallel to the rib surface. dF_s and dF_g can be calculated as following:

$$dF_s = \sigma_c d_A \qquad \text{Equation 3-24}$$

$$dF_g = \sigma_n d_A / \cos\emptyset \qquad \text{Equation 3-25}$$

Where:

σ_c is unit cohesion of bearing face and concrete (0.11 fc)

$\emptyset$ is friction angle between steel and surrounding concrete

σ_n is normal stress on shear failure plane

dF_s and dF_g could be divided into parameters dF_{pu} and dF_{bu}, the formula is as following:

$$dF_{pu} = \left(\frac{\sigma_n d_A}{\cos\emptyset}\right).\sin(\delta + \emptyset) + \sigma_c d_A.\cos\delta \qquad \text{Equation 3-26}$$

$$dF_{bu} = \left(\frac{\sigma_n d_A}{\cos\emptyset}\right).\cos(\delta + \emptyset) - \sigma_c d_A.\sin\delta \qquad \text{Equation 3-27}$$

Where:

dF_{pu} is along the longitudinal direction of strand

dF_{bu} is perpendicular the longitudinal direction of strand

Integral of Equation 3-30 will lead to total resisting force F_p as following:

$$F_p = 6\int_{\frac{-\pi}{6}}^{\frac{\pi}{2}} dF_{pu} d\theta = 6\left[\left(\frac{\sigma_n}{\cos \emptyset}\right).\left(\frac{\sin(\delta + \emptyset)}{\sin \delta}\right) + \sigma_c.\cot \delta\right].A_r$$

Equation 3-28

$$A_r = (\frac{2}{3})\left\{\left(\frac{\pi d_e}{4}\right) - \left(\frac{\pi d_e}{2}\right)\left[\left(\frac{d_e}{2}\right) - (\frac{d_e + d_c}{2})d_a\right]\right\}$$

Equation 3-29

Then the total resisting force F_p which is in valid in dz and the average bond stress could be calculated as following:

$$F_p = 2\left(\left(\frac{\sigma_n}{\cos \emptyset}\right).\left(\frac{\sin(\delta + \emptyset)}{\sin \delta}\right) + \sigma_a.\cot \delta\right) + \text{п} d_e{}^2 d_a$$

Equation 3-30

$$\tau_b = (3\pi/14)(d_e/d)^2\left(\left(\frac{\sigma_n}{\cos \emptyset}\right).\left(\frac{\sin(\delta + \emptyset)}{\sin \delta}\right) + \sigma_c.\cot \delta\right)$$

Equation 3-31

Where:

d_e is the diameter of exterior wire

d_c is the diameter of core wire

A_r is the area of a not complete crescent

Equation 3-31 indicates that τ_b is influenced by several factors, such as the ratio of the exterior wire diameter to the nominal strand diameter d_e/d, the friction angle ($\emptyset$), the inclination angle of the strand ribs (δ), the bond strength between the concrete and strand (σ_c), and the normal stress at the shear interface (σ_n). The subsequent section details the calculation of the normal confining stress (σ_n), taking into account the rotation of the strand. In cases where beams experience pull-out failure accompanied by strand rotation, integrating the radial component of the mechanical interlock, dF_{bu}, generates a bursting force, F_{rib}, around the exterior wires Figure 3-14.

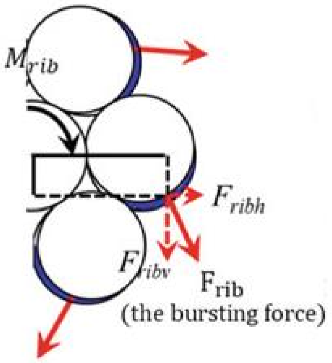

Figure 3-14 _ Torque generated by bursting force, (Wang, 2023)

$$F_{ribv} = \int_{\frac{-\pi}{6}}^{\frac{\pi}{2}} dF_{pu} \cos\theta \, d\theta = 3/4 \left[\left(\frac{\sigma_n}{\cos\emptyset} \right) . \left(\frac{\cos(\delta + \emptyset)}{\sin\delta} \right) - \sigma_c \right] . h_w d_e \quad \text{Equation 3-32}$$

$$F_{ribh} = \int_{\frac{-\pi}{6}}^{\frac{\pi}{2}} dF_{pu} \sin\theta \, d\theta = \sqrt{3}/4 \left[\left(\frac{\sigma_n}{\cos\emptyset} \right) . \left(\frac{\cos(\delta + \emptyset)}{\sin\delta} \right) - \sigma_c \right] . h_w \quad \text{Equation 3-33}$$

$$F_{rib} = \sqrt{{F_{ribv}}^2 + {F_{ribh}}^2} = \sqrt{3}/4 \left[\left(\frac{\sigma_n}{\cos\emptyset} \right) . \left(\frac{\cos(\delta + \emptyset)}{\sin\delta} \right) - \sigma_c \right] . h_w \quad \text{Equation 3-34}$$

$$M_{rib} = 9/2 \left[\left(\frac{\sigma_n}{\cos\emptyset} \right) . \left(\frac{\cos(\delta + \emptyset)}{\sin\delta} \right) - \sigma_c \right] . h_w \quad \text{Equation 3-35}$$

As a result of the helical configuration of the exterior wires, a torque, M_{rib}, is exerted on the steel strand. When this torque surpasses the frictional capacity, the strand starts to rotate helically. During this rotation, the bond strength and confining stress of the steel strand both achieve their maximum values. Consequently, the normal stress, σ_n, associated with pull-out failure in beams where strand rotation occurs, is identified as the critical confining stress, $\sigma_{n,crie}$. This critical stress can be determined by analyzing the moment balance around the center of the strand. The torque, M_{fri} is a result of frictional force which is around the wires and is supposed to be uniformly on the whole rib surface, shown in fff.

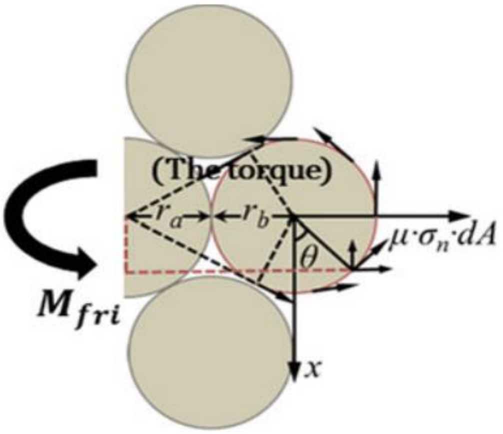

Figure 3-15 _ Torque produced via frictional force, (Wang, 2023)

The mentioned torque could be calculated by the following formula:

$$\frac{M_{fri}}{12} = \int_{\frac{-\pi}{6}}^{\frac{\pi}{2}} \frac{\mu\sigma_n dAd_e \cos\theta^2}{2} + \int_{\frac{-\pi}{6}}^{\frac{\pi}{2}} \mu\sigma_n dAd_e \sin\theta \, (\frac{d_e + d_c}{2} + \frac{d_e}{2}\sin\theta$$

Equation 3-36

$$M_{fri} = (3\sqrt{3} + 2\pi)(\mu\sigma_n {d_e}^3 d_a$$

Equation 3-37

Considering strand rotation, we can write the formula for bond stress like following:

Equation 3-38

$$\sigma_{n,crie} = \left(\frac{1}{\left[\left(\frac{\cos(\delta + \emptyset)}{\sin\delta\cos\emptyset}\right) - \left(\frac{2\sqrt{3}}{3} + \frac{4\pi}{9}\right)\left(\frac{\tan\emptyset}{\sin\delta}\right)\right]}\right).\sigma_c$$

$$\tau_b = (3\pi/14)(d_e/d)^2\left(\left(\frac{k.\sigma_c}{\cos\emptyset}\right).\left(\frac{\sin(\delta + \emptyset)}{\sin\delta}\right) + \sigma_c.\cot\delta\right)$$

Equation 3-39

$$K = \left(\frac{1}{\left[\left(\frac{\cos(\delta + \emptyset)}{\sin\delta\cos\emptyset}\right) - \left(\frac{2\sqrt{3}}{3} + \frac{4\pi}{9}\right)\left(\frac{\tan\emptyset}{\sin\delta}\right)\right]}\right)$$

It should be mentioned that only in having well-constrained situation in which the failure occurs with strand rotation, $\sigma_{n,crie}$ should be calculated by Equation 3-38. Also, it is notable that the $\sigma_{n,crie}$ might be less that the peak confining stress if there be adequate confinement by concrete in the section.

In this case, the critical bond stress, $\sigma_{n,crie}$, could be applied in place of the peak confining stress to prevent an estimation of overvalue of the bond stress. The σ_n within the concrete is described demonstrating normal stress acting on the shear failure plane, which is nearly perpendicular to the strand axis. The formation of σ_n is almost linked to the helical features of the steel strand. Because of the helical ribs, the strand tends to move upright to the bond face, leading radial confining stress in surrounding area. As a result, this radial confining stress and the normal stress σ_n is considered similar. The mentioned concepts have been validated by (Wang, 2023) via testing several experimental cases.

3.2.3 Model for Bond–Slip Between Corroded Strand and Concrete

In this part a local bond stress-slip relationship regarding the interaction of corroded steel strand and concrete which is introduced by (Wang, 2023) will be explained. To support the theory, experimental observations regarding force-displacement graph have also been used. To normalize the calculations, the PC beam is separated to several segments, numbering from 1 to n and having length equal to l_i , shown in Figure 3-16.

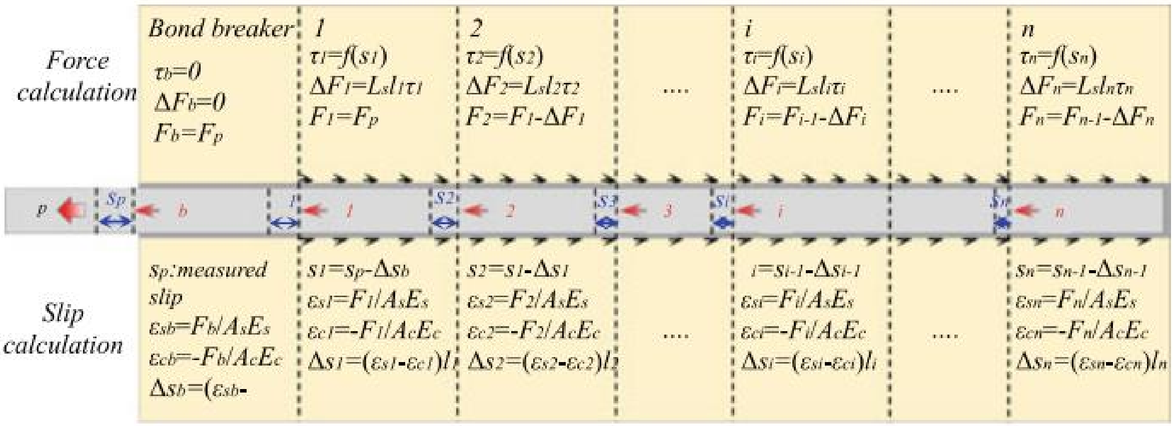

Figure 3-16 _ Schematic figure of the numerical approximation, (Wang, 2023)

Where:

A_c is concrete cross-section area

A_s is strand cross-section area

l_s is strand circumference

The beam is assumed to be under loading equal to F_p and the load and slip are computes as the average value in each part. The procedure is working like following steps:

Step1: Suppose slip S_p measured at the loaded end and next compute S_1 which is the slip at section one.

Step2: in the first section the local bond stress and force should be computed.

Step3: compute the tension force in section two considering $F_1 = F_p$.

Step4: compute the strain of concrete and strand in section one.

Step5: compute the local slip in section one.

Step6: compute the slip in section two.

F_2 and S_2 in section two have been determined. The numerical process is then repeated to compute F_i and S_i for each subsequent section (i) until the specified boundary conditions are satisfied. If these conditions are not met, the initial assumption for the loaded end slip S_p must be altered, and the entire procedure is repeated. Depending on the relationship between the bond length and the effective bond length, two different boundary conditions can be defined. First, for specimens that have long embedded lengths or under low pull-out loads, the pull-out force is only transmitted within the interior part of the specimen and does not reach the free end. In this scenario, the boundary condition is that both the tension force F_i and slip S_i of the steel strand at any segment (i) are zero. On the other hand, for specimens that have short bond lengths or high pull-out loads, the pull-out force is distributed across the whole bond area, and the boundary condition in this case is that the tension force F_n at the free end of the strand is zero. If the strand yields in the pull-out test, the effect of plastic deformation might be better to be accounted for when computing the strain ε_s of the strand. The elastic-plastic proposed models are as following:

$$\sigma = \begin{cases} \varepsilon E_s & \varepsilon < \varepsilon_{sy} \\ f_{sy} + E_{sp}\left(\varepsilon - \varepsilon_{sy}\right) & \varepsilon < \varepsilon_{sy} \end{cases} \qquad \text{Equation 3-40}$$

$$\varepsilon_{si} = \begin{cases} F_i / A_s E_s & F_i \leq A_s f_{sy} \\ \varepsilon_{sy} + \dfrac{F_i}{A_s E_{sp}} - f_{sy}/E_{sp} & F_i > A_s f_{sy} \end{cases} \qquad \text{Equation 3-41}$$

Where:

f_{sy} is yield strength of steel

ε_{sy} is yield strain of steel

E_{sp} is steel hardening modulus

3.2.4 Local Bond–Slip Between Strand and Concrete

In previous research, numerous models have been proposed to represent the local bond stress–slip relationship in concrete structures. Figure 3-17a and Figure 3-17b illustrate two such models: a piecewise uniform function and a multivariate linear function, respectively. These models, nevertheless, are overly easy and do not adequately capture the complexities required for the current study. Figure 3-17c presents a logarithmic function, where bond stress steadily develops as the applied load grows. This model lacks a descending branch, which could result in unrealistically high bond stresses, failing to represent the true behaviour of the bond. The CEB Model Code offers a more nuanced approach by dividing the bond stress-slip relationship into four distinct zones. This model features a plateau at the peak bond stress to characterize the bond behaviour between a ribbed bar and concrete, as illustrated in Figure 3-17d. However, experimental data did not confirm the existence of such a plateau. To better represent the local bond behaviour between ribbed bars and concrete, the CEB Model Code suggests an enhanced version of the model as illustrated in Figure 3-18. This improved model eliminates the plateau and instead divides the bond stress-slip relationship into three zones: an initial nonlinear grow in bond stress until it reaches a peak, followed by a linear reduction in bond stress, and finally a zone of steady residual strength. The elimination of the peak bond stress plateau reflects a more accurate depiction of bond behaviour observed in experimental studies. Given the closeness in bond mechanisms between ribbed bars and concrete, this refined local bond stress–slip model can also be applied to describe the bond behaviour between steel strands and concrete. This adaptation ensures a more accurate and comprehensive understanding of the interaction between steel strands and the surrounding concrete matrix, crucial for the design and analysis of concrete structures.

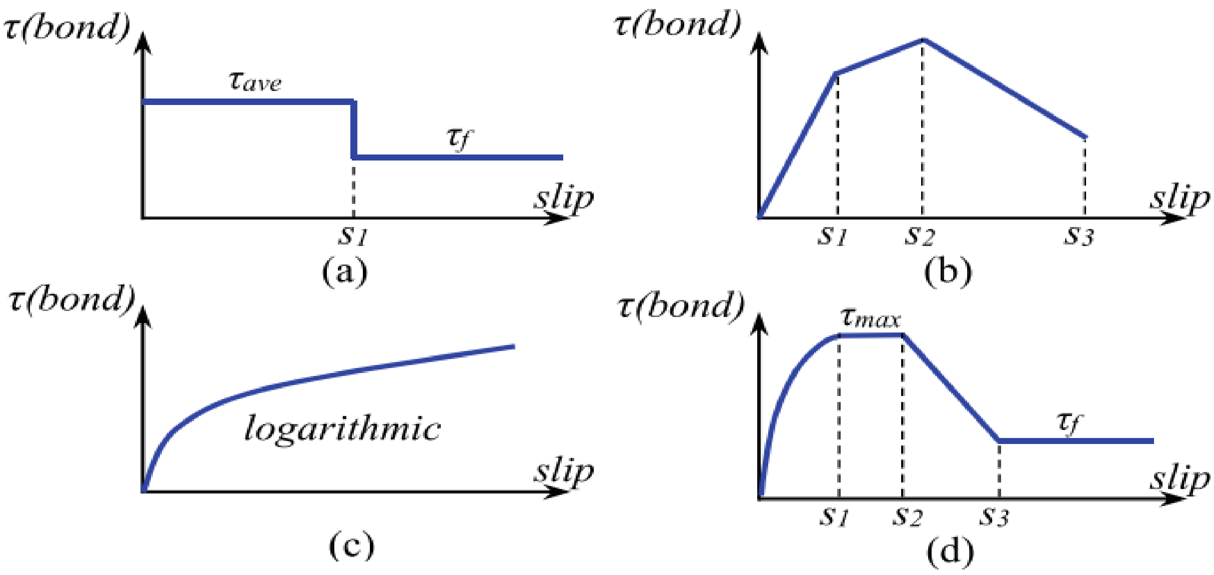

Figure 3-17 _ Described in detail above, (Wang, 2023)

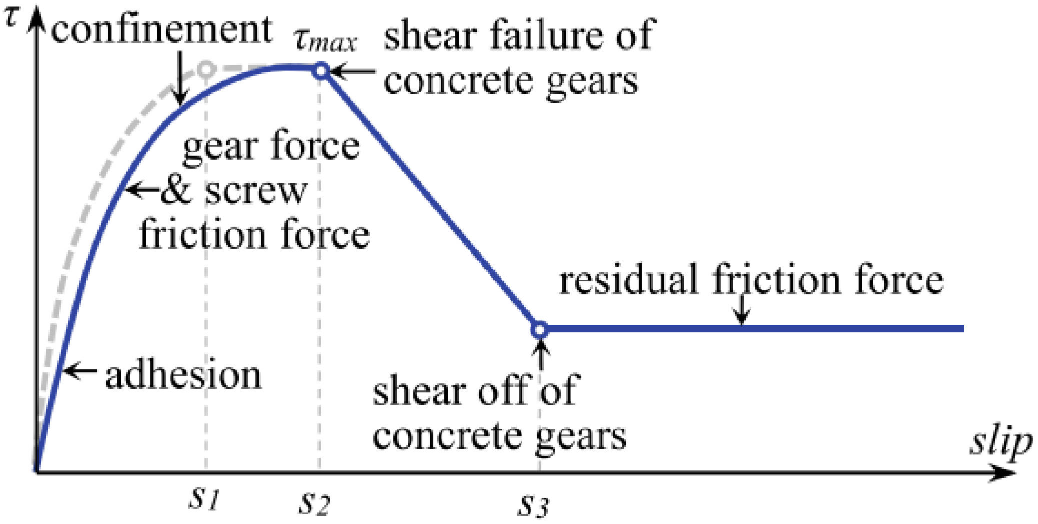

Figure 3-18 _ Bond-slip relationship proposed by (Wang, 2023)

This model offers a comprehensive explanation of the bond mechanism and the modes of bond failure. Initially, bond strength and stiffness are derived from the adhesive forces at the interface. As slip develop, these adhesive forces diminish progressively. Nevertheless, the concrete opposes the slip and rotation of the steel strands, leading to the development of frictional forces and mechanical interlocking at the contacting face of steel and concrete.

As the slip continues to grow, the bond stress rises accordingly, eventually reaching its peak. At this stage, localized crushing and the formation of micro-cracks begin to occur on the concrete's confining surface. As these deformations progress, bond stress starts to decline until excessive slip results in either shear failure or crushing of the concrete. Where the bond force is sustained mainly by longitudinal friction, which remains relatively low and stable.

In alignment with the CEB Model Code, the developed bond stress–slip model can be expressed as following:

$$\tau = \begin{cases} \tau_{max}(\frac{s}{s_2})^a & 0 \le s \le s_2 \\ \tau_{max} - (\tau_{max} - \tau_f)(\frac{s - s_2}{s_3 - s_2}) & s_2 \le s \le s_3 \\ \tau_f & s_3 \le s \end{cases}$$

Equation 3-42

Where:

τ_{max} is the maximum bond stress

τ_f is residual friction stress and could be considered as $0.4\tau_{max}$

a , s_2 and s_3 are constant

For ribbed bars, the maximum bond stress, τ_{max}, is determined by the formulas $1.25\sqrt{f_{ck}}$ for good bond conditions and $2.5\sqrt{f_{ck}}$ for other conditions, where f_{ck} represents the characteristic compressive strength of the concrete. The value of τ_f is then computed as 40% of τ_{max}. The parameters α and s_2 are typically assigned values of 0.4 and 3 mm, respectively, while s_3 denotes the clear distance between the ribs of the bars. As previously noted, the bond behaviour of strands embedded in concrete closely resembles that of ribbed bars. Consequently, the parameters used to describe the local bond features of strands are estimated based on those for ribbed bars. Given that strands do not have ribs, the parameter s3 is defined as half the distance between next wires and the concrete gear, expressed as $s_3 = 0.5s_l$, where $s_l = s_t$ / sin α, as shown in Figure 3-19 and Figure 3-20.

These parameters were applied to the local bond stress–slip model and validated using experimental data. For this model, τ_{max} was set to $1.25\sqrt{f_{ck}}$, and s_3 was assigned a value of 12.0 mm. Figure 3-21 illustrates that the calculated load–displacement curve at the loading end aligns closely with the experimentally observed diagram. The anticipated failure mode in experimental case, which involved strand breakage, also matched the experimental findings. This indicates that the local bond stress–slip relationship and the selected factors are appropriate for uncorroded strands.

However, for corroded beams, these factors must be redefined. As discussed currently, corrosion affects both bond strength and bond stiffness. According to Equation 3-42, bond stiffness is associated with the peak bond stress, and therefore, the local bond stress–slip relationship must be adjusted to account for the effects of corrosion on beams.

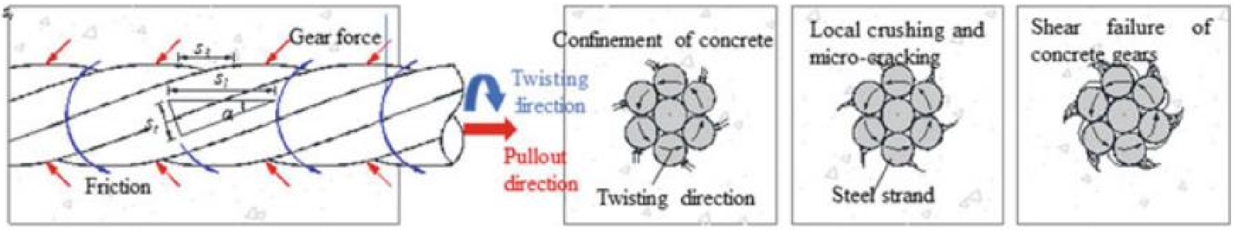

Figure 3-19 _ Embedded strand in concrete, (Wang, 2023)

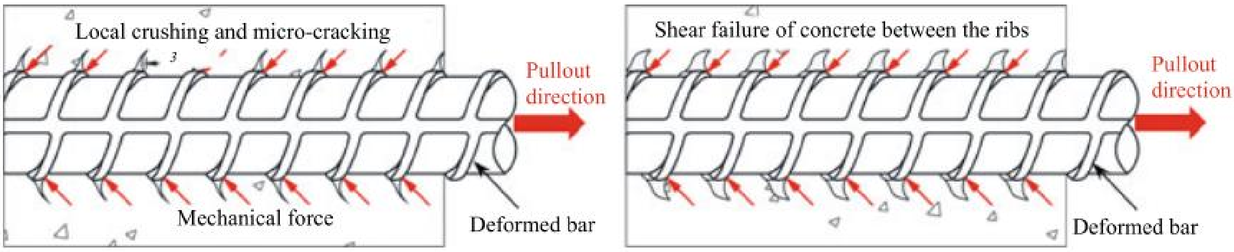

Figure 3-20 _ Embedded deformed bar in concrete, (Wang, 2023)

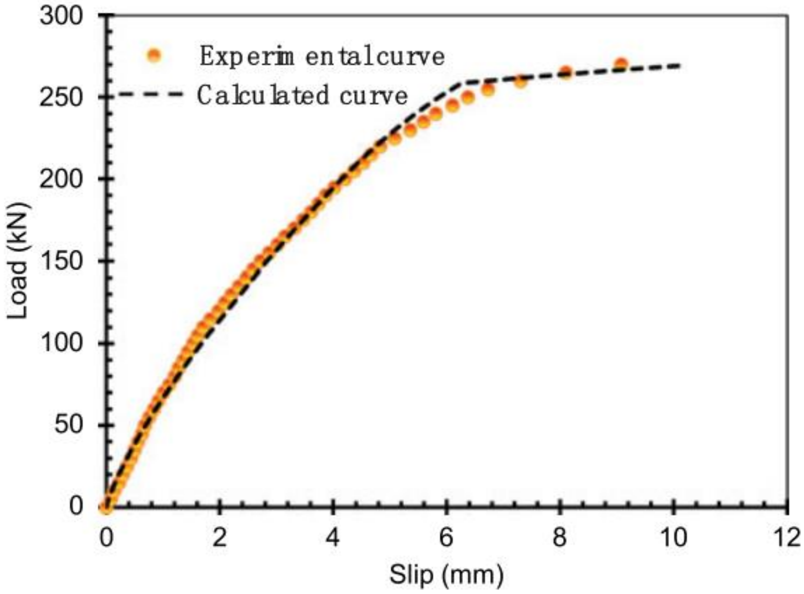

Figure 3-21 _ Comparison of load-displacement between experiment and computed one for the case of uncorroded, (Wang, 2023)

The maximum bond stress for corroded PC beams was calibrated based on experimental data. Figure 3-22 compares the experimental and defined force–displacement figure regarding corroded beams, showing a strong agreement between the calculated and observed results. This indicates that the local bond–slip relationship remains applicable to corroded elements when$\tau_{max}$is adjusted accordingly. In Figure 3-22, the peak bond stress, is indicated regarding corroded beams, where τ_{max} regarding uncorroded elements is typically$1.25\sqrt{f_{ck}}$. Interestingly, the τ_{max} regarding beams PS1 and PS2, which have lower corrosion ratio, exceed those of uncorroded beams. However, in cases of high corrosion τ_{max} regarding corroded members falls below that of uncorroded members, and it continues to reduce as the level of corrosion rises. To evaluate the impact of strand corrosion on bond performance, the normalized maximum bond stress, R, was used. R is described as the relationship of the maximum bond stress of a corroded member to that of its corresponding uncorroded element, as depicted in Figure 3-23. The figure also includes a satisfied graph showing the relationship between R and the corrosion loss, η. The data reveals that when corrosion loss is under 6%, R actually rises. Nevertheless, as corrosion progresses further, the normalized maximum bond stress declines sharply. Similar trends were observed in the bond behaviour of both corroded prestressed concrete (PC) and reinforced concrete (RC) specimens subjected to pull-out tests.

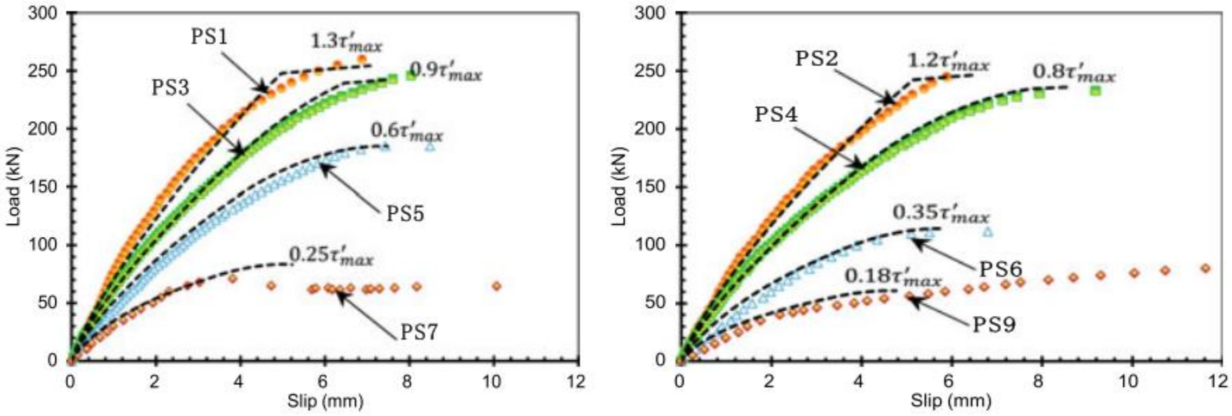

Figure 3-22 _ comparison between experimental and calculated load-displacement graph regarding corroded beams. Beams PS1 to PS9 are the name of beams used for study in this part, (Wang, 2023)

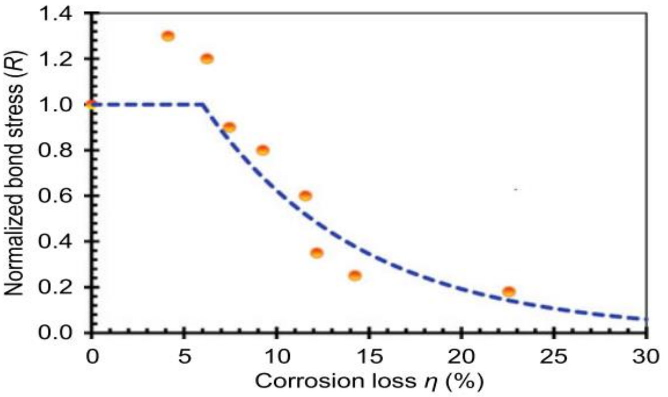

Figure 3-23 _ Effect of corrosion on bond stress, (Wang, 2023)

$$R = \begin{cases} 1 & \eta < 6\% \\ 2.03e^{-0.118\eta} & \eta < 6\% \end{cases}$$ Equation 3-43

To validate the empirical model's accuracy, a comparison was made between the anticipated and experimental load–displacement model for beam PS8 (name of a beam used in the experimental campaign), as illustrated in Figure 3-24. Prior to significant slip occurring in the strand, the anticipated trend aligns closely with the experimental data. However, once the slip becomes excessive, the grow in pull-out force is affected by the uncorroded portion of the strand at the free end, which is not accounted for by the empirical model, resulting in some discrepancies. Overall, the empirical model demonstrates strong anticipative exactness regarding bond deterioration between corroded strands and concrete.

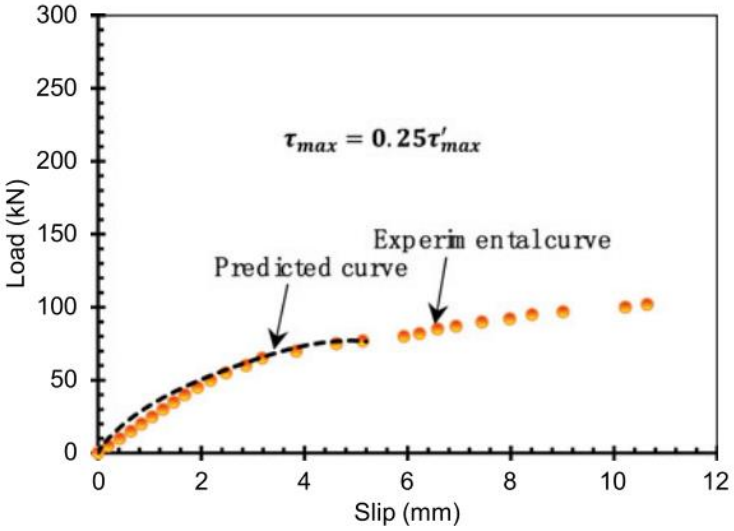

Figure 3-24 _ Comparison between the anticipated and experimental load–displacement model for beam PS8, (Wang, 2023)

The study observed an enhancement in bond strength for low corroded strands, which benefits concrete components. Nevertheless, this model does not incorporate the potential grow in bond strength. For corrosion losses below 6%, the normalized bond strength ratio (R) for the steel strand is presumed to be constant at 1.0. When corrosion loss exceeds 6%, R declines considerably. Despite these limitations, the empirical model remains effective for anticipating the residual bond strength of corroded strands embedded in concrete.

4 Methodology

The widespread use of prestressed concrete (PC) in the construction of numerous structures and infrastructures emphasizes the critical importance of understanding their durability and load-bearing capacity. As these structures age, it becomes increasingly important to identify and mitigate the factors that can compromise their performance. In recent years, there has been a growing focus on the factors that degrade these structures over time, with a particular emphasis on finding optimal strategies for maintaining their structural integrity.

One of the most significant challenges faced by PC structures is the corrosion of steel strand embedded in the concrete. Corrosion has been identified as a primary factor that diminishes both the ultimate and residual capacity of these structures and alters their failure modes. This is important due to the detrimental impact of corrosion on the bond between the steel strand and the surrounding concrete. The degradation of this bond can lead to severe consequences, including compromised structural safety and increased economic costs due to the need for repairs and maintenance. Therefore, it is essential to study how corrosion affects the bond behaviour in PC structures and, more importantly, how the deterioration of this bond influences the overall structural performance.

In this research, three naturally corroded beam-end specimens extracted from a full-scale prestressed concrete beam, without stirrups, which had been in service for over a decade as part of a thermal power plant structure have been evaluated in the laboratory at the Polytechnic University of Turin. During this period, the beam was subjected to repeated cycles of wetting and drying with marine water, resulting in natural corrosion. Each beam-end specimen was sequentially tested to failure. After testing, the tested section was removed, and the remaining portion of the beam was prepared for subsequent tests.

These tests were designed to closely simulate real-world conditions, Figure 4-1, as naturally corroded beams were chosen over artificially corroded ones, based on literature suggesting that artificial corrosion may not accurately replicate the effects of natural corrosion processes. During the tests, data was carefully recorded using gauges to monitor the performance of the PC beams under load. Additionally, the tests were monitored using the Digital Image Correlation (DIC) technique, which provided valuable insights into the strain distribution and displacement patterns of the beam-end specimens.

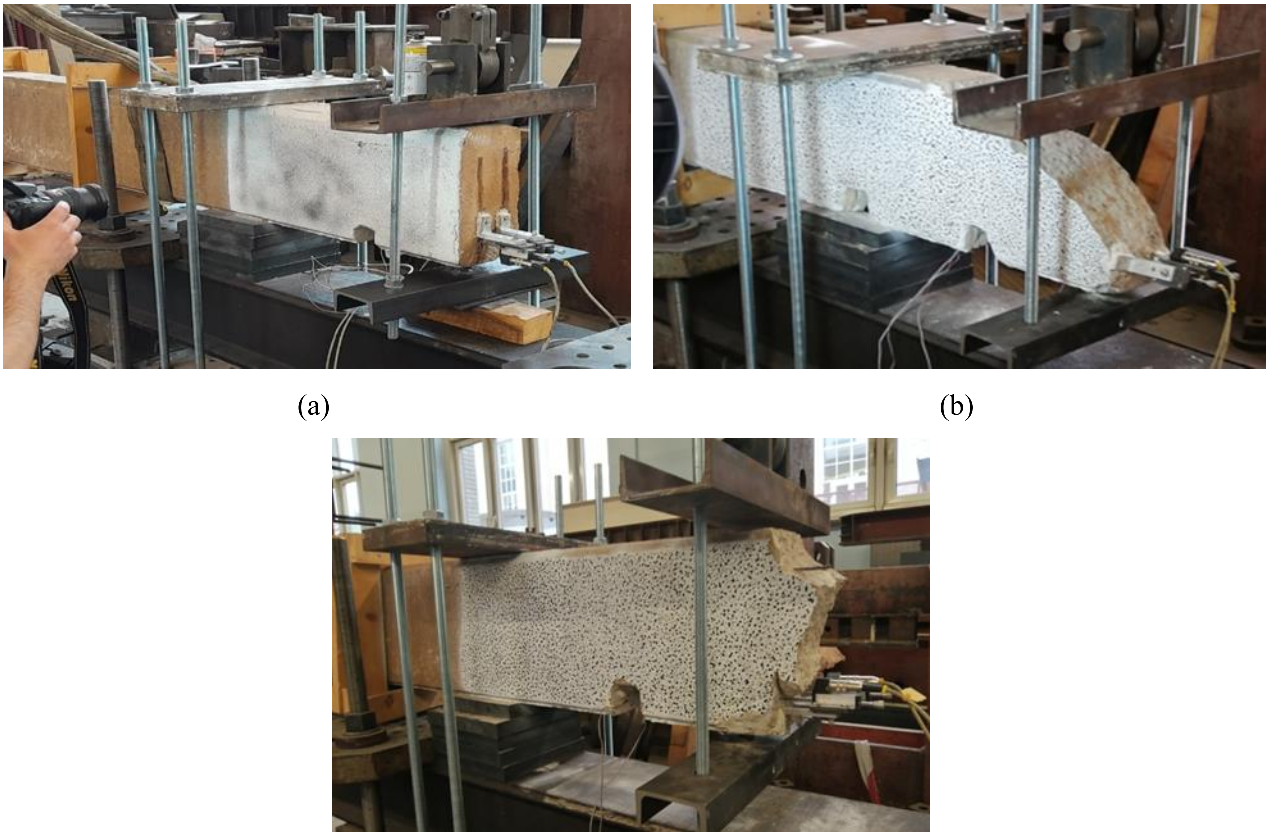

(a) (b)

(c)

Figure 4-1 _ (a) Beam-end specimen in test 1, (b) Beam-end specimen in test 2, (c) Beam-end specimen in test 2

To further enhance the understanding of bond behaviour between the pretensioned strands and the surrounding concrete, nonlinear finite element analyses (NLFEA) were conducted using Abaqus software. These simulations aimed to replicate the experimental conditions and provide a more detailed understanding of the bond mechanisms at play. The NLFEA models were calibrated by experimental data to ensure accuracy. To achieve a more precise simulation of the beam characteristics and behaviour, the UMAT subroutine was employed within the software. Each aspect of this study, from the experimental procedures to the numerical modeling, will be discussed in detail in the subsequent sections of this thesis. This comprehensive approach is intended to contribute to the broader understanding of the bond degradation impact on PC structures.

4.1 Experimental Program

An experimental investigation was conducted to examine the impact of corrosion on bond properties and load-bearing capacity in prestressed concrete (PC) beams with natural corrosion and without any transverse reinforcement. The PC beam served as structural elements in a thermal power plant and experienced 10 years of exposure to refrigerating wetting cycles involving marine water. During this period, the beam was susceptible to chloride-induced corrosion, which was exacerbated by the cyclical exposure to seawater, Figure 4-2. The beam has been divided as three sperate beam-end specimen to be prepared for the tests, Figure 4-1.

(a)

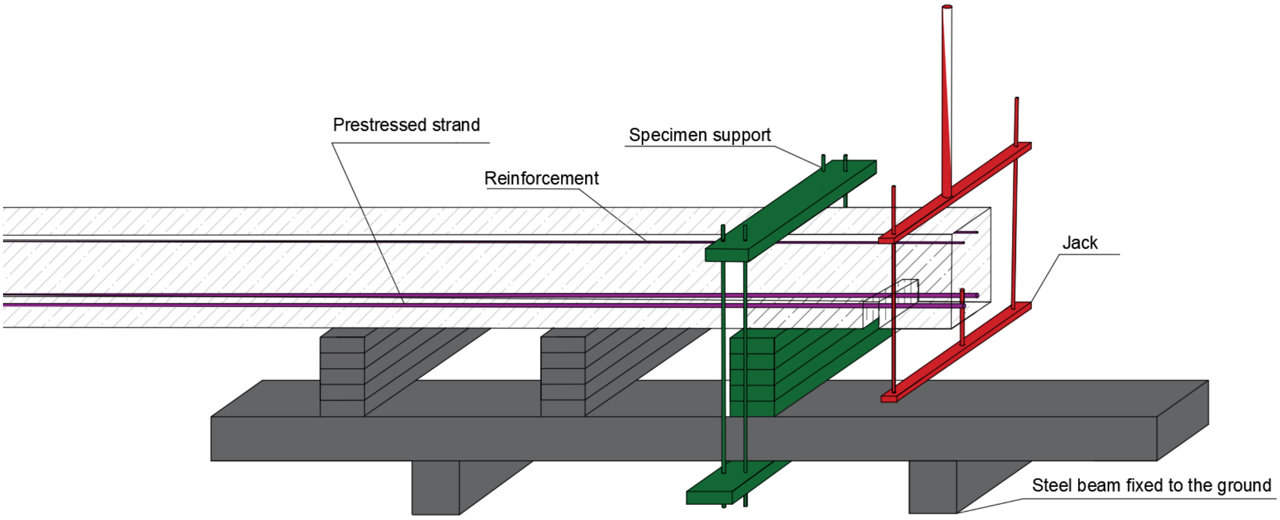

(b)

Figure 4-2 _ (a) The whole view of the corroded PC beam, (b) Graphical representation of PC beam under testing

The impact of corrosion on the strands of the beam is visible in Figure 4-3. This figure provides a visual representation that highlights the extent and nature of the corrosion occurring on the prestressing strands. Such observations are critical for understanding how corrosion compromises the structural integrity and overall performance of the beams. By examining the evidence presented in Figure 4-3, we can better appreciate the relationship between corrosion mechanisms and the degradation of bond properties in prestressed concrete.

Figure 4-3 _ presence of corrosion on the strands and surrounding concrete after splitting failure, Specimen BE1-test1, this part had been at the edge of the beam resulting more exposure to corrosion

4.1.1 Material Properties and Geometry of Specimens

The beam was strategically divided into three distinct beam-end specimens, with each segment subjected to individual testing and evaluation. The objective was to assess the bond behaviour and load-bearing capacity of each segment in isolation. As previously noted, three separate tests were conducted, each corresponding to one of the three segments. The first test was performed on the beam-end segment designated as BE1, which represents the edge portion of the entire beam. After the completion of this initial test, the tested segment was removed from the beam, and the subsequent segment was prepared for evaluation. This second segment, referred to as BE2, was then tested under similar conditions. Following this, the second segment was excised, and the final segment, named BE3, was prepared and subjected to testing. Through this systematic approach, each beam-end specimen—BE1, BE2, and BE3—was individually analysed, enabling a detailed assessment of each part along the beam length, Figure 4-4.

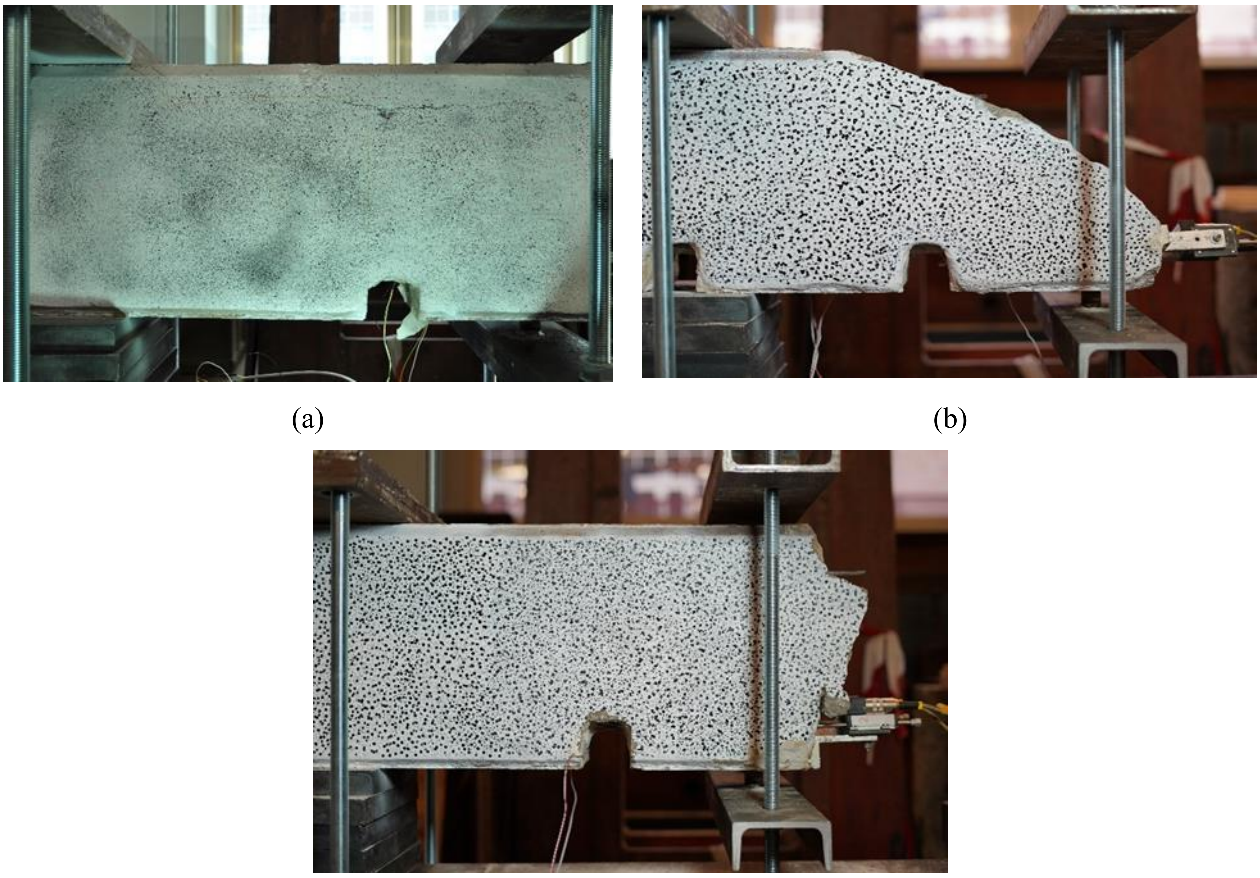

(a) (b)

(c)

Figure 4-4 _ Three beam-end specimen, (a) Specimen BE1 _ Test1, (b) Specimen BE2 _ Test2, (c) Specimen BE3 _ Test3

The geometrical specifications of the beam-end specimens are detailed in Table 4-1, while a more accurate representation can be found in Figure 4-5. The prestressed strands employed, consisted of two seven-wire strands, each with an equivalent diameter of 12.7 mm, strategically positioned at the bottom of the beams' cross-section and two bars located at the top part of the beam with the diameters equal to 5 mm.

Geometry of PC beam-end specimen	Test 1 (BE1)	Test 2 (BE2)	Test 3 (BE3)
Name of parameters	mm	mm	mm
Beam height	300	300	300
Beam length from the support to the end	520	480	520
Support length	140	140	140
Bond length	230	230	230

Strand diameter	12.7	12.7	12.7
Concrete Cover for the bottom strands	50	50	50
Beam width	150	150	150
Top reinforcement diameter	5	5	5
Concrete Cover for the top reinforcements	40	40	40

Table 4-1 _ Geometry of PC beam-end specimens

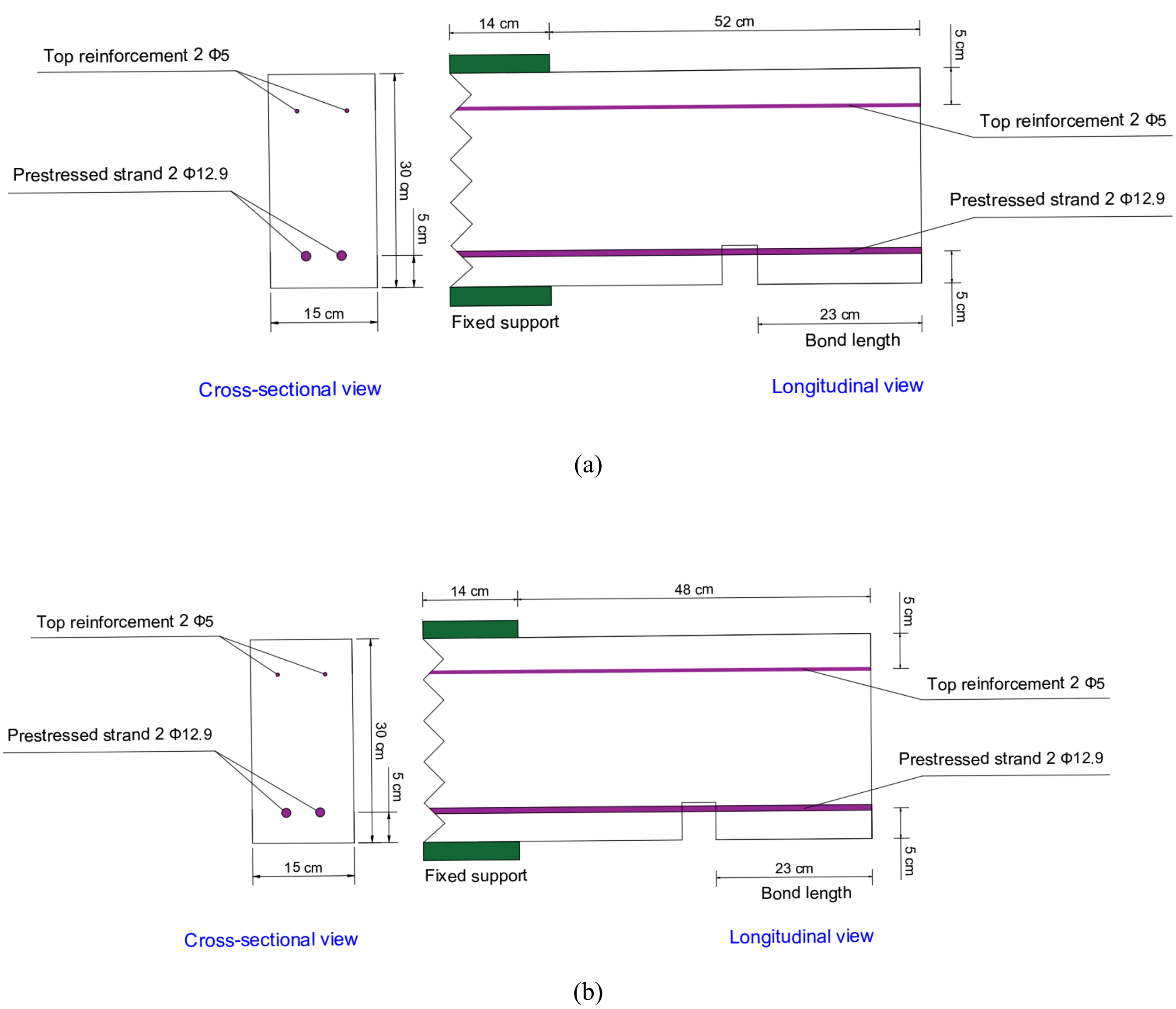

(a)

(b)

Figure 4-5 _ (a) Geometric presentation of specimens regarding tests 1 and 3 (BE1 and BE 3), (b) Geometric presentation of specimens regarding test 2 (BE 2)

In terms of specimen geometry, all three beam-end specimens have similar geometry except in terms of total length. For the specimens evaluated in tests 1 and 3 (BE1 and BE3), a beam-end specimen length of 52 cm was considered, whereas the beam-end specimen length evaluated in test 2 (BE2) was notably shorter, setting as 48 cm. The material properties of the specimens are described in Table 4-2.

Concrete			
f_c	f_{ct}	E_c	
[MPa]	[MPa]	[GPa]	
45.4	3.36	35.6	
Prestressing strands			
E_p	f_{pu}	ε_{pu}	Diameter
[GPa]	[MPa]	[%]	[mm]
195	1901.75	5	12.7
Rebars			
E_s	f_y	ε_{su}	Diameter
[GPa]	[MPa]	[%]	[mm]
195	435	18	5

Table 4-2 _ Mechanical properties of beam-end specimen

The initial prestressing strength $\sigma'_{p,0}$ of 1095 MPa was considered to the PC beam. Importantly, the actual prestress $\sigma_{p,res}$ within the strands was assessed just prior to conducting the second test. This determination was achieved using strain gauges during the experimental procedure, as well as back analyses facilitated by Non-Linear Finite Element Analysis software, ABAQUS, while the beams were in a state of relaxation. The estimated level of residual prestress in strands was equal to 55% of the initial prestress in strand, equal to 602 MPa, will be explained in detail in section 4.3.4.

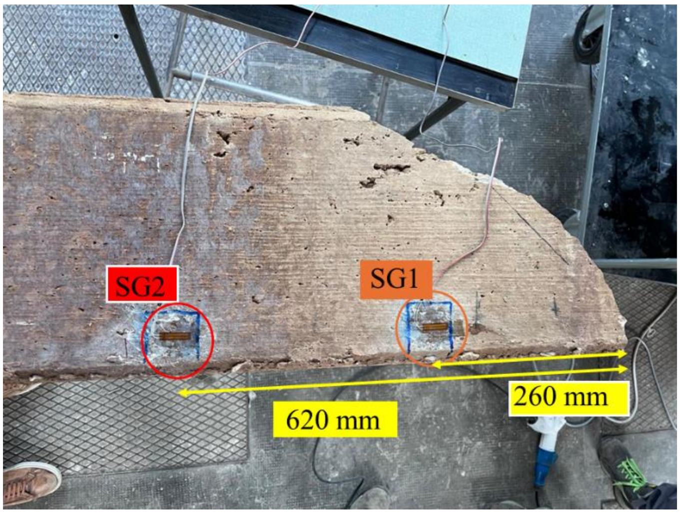

Figure 4-6 _ Strain gauges used to find the rsidual prestress level

It is noteworthy that the beam was designed without any form of transverse reinforcement. The placement of the reinforcement was strategically arranged, with the centroid distances from the exterior surface measuring 40 mm for the top reinforcement and 50 mm for the bottom reinforcement within the cross-section. In terms of the material properties, the mean compressive strength of the concrete was evaluated to be 45.4 MPa. This strength was determined through comprehensive testing, underscoring the structural integrity of the specimens in the context of long-term exposure and service conditions. This detailed analysis contributes to a deeper understanding of the behaviour of prestressed concrete beams subjected to corrosion and emphasizes the significance of bond properties in the durability assessment of such structural elements.

4.1.2 Test Setup

The beam-end specimens are fixed by two supports, positioned above and below the beam, effectively fixing the specimen from the top and bottom, while the right and left sides remain free. This configuration simulates a cantilever beam, as it is fixed on one side only, with the other side unsupported, Figure 4-7 and Figure 4-2b.

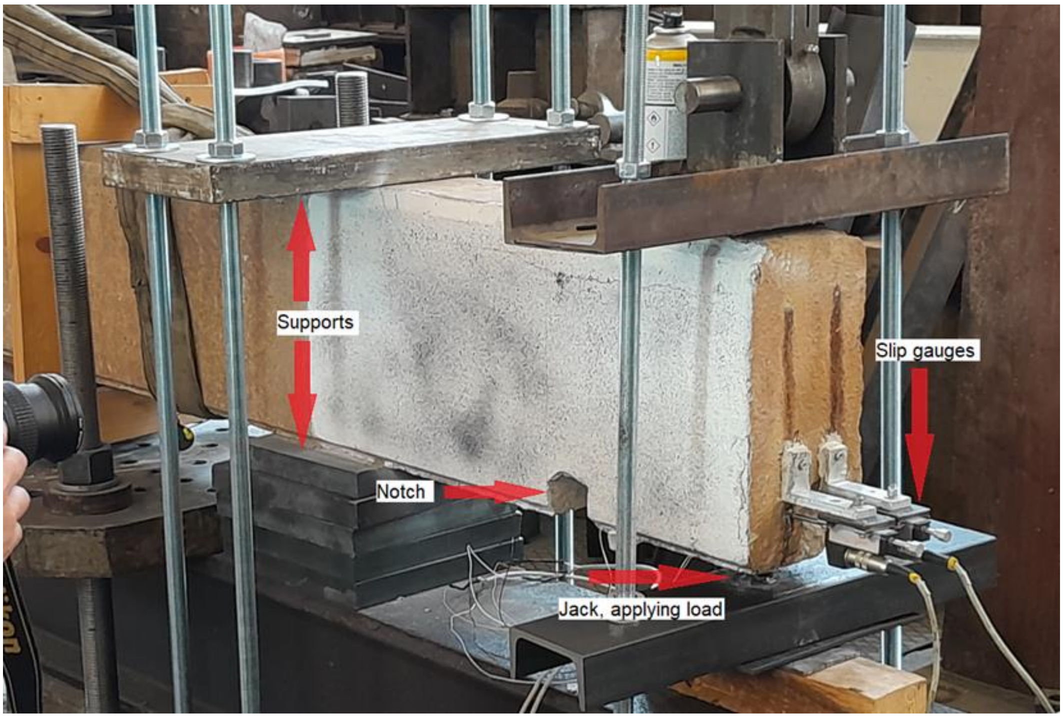

Figure 4-7 _ Fixed supports on only one side of the beam-end specimen _ Slip Gauges located on the end of beam and connected to the end of strands _ Jack which applies load in the hole _ Notch to manage bond length _ All three specimens have same test set up

A notch has been created in the lower part of the beam, defining a bond length of 23 cm. This bond length corresponds to the portion of the strands embedded in concrete, extending from the notch to the free end of the beam, while the remaining portion of the strands has been inactivated from participating in bond process, Figure 4-7 and Figure 4-8.

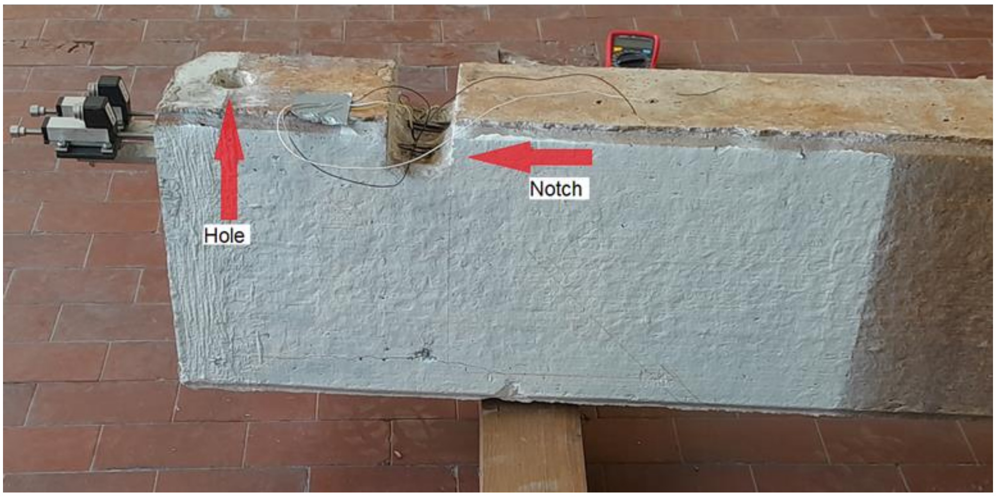

Figure 4-8 _ Notch at the bottom of beam _ Hole created to apply load

Moreover, a hole has been drilled at the free end of the beam, extending from the bottom upwards to slightly above the level of the strands, Figure 4-8. This hole is positioned between the strands to facilitate the application of the load, Figure 4-9. The load is applied using a hydraulic jack inserted into the hole, with the force directed upwards, pulling the free end of the specimen upward, Figure 4-7 and Figure 4-10. This hole is strategically created to prevent any potential compression stress that might be exerted on the strands by the surrounding concrete due to the applied load. By eliminating this compression stress, the loading phase does not affect the bond between the strands and the surrounding concrete, ensuring an accurate measurement of the bond strength.

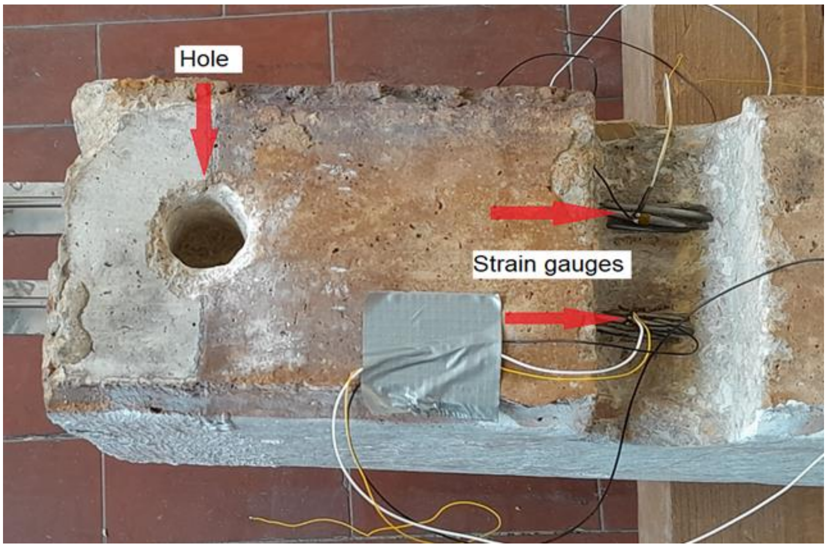

Figure 4-9 _ Hole created to apply load _ Strain gauges to measure strain in strands

If compression stress were applied at the interface between the strands and concrete, the bond strength might be overestimated. The load is gradually applied to the specimen in a displacement-controlled manner, avoiding any shock across the specimen. The graphical representation test setup of the specimens under testing is provided in Figure 4-10.

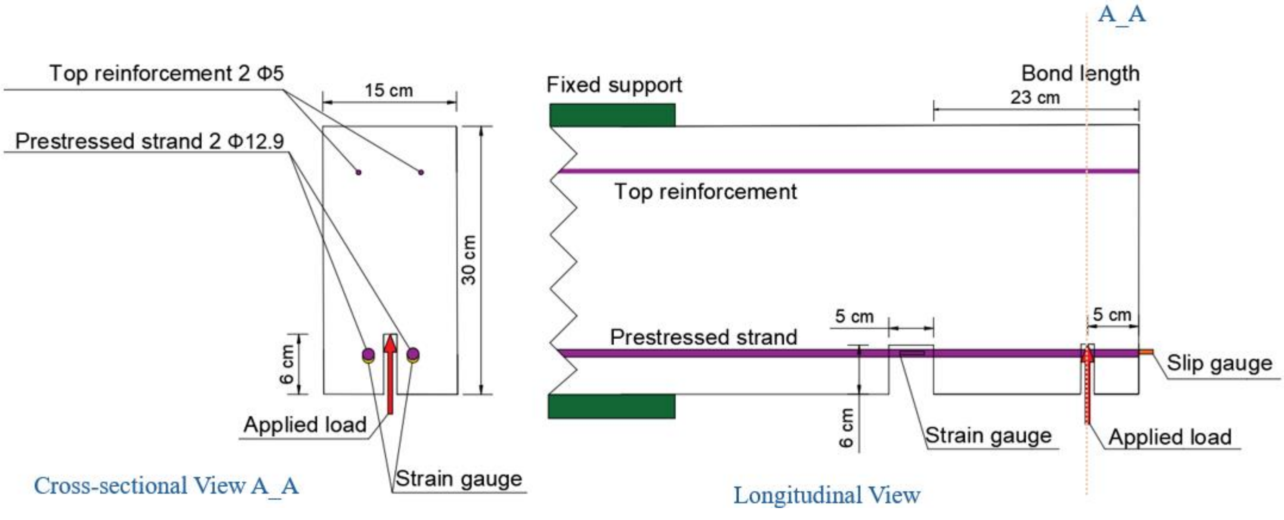

(a)

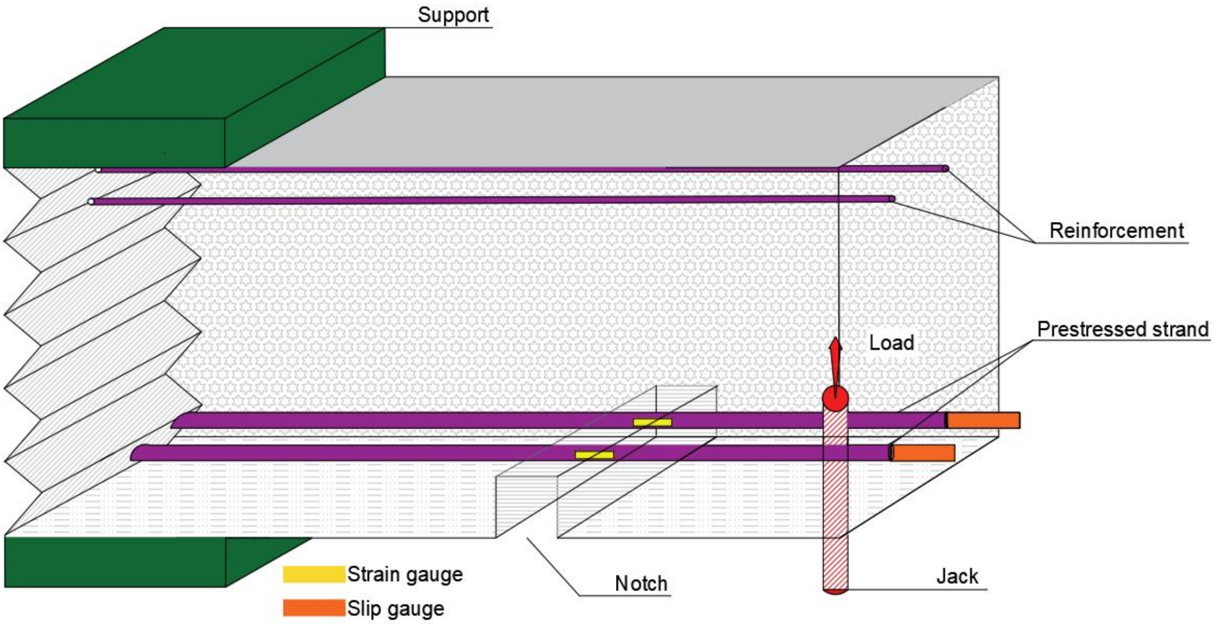

(b)

Figure 4-10 _ (a) 2D graphical representation of specimens and test setup, (b) 3D graphical representation of specimens and test setup

Moreover, during the tests, strain gauges were employed to monitor the strain within the strands, providing precise measurements of the internal deformation, Figure 4-9 and Figure 4-10. Simultaneously, slip gauges were used to record the relative displacement between the strands and the surrounding concrete at the end of the beam, Figure 4-7 and Figure 4-11. This dual monitoring approach allowed for a comprehensive analysis of the interaction between the strands and concrete, capturing both the internal strain and the external relative movement, which are critical for understanding the bond behaviour under load.

Figure 4-11 _ Gauges to record the relative slip of strand at the end of beam

4.1.3 Experimental Results

In this section, the experimental results obtained from three tests conducted in the laboratory to evaluate the structural behaviour, especially bond between strands and concrete, of the naturally corroded PC beam-end specimens under loading will be presented. The experimental setup was meticulously designed to replicate realistic loading scenarios, with careful consideration given to the placement of notches, supports, and loading points to accurately capture the specimens' response. During the tests, key parameters such as load, displacement, slip in strands and strain were continuously monitored using precise instrumentation to ensure the reliability of the data collected. The results provide valuable insights into the bond stress-slip relationship between strands and surrounding concrete and the failure mechanisms, highlighting the influence of natural corrosion on the PC beam. The following section will detail the findings from each test, providing a comprehensive analysis of the observed structural behaviour. As previously mentioned, a displacement-controlled test was conducted on the beam-end specimens, Figure 4-2b, which were configured to resemble cantilever beams. The load was applied gradually in an upward direction, and the load versus time relationship is illustrated in Figure 4-12. It is observed that in test 2 there is a residual capacity while the other two tests experienced approximately brittle failure.

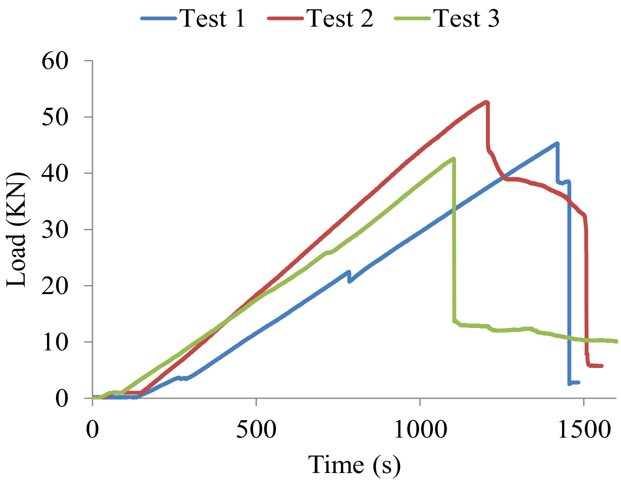

Figure 4-12 _ Applied vertical load vs Time

Strain gauges were also employed during the tests to measure the strains variation in the strands, with the gauges attached to the strands near the notch Figure 4-9. The resulting load versus strain data is presented in Figure 4-13.

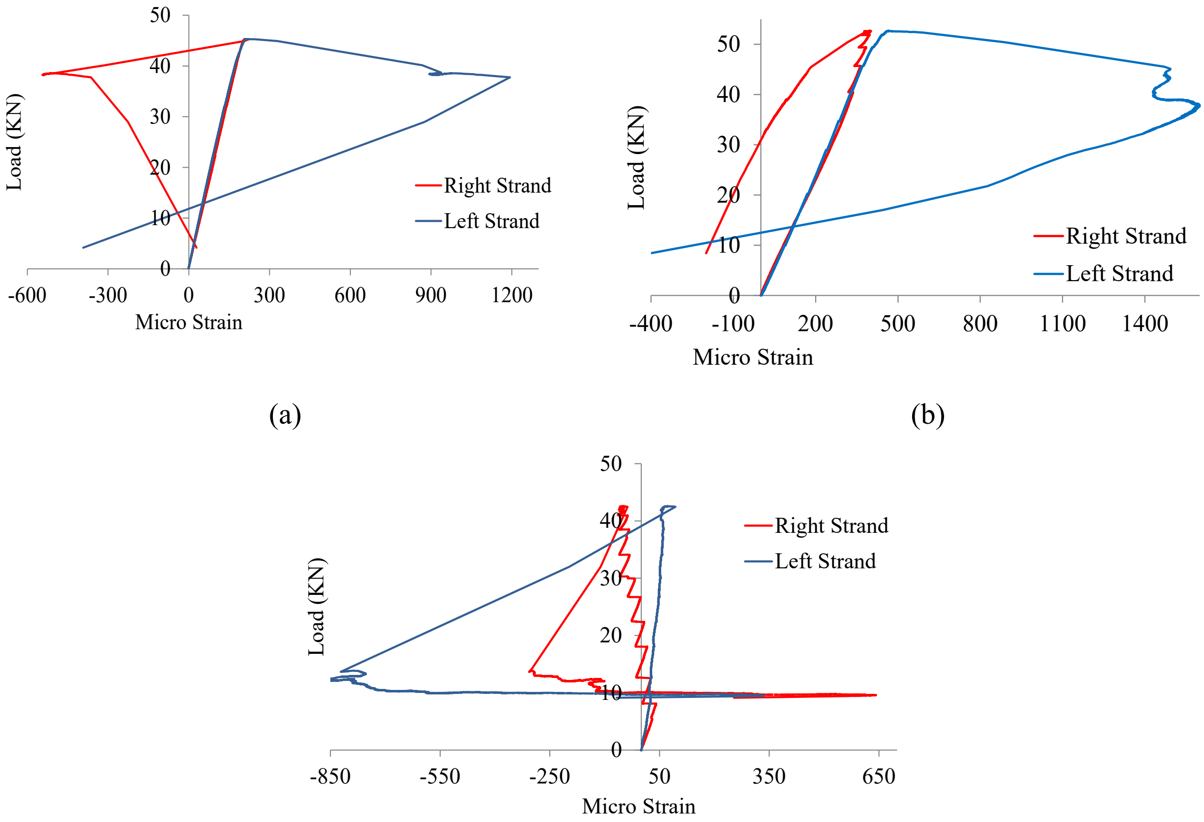

(a)

(b)

(c)

Figure 4-13 : (a) Test1, (b) Test 2, (c) Test3 _ Applied vertical load vs recorded micro strain

It could be observed that in test 1and 2, when the load increases the strands experienced elongation until beam failure and bond loss and after appearing the failure, the right strand tends to back to the previous situation before pre-tensioning of the strands (the negative parts do not represent the compression in the strands while they represent less elongation compared to after pre-tensioning). Therefore, the left strands sustain more elongation in the residual part to offset the lack of right strand.

In test3, the specimen experienced a bit rotation in the horizontal direction in the first steps which leads to negative strain in the right strands and after bond loss, the right strands tend to come back to the relaxation situation which was before pre-tensioning. While the left strand, lost its bond after sustaining the load and elongation and then follow coming back pattern to the situation with no stress.

Moreover, two slip gauges were used to measure the relative slip between the strands and the concrete at the end of the specimen Figure 4-10 and Figure 4-11. The load versus slip results are depicted Figure 4-14.

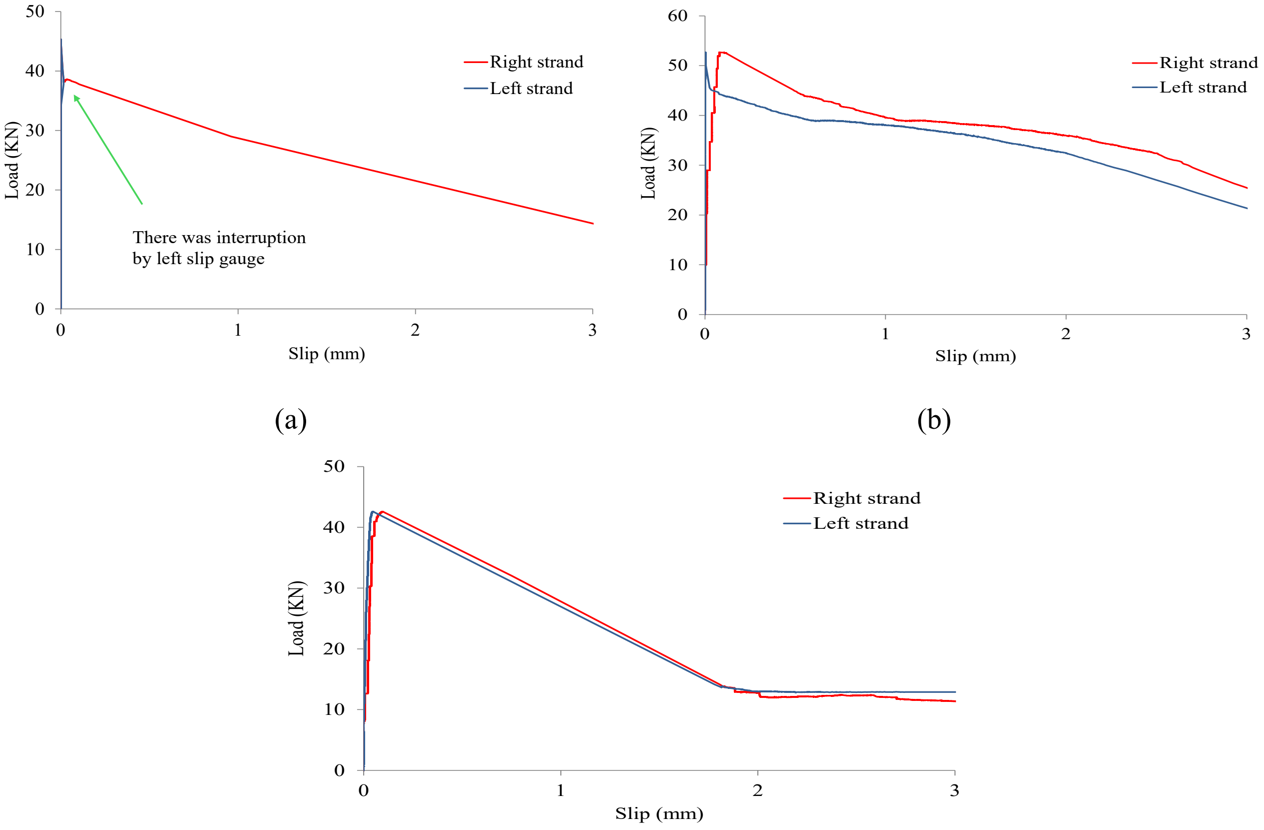

(a) (b)

(c)

Figure 4-14 : (a) Test1 (left gauge experienced detachment), (b) Test 2, (c) Test3

Using Equation 4-1,the uniform bond for each strand was calculated, and the bond-slip relationship is illustrated in Figure 4-15 and Figure 4-16. The slip can be seen before reaching the maximum capacity of beam and in the residual part.

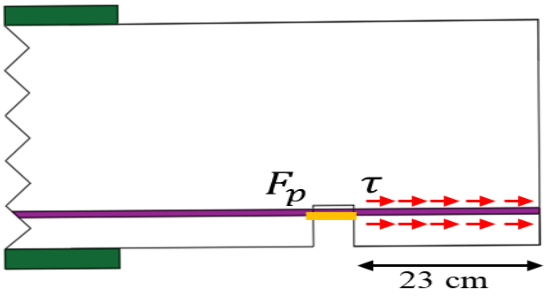

Figure 4-15 _ The bond is calculated based on F_p obtained based on strain gauges divided by strand equivalent perimeter and bond length

$$\sigma = E * \varepsilon$$ Equation 4-1

$$F_p = \sigma * A$$

$$\tau = F_p / A'$$

Where:

σ is tensile stress in each strand

E is 195000 MPa

ε is strain in each strand measured by strain gauges

F_p tensile force in each strand based on measured strain

A is strand area

A’ is $\pi * bond\ length * strand\ diameter$

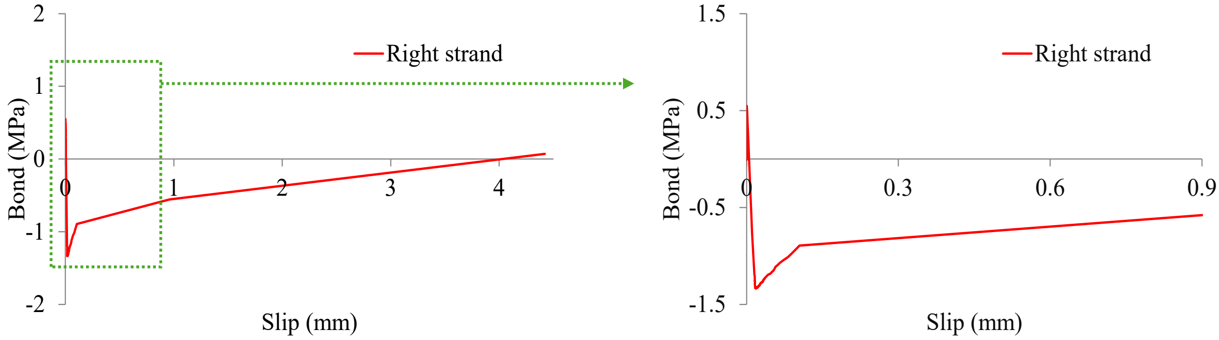

(a)

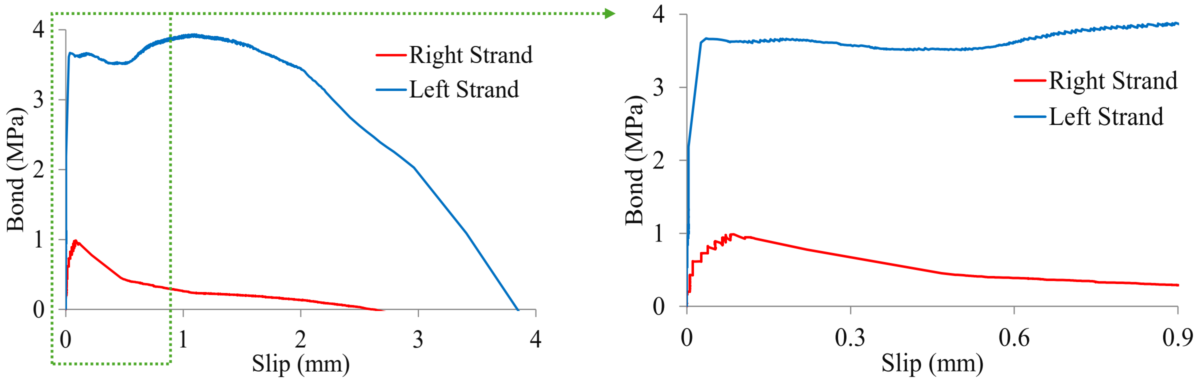

(b)

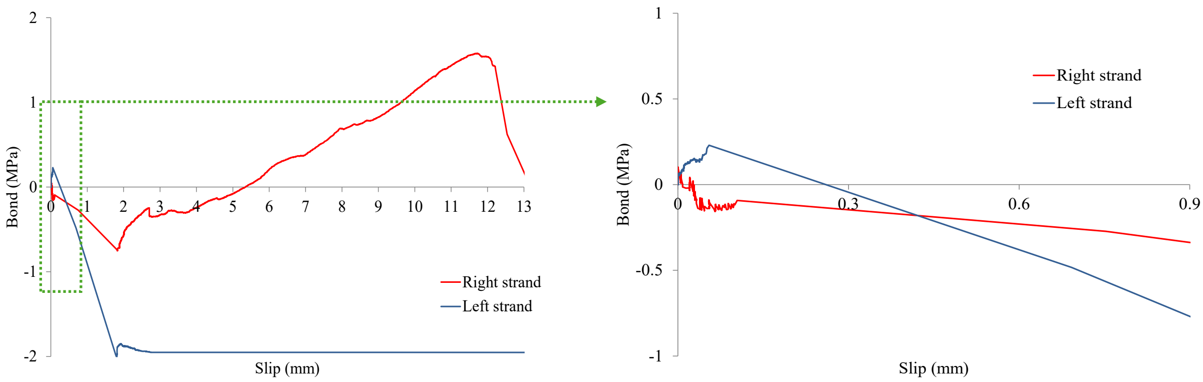

(c)

Figure 4-16 _ (a) Test1, the transducer to measure the relative slip of left strand showed interruption, (b) Test 2, (c) Test3 _ The zoomed view of the graph shown in the right

The bond stress-slip relationship which calculated based on the strains that was recorded by strain gauges during the experimental test could be considered as an average bond-slip in our region of interest because the strain gauges was in the notch, not monitoring complete bond length in detail and also the slip gauges recorded the slip only at the end of the specimen. It should be mentioned that the bond stress- slip relationship for the left strand in the test 1 could not be presented due to interruption in slip gauges.

4.2 Digital Image Correlation (DIC)

Strain and displacement are essential factors in the fields of engineering, as they provide critical insights into material behaviour and structural integrity. Accurately evaluating these parameters, whether in a laboratory setting or in the field, poses a significant challenge due to the need to balance accuracy, simplicity, and cost. Traditional measurement methods often involve compromises among these factors, leading to a demand for innovative techniques that can provide comprehensive and precise data. Digital Image Correlation (DIC) has appeared as a promising method for addressing this need, particularly in the study of crack propagation and material deformation. DIC offers a cost-effective, straightforward, and highly precise solution, making it suitable for both laboratory and real-world applications. Digital Image Correlation is a cutting-edge, non-contact optical method used for quantifying strain and displacement. It is recognized for its ease of use and cheapness compared to more conventional methods such as speckle interferometry. Moreover, DIC offers greater precision and objectivity than manual measurement approaches, significantly expanding its potential applications across various disciplines(McCormick & Lord, 2010). The development of DIC has been driven due to the restriction of traditional measurement instruments, such as Linear Variable Differential Transformers (LVDTs) and strain gauges, which require physical contact with the specimen. These contact-based methods are often restricted in their ability to provide comprehensive data on displacement and strain fields. In contrast, DIC enables full-field measurement without direct contact, facilitating the obtaining of more detailed information at a lower experimental cost. Since its initial implementation in the 1980s, DIC has developed significantly, including reductions in computer demand and improvements in precision. The technique involves capturing sequential images of a specimen as it undergoes deformation. By employing an image processing algorithm, DIC calculates displacement and strain fields on the specimen's surface by numerically comparing the grey-level intensities of undeformed and deformed images (de Assis & Evangelista Junior, 2017). The DIC method begins by capturing a reference image of the specimen prior to loading, continuing by a series of images captured during deformation. As the material deforms, the speckle pattern on its surface changes, and these changes are used to calculate displacement fields. The utilization of a digital camera to capture these images distinguishes DIC from other experimental methods used for assessing strain deformation. By analyzing these deformed images, DIC provides a comprehensive map of the strain distribution across the specimen's surface. This is satisfied by applying mathematical derivatives to the displacement field, which can be reached using various techniques, such as dots, grids, or lines on the sample. The accuracy and quality of DIC analyses are largely based on the resolution of the camera and the drown speckles on the sample. For effective DIC implementation, the surface of the specimen must be prepared with a random speckle pattern, which provides unique points for correlation. By comparing the speckle map before and after deformation, DIC can determine strain by tracking the movement of specific points within the grid formed by image subsets. The positions of these points, recorded before and after deformation, are critical for the correlation process and the subsequent calculation of strain. Several software solutions are available to support DIC analysis, including the open-source Ncorr, which is built on the MATLAB platform. Ncorr provides an accessible and cost-effective tool for engineers globally, enabling precise measurement of displacement and strain in comparison to other methods. This software is versatile and can be applied to any material capable of retaining a fine speckle pattern on its surface. Recent explorations have extended its application to composite materials, showcasing its potential for further innovation. Thus, DIC, particularly when combined with accessible tools like Ncorr, represents a powerful approach for analyzing material behaviour in both academic research and practical engineering settings (Akademia Baru et al., 2016). When images are captured by digital cameras, they are imported into the Ncorr software, beginning with a photo taken before any loading as the reference image. Subsequent images taken during the loading phase are also input into the software, which then detects the displacement of each speckle pattern. The reference image is divided into smaller sections, known as subsets. For 2D Digital Image Correlation (DIC) analysis, it is assumed that the deformation within each subset is homogeneous. The software tracks these deformed subsets in the current images to determine their new positions. The transformation of coordinates from the reference state to the deformed state is constrained to a linear, first-order transformation.

$$X_2 = X_1 + u_{1,2} + \left(\frac{\partial u}{\partial x_{1,2}}\right)(X_{1i} - X_{1c}) + \left(\frac{\partial u}{\partial y_{1,2}}\right)(Y_{1i} - Y_{1c})$$ Equation 4-2

$$Y_2 = Y_1 + v_{1,2} + \left(\frac{\partial v}{\partial x_{1,2}}\right)(X_{1i} - X_{1c}) + \left(\frac{\partial v}{\partial y_{1,2}}\right)(Y_{1i} - Y_{1c})$$ Equation 4-3

$$P = \left\{ u \quad v \quad \frac{\partial u}{\partial x} \quad \frac{\partial u}{\partial y} \quad \frac{\partial v}{\partial x} \quad \frac{\partial v}{\partial y} \right\}$$ Equation 4-4

Where:

X_2 and Y_2 are the coordinates of subset point after loading

X_{1i} and Y_{1i} are the coordinates of an initial reference subset point

X_{1c} and Y_{1c} are the coordinates of the center of the initial reference subset

P is a generalized deformation vector

The subscript “1,2” used to signify that the transformation is from reference condition to the after loading condition.

Figure 1 shows the reference subset before loading start, and the target subset after deformation of specimen.

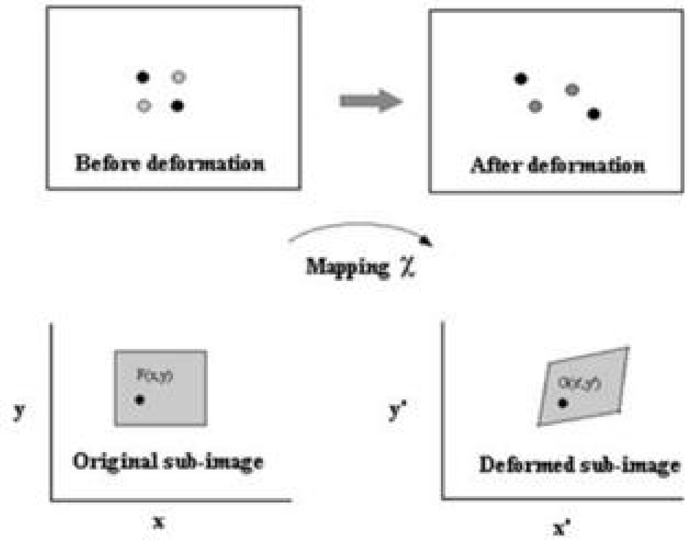

Figure 4-17 _ Digital image correlation deformation working principle (Akademia Baru et al., 2016)

Determining strain fields is more challenging than calculating displacement fields due to the requirement for differentiation, which is highly sensitive to noise. Any noise present in the displacement data can significantly amplify errors in the resulting strain measurements. To address this issue, Ncorr employs the Green-Lagrangian strain formulation, which provides a more accurate representation of strain, particularly in the presence of nonlinear deformations.

$$E_{xx} = 0.5(\frac{2\partial_u}{\partial_x} + \left(\frac{\partial_u}{\partial_x}\right)^2 + \left(\frac{\partial_v}{\partial_x}\right)^2) \qquad \text{Equation 4-5}$$

$$E_{yy} = 0.5(\frac{2\partial_v}{\partial_y} + \left(\frac{\partial_u}{\partial_y}\right)^2 + \left(\frac{\partial_v}{\partial_y}\right)^2) \qquad \text{Equation 4-6}$$

$$E_{xy} = 0.5(\frac{\partial_u}{\partial_y} + \frac{\partial_v}{\partial_x} + \frac{\partial_u\partial_u}{\partial_x\partial_y} + \frac{\partial_v\partial_v}{\partial_x\partial_y}) \qquad \text{Equation 4-7}$$

Numerous studies have explored the use of the Digital Image Correlation (DIC) technique and the Ncorr platform for measuring surface displacement and strain. These investigations have utilized various cameras, speckle patterns, and experimental setups. The findings consistently demonstrate that DIC, particularly when implemented through Ncorr, is a reliable and effective method for such measurements.

4.2.1 Digital Image Correlation (DIC) Test Setup

All three specimens in the study were monitored using Digital Image Correlation (DIC) to assess their surface displacement. For Test 1, a single digital camera was employed, while Tests 2 and 3 utilized two digital cameras to capture a more accurate and comprehensive view. The cameras were positioned directly in front of the specimen surface, with their elevation precisely aligned with the centerline of the beam to ensure consistency in measurements. Proper camera placement was critical to minimize potential errors, so the cameras were carefully set at an optimal distance from the samples. Furthermore, an appropriate lighting setup was used to provide uniform illumination, which is crucial for obtaining clear and consistent images. The cameras were programmed to capture images at regular intervals of approximately every 10 seconds, as illustrated in Figure 4-18.

(a)

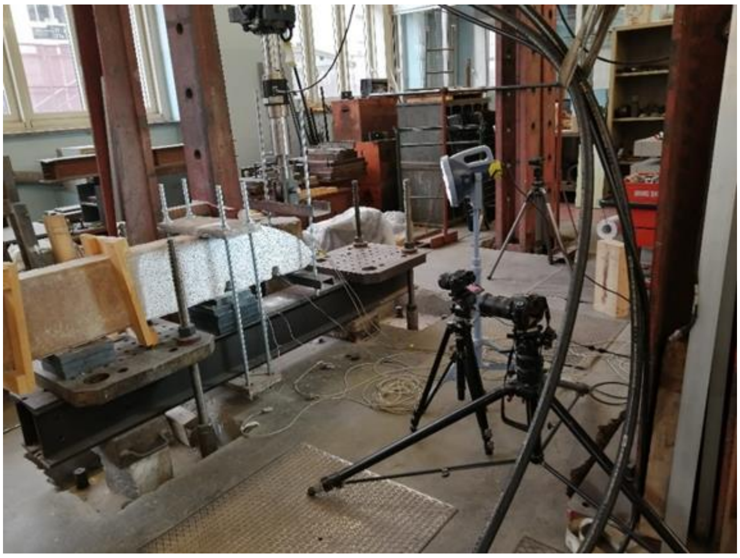

(b)

(c)

Figure 4-18 _ Position of cameras and lighting in DIC. _ (a) test 1, (b) test 2, (c) test 3

To enhance the image quality and accuracy of the DIC analysis, different methods were used to create speckle patterns on the specimen surfaces. For specimen BE1, a spray technique was employed to apply a speckle pattern onto the beam surface. In contrast, specimens BE2 and BE3 had speckle patterns manually drawn onto their surfaces. The speckle patterns consisted of dots of three distinct sizes, applied randomly and with high attention to detail to meet the requirements for accurate analysis. The variations in speckle size and patterning were carefully considered to optimize the image correlation process, as shown in Figure 4-19.

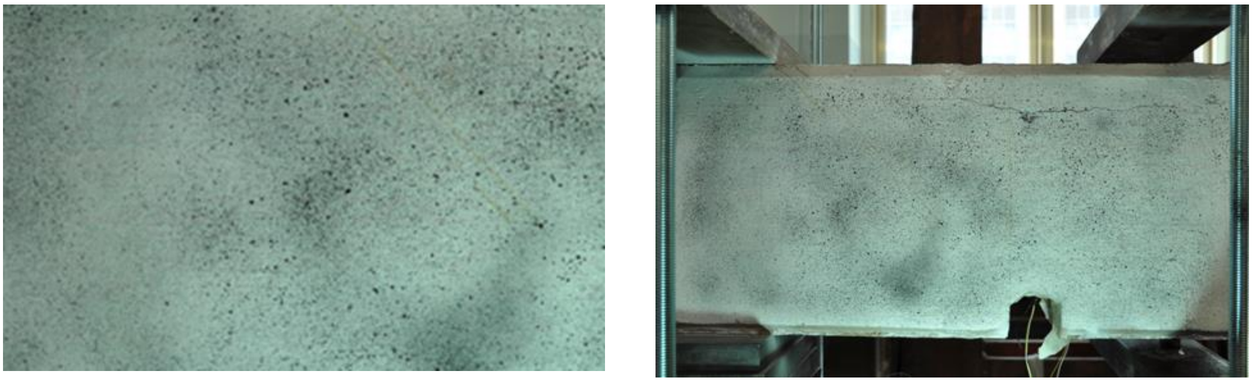

(a1) (a2)

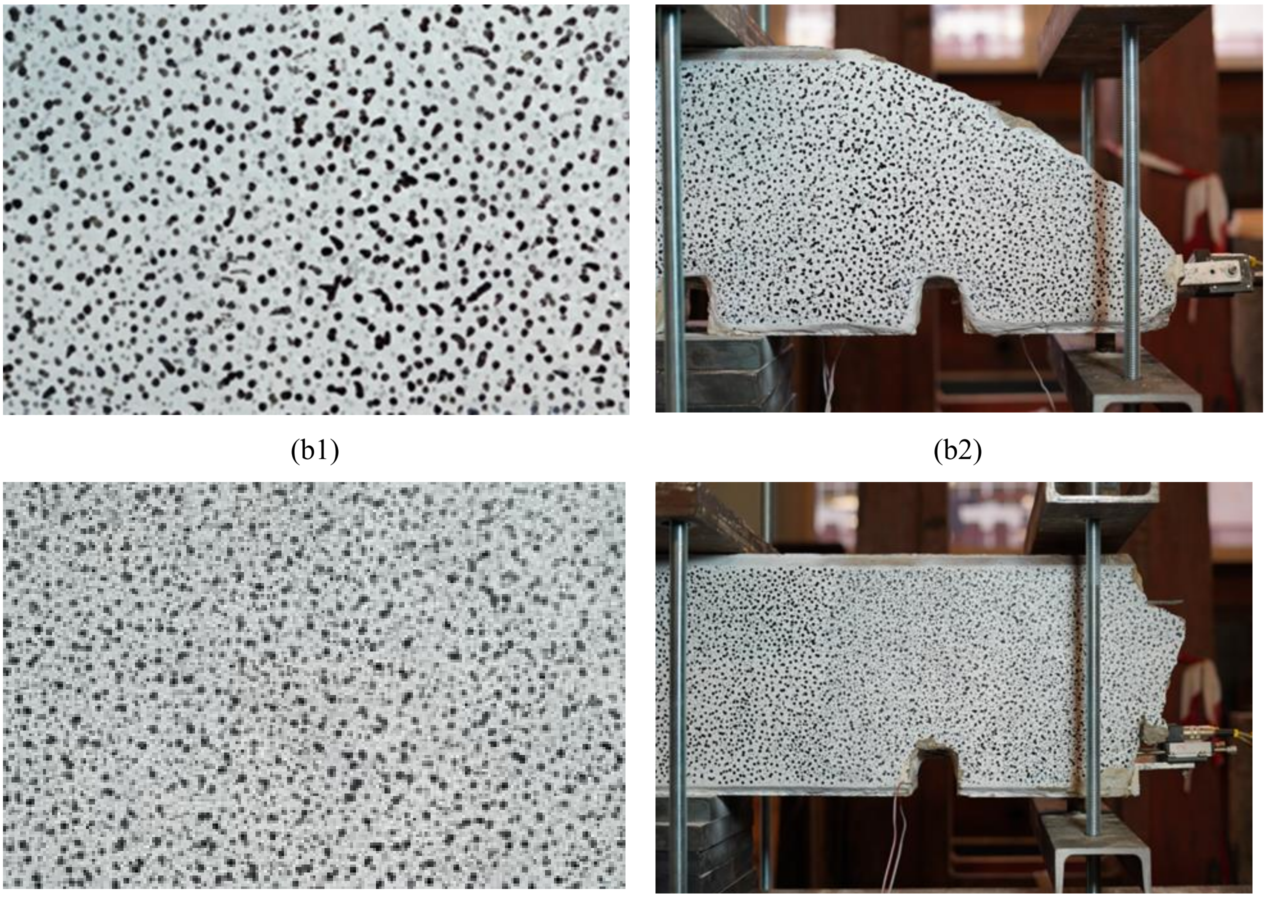

(b1) (b2)

(c1) (c2)

Figure 4-19 _ (a1) close view of speckle pattern specimen BE1, (a2) whole view of specimen BE1, (b1) close view of speckle pattern specimen BE2, (b2) whole view of specimen BE2, (c1) close view of speckle pattern specimen BE3, (c2) whole view of specimen BE3

After the images were collected, post-processing was conducted using the Ncorr software platform to analyze beam displacement and strain distribution. For each specimen, an image captured prior to loading; was considered as the reference image, and subsequent images taken during the loading and failure phases were analyzed to track changes. Ncorr allows for extensive parameter testing, including varying subset sizes, to refine the analysis and achieve the most accurate results. In terms of displacement analysis, the data obtained in pixel measurements were converted to real-world units (millimeters) to provide meaningful insights. For strain calculations, the Green-Lagrangian strain formulation was applied, providing a robust method for capturing both linear and nonlinear deformation effects. Figure 4-20 shows representative format examples from the Ncorr analyses results.

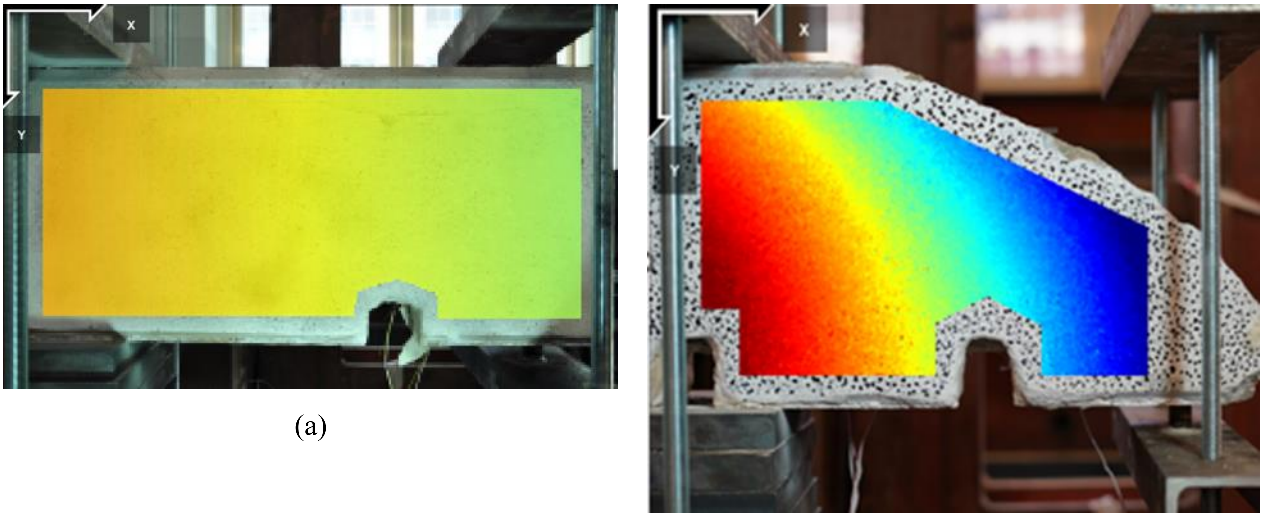

(a)

(b)

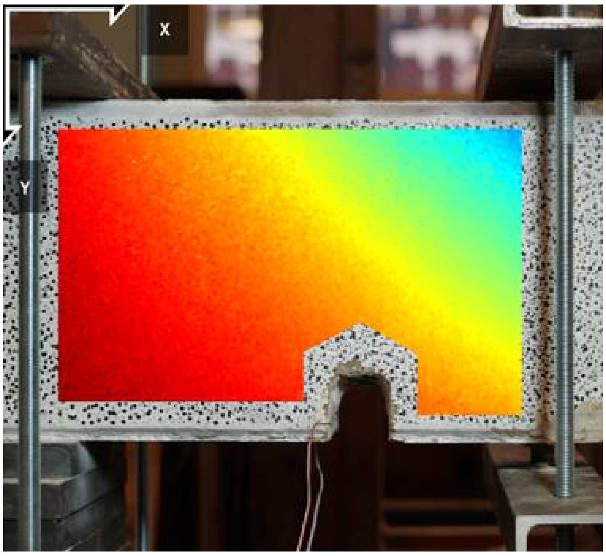

(c)

Figure 4-20 _ A representation sample to see the output format of Ncorr _ (a) test 1, (b) test 2, (c) test3

The use of multiple cameras, precise alignment, optimal lighting, and careful preparation of speckle patterns significantly enhanced the accuracy and reliability of the DIC measurements. Furthermore, the ability of Ncorr to adjust analysis parameters, such as subset size, enabled a fine-tuning of the data to improve the accuracy of the results. This comprehensive approach underscores the effectiveness of DIC and Ncorr in experimental mechanics, providing valuable data on material behaviour under load that can be used to inform engineering design and safety assessments. Another significant advantage of the Digital Image Correlation (DIC) technique is its ability to monitor crack patterns from their initiation through their progression. This is achievable because DIC captures images corresponding to each step of the loading process, allowing for detailed analysis of how cracks form and propagate over time.

4.2.2 Digital Image Correlation (DIC) Results

Digital Image Correlation (DIC) was employed to monitor the tests using digital cameras, which captured images of the specimen at 10-second intervals throughout the testing process. Following image acquisition, the digital images were processed using the Ncorr platform, operating within the MATLAB environment, to determine displacements in the regions of interest, as described in detail in Section 4.2. Furthermore, the analysis of these digital images allowed for the identification of the precise moment when the cracks appeared on the concrete surface. It is important to note that careful consideration must be given to the speckle pattern applied to the concrete surface, ensuring it is distributed randomly and features dots of varying sizes to facilitate accurate analysis. During the first test, the speckle pattern was applied using spray paint, which was insufficient and experienced noises for effective post-processing analysis. Furthermore, automatic zoom-in and zoom-out adjustments during capturing images affected the quality of the analysis. Consequently, the results of the second and third tests, which employed improved speckle patterns, will be discussed in this section. Therefore, for the load versus displacement curve, we have opted to present the data obtained from Test 2 and Test 3 which are calculated in the MATLAB environment, as shown in Figure 4-22.

By correlating the applied load with the recorded time and analyzing the Digital Image Correlation (DIC) images captured during the test, the load versus displacement of the beam in the vertical direction at the point of load application was determined. Due to the presence of steel plates that locked the beam at the support and the connection of the upper plate to the bottom plate and the underlying steel beam (fixed to the ground) through four steel bars, the support also experienced minor displacements. To address this issue and accurately determine the relative displacement of the loading point with respect to the supports ,Figure 4-21, DIC analysis was employed using simplified analytical Equation 4-8 and MATLAB codes. Initially, the DIC provided absolute deformation data, necessitating additional calculations in MATLAB to derive the relative deformation, which proved valuable for subsequent numerical analyses.

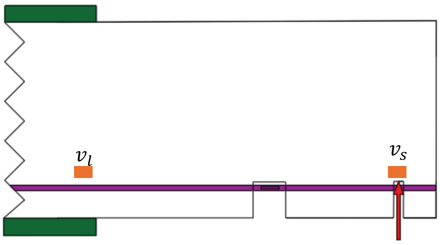

Figure 4-21 _ Positions of points used to extract relative vertical displacement using MATLAB

$v_r = v_l - v_s$ Equation 4-8

Where:

v_r is the relative vertical displacement at point of loading

v_l is absolute vertical displacement at point of loading

v_s is absolute vertical displacement at support

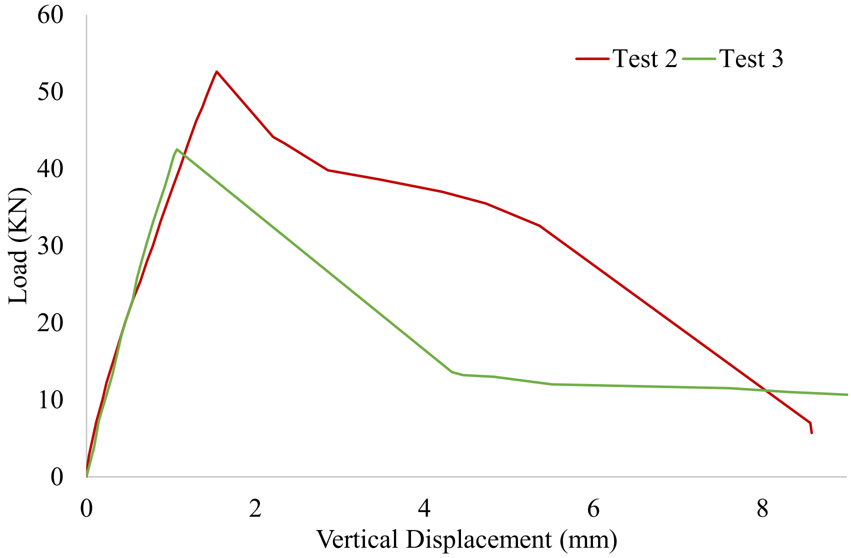

Figure 4-22 _ Load vs Vertical Displacement at where the load applied (vertical displacement obtained by DIC analyses)

Moreover, using DIC we recorded the moment at which the first shear crack reached the concrete surface, Figure 4-23. Also, there has been the possibility to observe and analyze the displacement pattern.

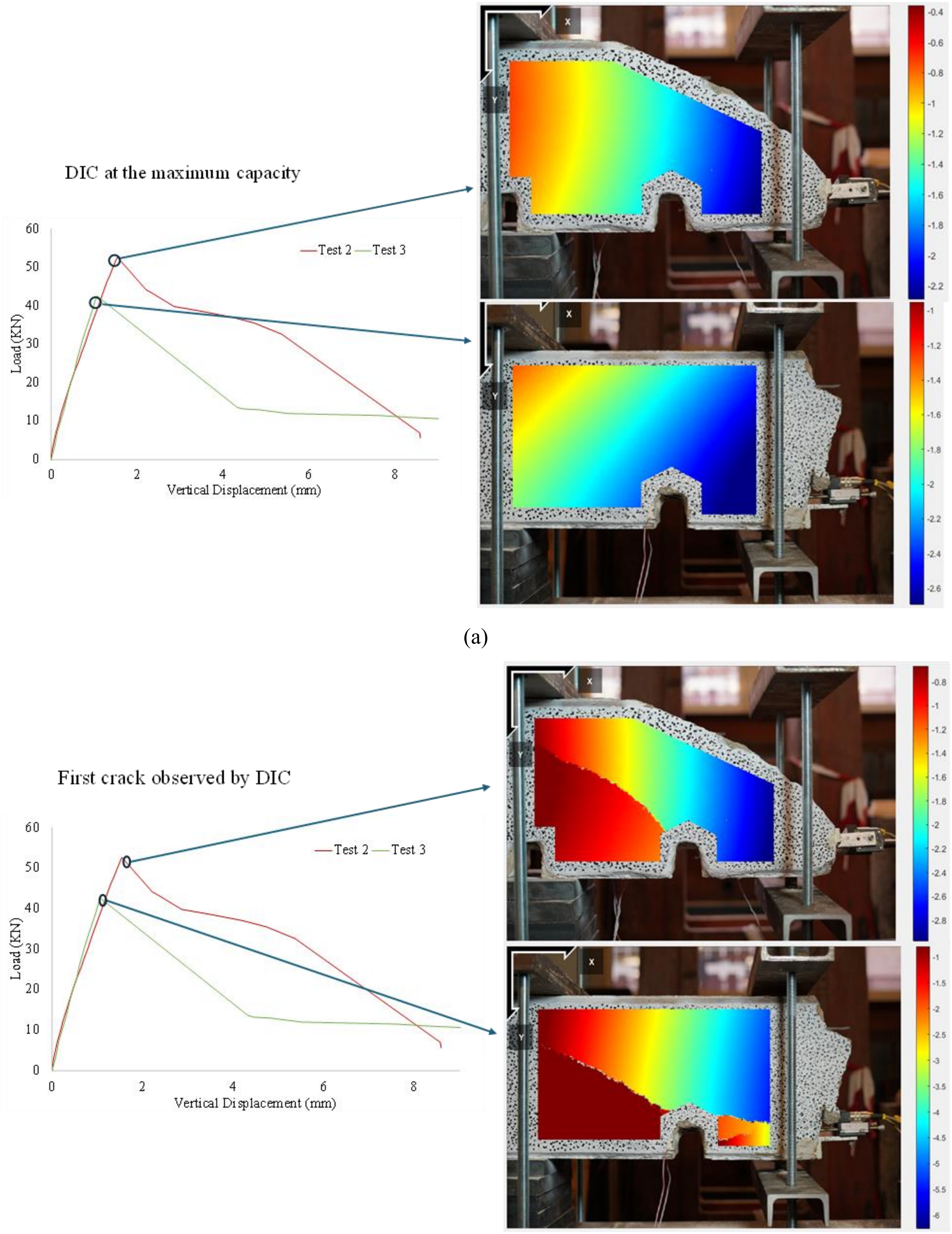

(a)

(b)

Figure 4-23 _ The vertical displacement shown in the DIC images are based on millimeters. (a) Vertical displacement distribution on the concrete surface when the specimen sustained the maximum load, (b) The first shear crack appeared immediately after the maximum load

Figure 4-23 demonstrated a sudden drop in the specimen's capacity following the appearance of the first crack in the concrete surface in Test 3. In contrast, the residual capacity in Test 2 decreased gradually after the first crack appearance in the concrete surface. Moreover, the Digital Image Correlation (DIC) analysis revealed the distribution of displacements across the specimen. All images were processed using the Ncorr platform, enabling the identification of displacement patterns in the specimen corresponding to each loading level. Therefore, the relative vertical displacement versus load regarding the part in which load applied has been drawn. Moreover, appearing the splitting cracks in the concrete surface has been tracked, Figure 4-24, which is useful to analyze the results obtained from the numerical approach.

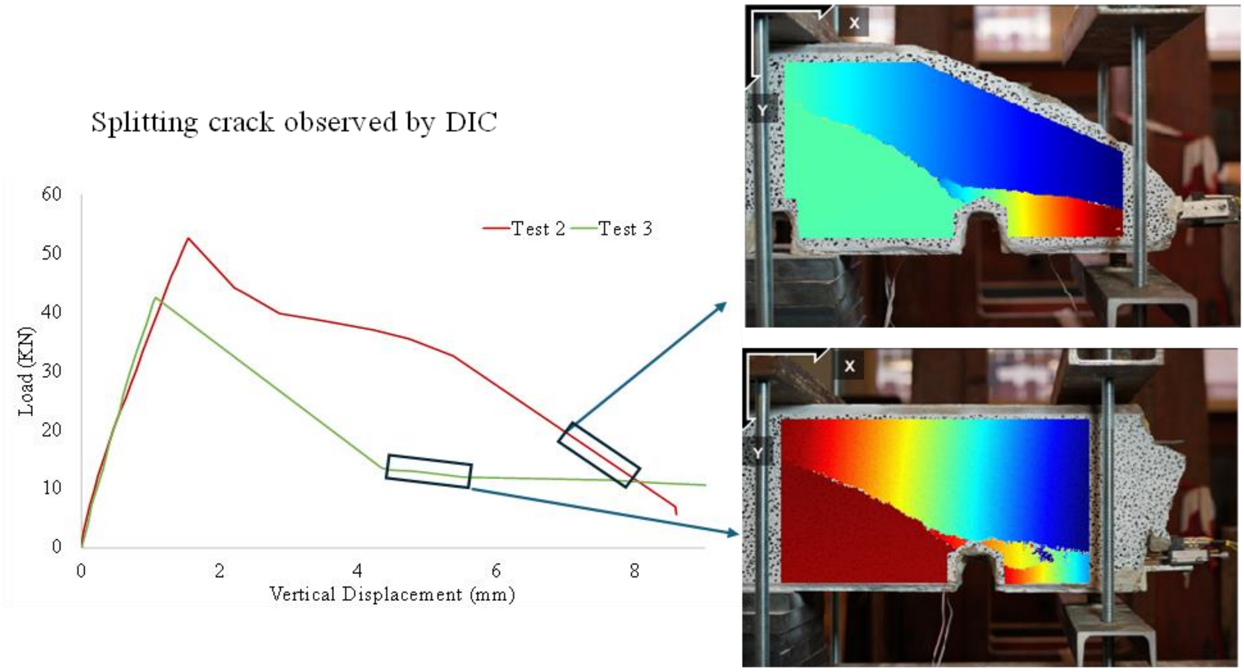

Figure 4-24 _ Appearance of splitting cracks in test 2 and test 3

Finally, the splitting failure has been observed for all three tests showing in Figure 4-25.

(a)

(b)

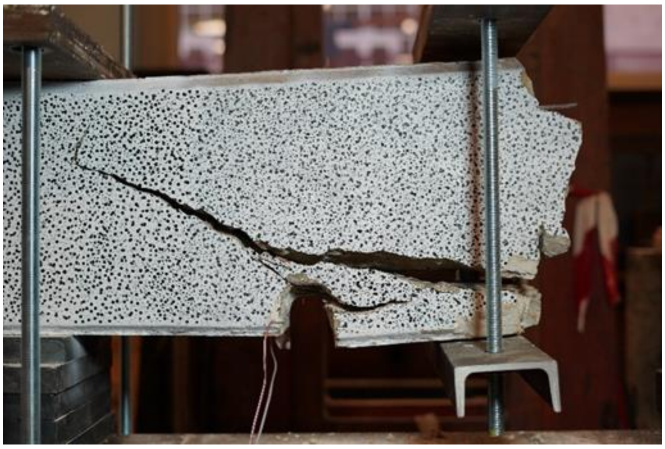

(c)

Figure 4-25 _ (a) Test 1, (b) Test 2, (c) Test 3 _ specimens after failure

4.3 Analytical Methods

4.3.1 Bond Stress vs Slip Relationship Based on Model Code 2010 (Model Code, 2010)

Considering our loading type and the failure mode as the splitting failure, the uncorroded reference value of $\tau_b$of the bond stress between concrete and the strands will be calculated by Equation 4-9 based on the model which proposed by Model Code 2010. And the parameters are described in the Table 4-3.

$\tau_b = \tau_{bmax}{}^{(\frac{s}{s1})^a}$ for $0 \leq s \leq s_1$

$\tau_b = \tau_{bmax}{}^{(\frac{s}{s1})^a}$ for $s_1 \leq s \leq s_2$ Equation 4-9

$\tau_b = \tau_{bmax} - (\tau_{bmax} - \tau_{bf})(s - s_2)/(s_3 - s_2)$ for $s_2 \leq s \leq s_3$

$\tau_b = \tau_{bf}$ for $s_3 < s$

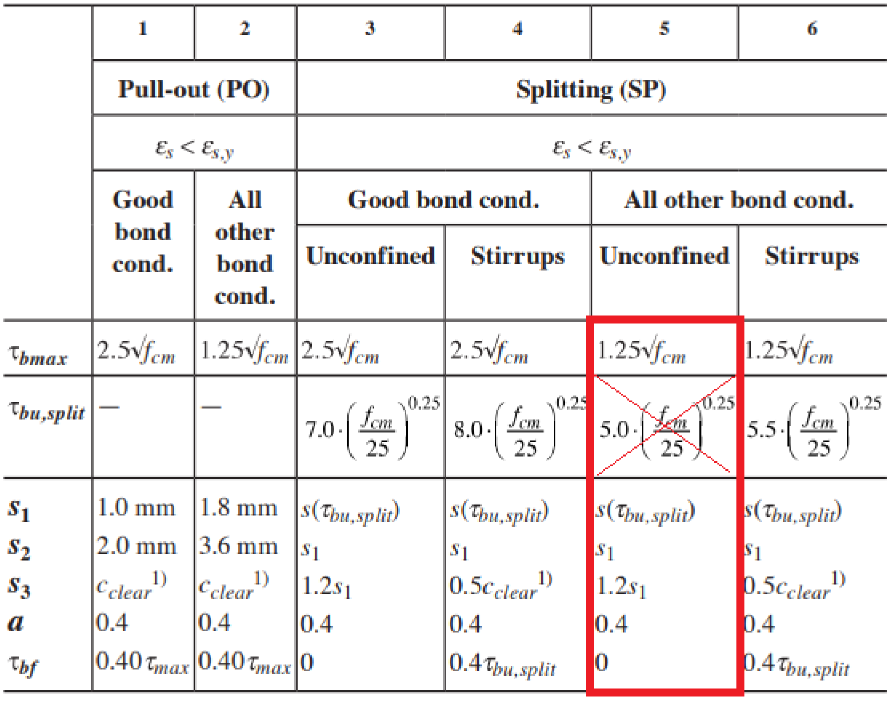

	1	2	3	4	5	6
	Pull-out (PO)		**Splitting (SP)**			
	$\varepsilon_s < \varepsilon_{s,y}$		$\varepsilon_s < \varepsilon_{s,y}$			
	Good bond cond.	**All other bond cond.**	**Good bond cond.**		**All other bond cond.**	
			Unconfined	**Stirrups**	**Unconfined**	**Stirrups**
τ_{bmax}	$2.5\sqrt{f_{cm}}$	$1.25\sqrt{f_{cm}}$	$2.5\sqrt{f_{cm}}$	$2.5\sqrt{f_{cm}}$	$1.25\sqrt{f_{cm}}$	$1.25\sqrt{f_{cm}}$
$\tau_{bu,split}$	—	—	$7.0\cdot\left(\frac{f_{cm}}{25}\right)^{0.25}$	$8.0\cdot\left(\frac{f_{cm}}{25}\right)^{0.25}$	$\cancel{5.0\cdot\left(\frac{f_{cm}}{25}\right)^{0.25}}$	$5.5\cdot\left(\frac{f_{cm}}{25}\right)^{0.25}$
s_1	1.0 mm	1.8 mm	$s(\tau_{bu,split})$	$s(\tau_{bu,split})$	$s(\tau_{bu,split})$	$s(\tau_{bu,split})$
s_2	2.0 mm	3.6 mm	s_1	s_1	s_1	s_1
s_3	c_{clear} 1)	c_{clear} 1)	$1.2s_1$	$0.5c_{clear}$ 1)	$1.2s_1$	$0.5c_{clear}$ 1)
a	0.4	0.4	0.4	0.4	0.4	0.4
τ_{bf}	$0.40\tau_{max}$	$0.40\tau_{max}$	0	$0.4\tau_{bu,split}$	0	$0.4\tau_{bu,split}$

Table 4-3 _ Splitting failure, other bond condition & unconfined is used (Model Code, 2010)

It should be noted that the condition "unconfined" in the category of "all other bond condition" is assumed in our calculation due to not having stirrups in our beam-end specimen. It could be seen that the τ_{bmax} and $\tau_{bu,split}$ are the function of mean cylinder compressive strength of the concrete which is 45.4 MPa in our case, and the generic slip should be evaluated according to $\tau_{bu,split}$. Therefore, as mentioned above, the parameters are considered based on the Table 4-3 except the parameter $\tau_{bu,split}$, because description of this parameter in the table is valid only if the strand diameter is equal to 25 mm while in our case, the strand diameter is equal to 12.7 mm. Thus, to calculate $\tau_{bu,split}$ the following formula has been used Equation 4-10.

$$\tau_{bu,slip} = \eta_2 (\frac{f_{cm}}{25})^{0.25} (\frac{25}{\emptyset})^{0.2} \left[(\frac{c_{min}}{\emptyset})^{0.33} (\frac{c_{max}}{c_{min}})^{0.1} + k_m k_{tr} \right] \quad \text{Equation 4-10}$$

In which

η_2 = 1.0 for good bond conditions, 0.7 for all other bond conditions

f_{cm} = the mean cylinder concrete compressive strength N/mm2

$\emptyset$ = the diameter of the anchored bar considered [mm] which ourse is 12.7 mm

k_m is considered 0 due to no confining reinforcement and c_{min} and c_{max} are shown in the Figure 3-2

k_{tr} is 0.02

The values of calculated parameters regarding the uncorroded situation are reported in the Table 4-4

$\tau_{bu,split}$	τ_{bmax}	a	S1	S2	S3	Cmin	Cmax	τ_{bf}
MPa	MPa		mm	mm	mm	mm	mm	MPa
7.475099	8.42244	0.4	1.335734	1.335734	1.602881	18.65	43.65	0

Table 4-4 _ Adjusted parameter using the model proposed by MC2010

Consequently, after calculation of the bond stress between concrete and stress and the relative displacement of the strands, the Figure 4-26 shows the bond stress-slip relationship of our sample considering uncorroded situation based on Model Code 2010.

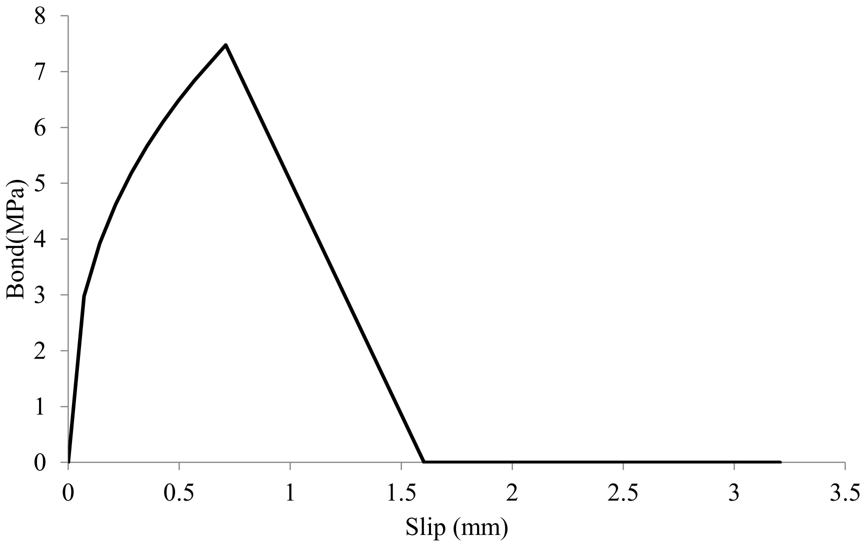

Figure 4-26 _ Bond-Slip relationship adjusted based on MC 2010

4.3.2 Bond Stress vs Slip Relationship Based on The Model Proposed by Wang (Wang, 2023)

In addition to the Model Code 2010 which is more appropriate for the RC elements with ribbed rebar, the bond-slip relationship also based on Wang model has been calculated due to be more adaptable for PC elements with strands which is our case.

The CEB Model Code suggests distribution improvements to reflect the local bond stress-slip relationship between strand and concrete, as shown in Figure 3-18. The bond transfer is divided into three distinct regions: (1) nonlinear increase region until the maximum bond stress, (2) linear decrease region, and (3) constant residual strength region. There is not the plateau over the maximum bond stress. The improved function is also employed to measure the local bond stress-slip relationship between strand and concrete. The observed mechanisms and failure modes can be well described by this improved distribution. First, the initial bond stress depends on the adhesion action. With increasing slip, the adhesion action reduces and the twist friction force and gear force both increase. These forces remain until excessive local slip appears such that the concrete gear shears off. After that, the bond force is only provided by the longitudinal friction force, which is small.

According to CEB Model Code (CEB-FIP 2010), the improved function for the local bond stress-slip relationship can be expressed as Equation 4-11.

$$\tau = \begin{cases} \tau_{max}(\frac{s}{s_2})^{a} & 0 \leq s \leq s_2 \\ \tau_{max} - (\tau_{max} - \tau_f)(\frac{s - s_2}{s_3 - s_2}) & s_2 \leq s \leq s_3 \\ \tau_f & s_3 \leq s \end{cases}$$ Equation 4-11

where

τ_{max} = maximum bond stress

τ_f = residual friction stress

α, s2 , and s3 are constants

For ribbed bars, the maximum bond stress, τ_{max}, is determined by the formulas $1.25\sqrt{f_{ck}}$ for good bond conditions and $2.5\sqrt{f_{ck}}$ for other conditions, where f_{ck} represents the characteristic compressive strength of the concrete. The value of τ_f is then computed as 40% of τ_{max}. The parameters α and s_2 are typically assigned values of 0.4 and 3 mm, respectively, while s_3 denotes the clear distance between the ribs of the bars. As previously noted, the bond behaviour of strands embedded in concrete closely resembles that of ribbed bars. Consequently, the parameters used to describe the local bond features of strands are estimated based on those for ribbed bars. Given that strands do not have ribs, the parameter s3 is defined as half the distance between next wires and the concrete gear, expressed as s_3 = 0.5s_l, where s_l = s_t / sin α, as shown in Figure 3-19 and Figure 3-20. These parameters were applied to the local bond stress–slip model and validated using experimental data. For this model, τ_{max} was set to $1.25\sqrt{f_{ck}}$, and s_3 was assigned a value of 12.0 mm. The situations description explained in detail in section 3.2.4. The mentioned situation, represent the bond-slip relationship proposed by Wang regarding the uncorroded situation. In fact, in our case we had the naturally corrosion and based on the corrosion level we estimated, will be explained in detail in section 4.3.4, the corroded bond-slip relationship has been calculated considering the $\tau_{bmax,corr}$ as 0.55% of the uncorroded case and the parameters and the results of calculations considering the uncorroded case and corroded cases are shown in Table 4-5.

Uncorroded situation					Corroded situation				
τ_{bmax}	a	S1	S2	S3	τ_{bmax}	a	S1	S2	S3
MPa		mm	mm	mm	MPa		mm	mm	mm
8.42	0.4	3	3	12	4.63	0.4	0.7	0.7	5.6

Table 4-5 _ Adjusted parameters in uncorroded and corroded cases using model proposed by Wang (Wang, 2023)

Consequently, after calculation of the bond stress between concrete and strands and the relative displacement of the strands using Equation 4-11, the Figure 4-27 shows the bond-slip relation of our sample based on model proposed by wang (Wang, 2023).

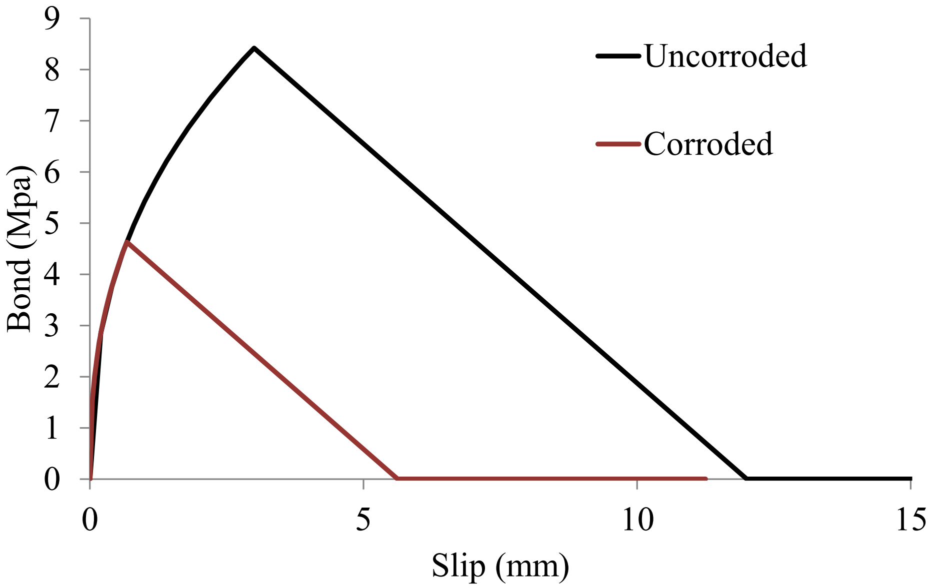

Figure 4-27 _ Bond-Slip relationship adjusted based on model proposed by wang

4.3.3 Transmission Length

The transmission length is a critical factor in analysing the bond properties which is inversely proportional to the bond stress which is a function of radial stress of interface and friction coefficient between concrete and strands. The parameters that play significant roles in terms of transmission length of uncorroded strands could be mentioned as concrete strength, concrete cover, strand diameter, and initial prestressing stress. According to the mentioned factors, (Anaya et al., 2022) suggested a simplified expression to calculate the uncorroded transmission length Lt,0 by Equation 4-12.

$$L_{t,0} = (30\emptyset_{eq,0}(\sigma_{p,0})^{1/2}) / ((c/\emptyset_{eq,0})^{1/3} {f_{cm}}^{2/3}) \qquad \text{Equation 4-12}$$

The transmission length is considerably affected by corrosion level due to loss of the bond capacity between concrete and strands caused by rust product formation and expansion of steel which cause some cracks and damage in the surrounding concrete. (Anaya et al., 2022) suggested also a simplified analytical expression to analyze the corroded transmission length, Equation 4-13, based on the threshold cross-sectional loss rate, Equation 4-14, the corrosion level and the rate of deterioration of transfer length, Equation 4-15, which is represented as a dimension loss factor a_{corr},Equation 4-16.

$$L_{t,corr} = L_{t,0}.\, a_{corr} \quad \text{Equation 4-13}$$

$$X_{lim} = 2250(\emptyset^{1/3}(c/\emptyset)^2)/\ (\sigma_{p,0})^{5/4} \quad \text{Equation 4-14}$$

$$V_{det} = 0.004(\sigma_{p,0}.\, f_c{}^{2/9})/\ \emptyset^{1/3}(c/\emptyset)^3 \quad \text{Equation 4-15}$$

$$a_{corr} = 1 + (X_{corr} + X_{lim}).\, V_{det} \geq 1 \quad \text{Equation 4-16}$$

Using the simplified approach presented, the uncorroded transmission length and corroded transmission length in different levels of corrosion and also the mentioned parameters are calculated regarding our case and shown in Table 4-6 and Figure 4-28.

X_{lim}	12.9	Threshold limit for transfer length	%
V_{det}	0.04	Rate of deterioration of transfer length	%
$L_{t,0}$	627	Uncorroded transfer length	mm
$L_{t,0}/\emptyset_0$	49.4	Uncorroded adimensional transfer length	-
$L_{t,corr}$	627	Corroded transfer length	mm

Table 4-6 _ Transfer length in PC beam

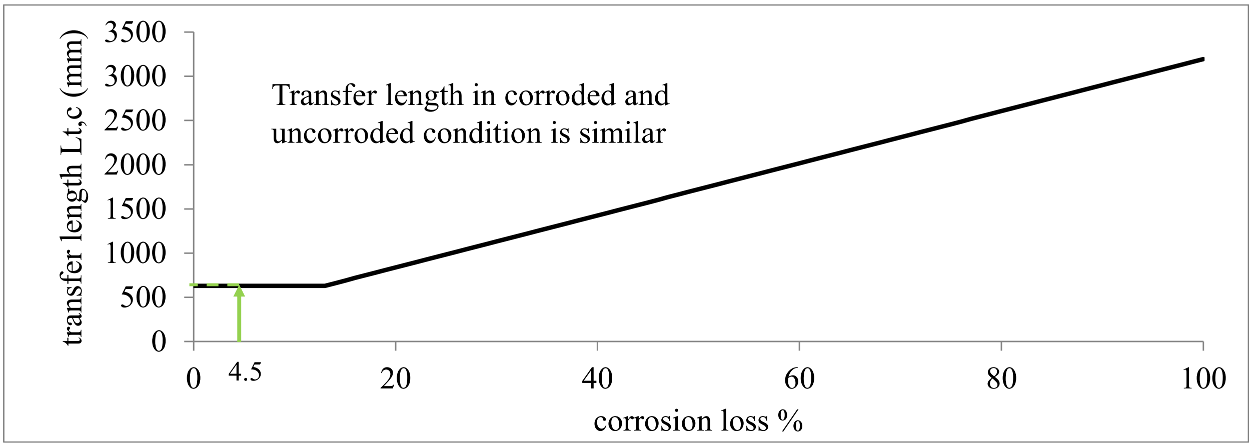

(a)

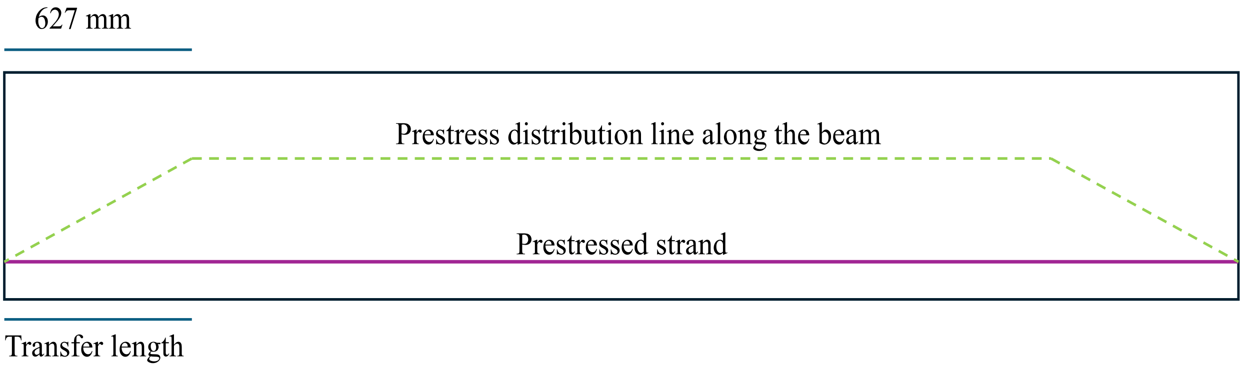

(b)

Figure 4-28 _ (a) Transmission length in the beam considering corrosion level (Anaya et al., 2022), (b) Distribution of the prestress along the beam, the prestress is zero at the beam edge and reaches the maximum after 627 mm

Considering the corrosion level in our case which is 4.5%, will be explained in detail in section 4.3.4, the corroded and uncorroded transfer length has become similar because we are in the unchanged domain which introduced by (Anaya et al., 2022), which proposes that if the corrosion level is less than 13 precent, the transfer length does not increase.

4.3.4 Corrosion Level and Mechanical Behaviour of Corroded Strands

The objective of this section is to estimate the equivalent corrosion level, and the constitutive law of corroded strain based on the available data, including the prestress levels in the strands. As outlined in Section 4.1.1, prior to initiating Test 2, strain gauges were employed to measure the strain in concrete surface in the beam during its relaxation phase and before creation of notch, Figure 4-29a. The beam was in the condition that the self-weight effect disappeared, and the results are shown in Figure 4-29b. Using this data, a back analysis was performed through Nonlinear Finite Element Analysis (NLFEA) to estimate the residual prestress level in the strands, simulating the beam in its relaxation phase before the creation of the notch. In this process, a trial-and-error approach was used to determine the residual prestress level in the strands, ensuring that the strain level at concrete surface obtained from the NLFA, closely matched the experimentally recorded strain at the corresponding point,Figure 4-29c. In the NLFE model, the strain level has been measured in the first modeling step to be sure that the recorded strain level is only because of prestress of strands. The residual prestress level was found to be 602 MPa, corresponding to approximately 55% of the initial prestress in the prestressed concrete (PC) beam.

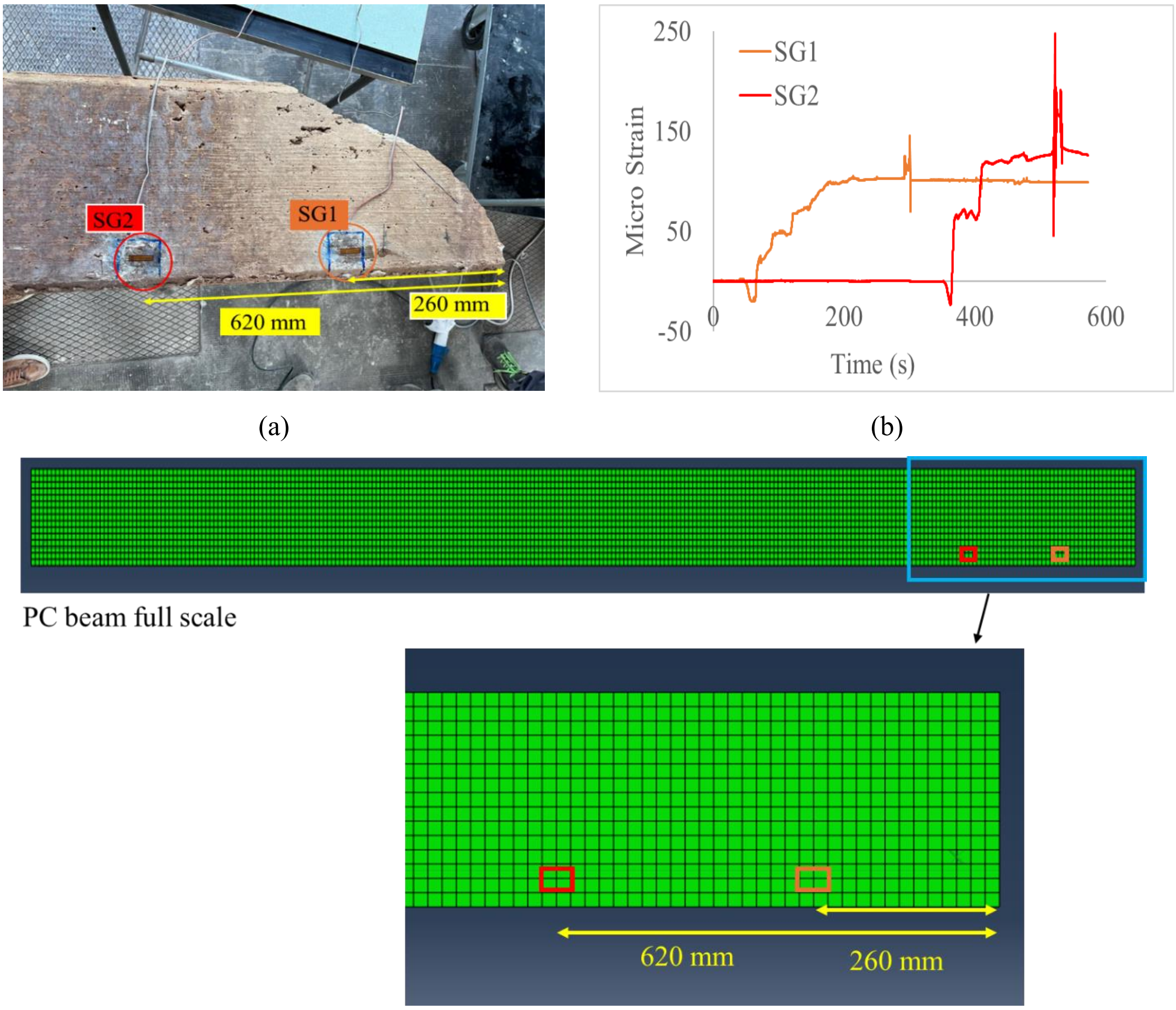

(a) (b)

(c)

Figure 4-29 _ (a) shows the location of two strain gauges used before conducting the second test, (b) shows the experimental result of strain gauges in terms of micro strain, (c) shows the FE elements in which the strains at concrete surface created by applying 55% of initial prestress in the strands recorded, in the relaxation phase before notch creation and without self-weight which was consistent with the experimental data.

Therefore, based on the model introduced by (Ravasini et al., 2023a) the equivalent corrosion level could be obtained. The coefficient R is a function of corrosion level according to cross-section loss and is ratio between corroded prestress and uncorroded prestress of strand, showing in Equation 4-17 which is related to the specimens with splitting failure.

$$\frac{Corroded\ prestress}{Uncorroded\ prestress} = R = e^{-0.133\mu} = 0.55 \qquad \text{Equation 4-17}$$

R is the coefficient

μ is corrosion level %

Then by considering R as 0.55, the equivalent corrosion level could be calculated as follows by Equation 4-18.

$$\mu = \frac{ln(0.55)}{-0.133} = 4.5\% \qquad \text{Equation 4-18}$$

Moreover, based on the graphical representation, the level of corrosion could be estimated by Figure 4-30, in which we are interested in splitting graph due to our failure mode which is splitting. The analyses showed that the level of corrosion before implementing test 2 could be considered as 4.5%.

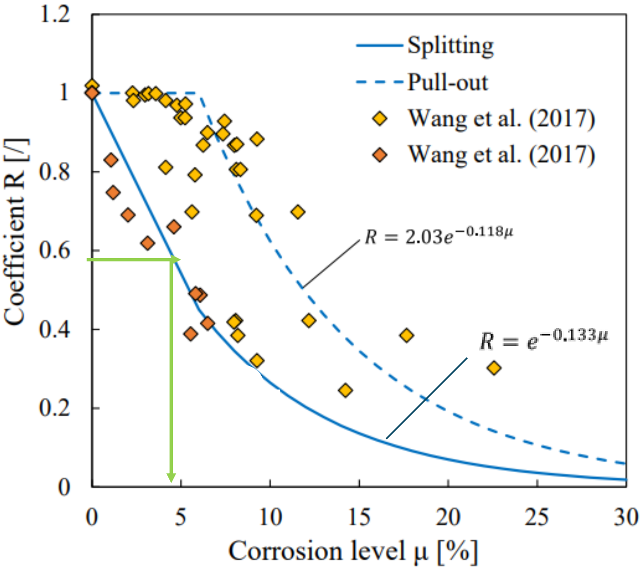

Figure 4-30 _ Corrosion level vs coefficient R (Ravasini et al., 2023a)

Moreover, due to corrosion and cross-section loss in the strand, the constitutive law of strands has been changed. According to the SCPS-model (Franceschini et al., 2023), having the maximum penetration depth in one outer wire, it is possible to estimate equivalent corrosion level. But here, an inverse approach has been applied and by having the equivalent cross-section loss, it is possible to estimate the maximum, Figure 4-31, and average corrosion penetration in outer wires and consequently, the corroded stress-strain relationship could be measured, Figure 4-32.

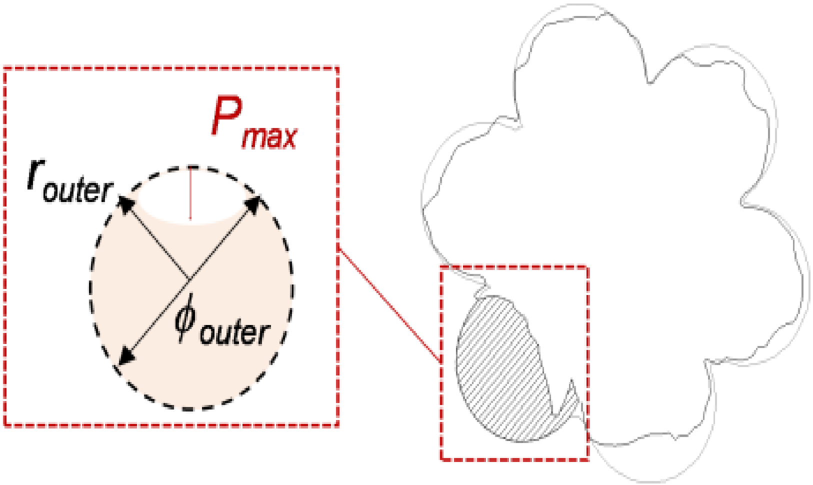

Figure 4-31 _ The maximum penetration depth compared to diameter of the outer wire in the worst case (Franceschini et al., 2023)

In this model, it is assumed that one of the outer wires experienced the most corrosion with the maximum pit depth and other five outer wires experienced the average pit depth like each other while, the inner wire assumed to not have any corrosion. Thus, based on this theory, the initial failure in the strand occurs by failure of the most corroded wires, $\sigma_{w,max}(\varepsilon, P_{max})$, blue. Then, the next break usually occurs by the failure of the other five outer wires simultaneously due to experiencing similar moderate corrosion pit, $\sigma_{w,av}(\varepsilon, P_{av})$, red. And finally, the failure occurs in the inner wire because no corrosion has been assumed for this core wire, green.

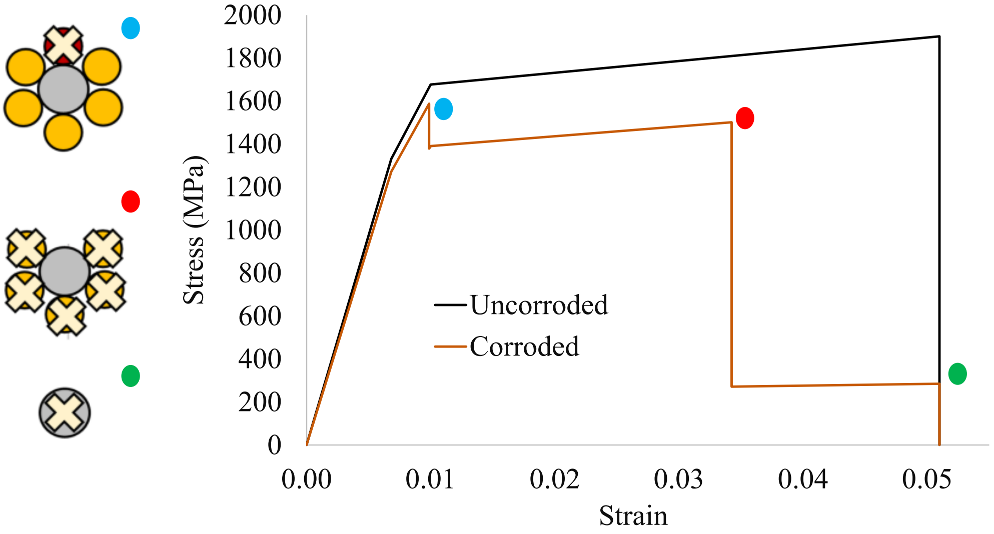

Figure 4-32 _ Stress-Strain relationship of uncorroded strand and corroded strand

The ultimate stress in the corroded wires is defined in the Equation 4-19.

$$\sigma_{w,max}(\varepsilon, P_{max}) = \begin{cases} 0.00 \leq \dfrac{P_{max}}{r_{outer}} < 0.33 & f_{py,0} + E''_{p,0}\left(\varepsilon_{pu,cor} - \varepsilon_{py,0}\right) \quad \varepsilon_{py,0} < \varepsilon_{pu,cor} \leq \varepsilon_{pu,0} \\ 0.33 \leq \dfrac{P_{max}}{r_{outer}} < 0.86 & f_{pp,0} + E'_{p,0}\left(\varepsilon_{pu,cor} - \varepsilon_{pp,0}\right) \quad \varepsilon_{pp,0} < \varepsilon_{pu,cor} \leq \varepsilon_{py,0} \\ 0.86 \leq \dfrac{P_{max}}{r_{outer}} < 2 & E_{p,0}\varepsilon_{pu,cor} \quad \varepsilon_{pu,cor} < \varepsilon_{pp,0} \end{cases}$$

$$\sigma_{w,av}(\varepsilon, P_{av}) = \begin{cases} 0.00 \leq \dfrac{P_{av}}{r_{outer}} < 0.33 & f_{py,0} + E''_{p,0}\left(\varepsilon_{pu,cor} - \varepsilon_{py,0}\right) \quad \varepsilon_{py,0} < \varepsilon_{pu,cor} \leq \varepsilon_{pu,0} \\ 0.33 \leq \dfrac{P_{av}}{r_{outer}} < 0.86 & f_{pp,0} + E'_{p,0}\left(\varepsilon_{pu,cor} - \varepsilon_{pp,0}\right) \quad \varepsilon_{pp,0} < \varepsilon_{pu,cor} \leq \varepsilon_{py,0} \\ 0.86 \leq \dfrac{P_{av}}{r_{outer}} < 2 & E_{p,0}\varepsilon_{pu,cor} \quad \varepsilon_{pu,cor} < \varepsilon_{pp,0} \end{cases}$$

Equation 4-19

And the residual stress of the corroded strand is defined by Equation 4-20.

$$\sigma_{\varepsilon} = \sigma_{w,max}(\varepsilon, P_{max})a_{Acor}$$

Equation 4-20

$$\sigma_{\varepsilon} = \sigma_{w,av}(\varepsilon, P_{av})a'_{Acor}$$

Where:

$$a_{Acor}\left(\frac{P_{max}}{r_{outer}}\right)=$$

$$\begin{cases} \dfrac{P_{max}}{r_{outer}} < 0.33 \\ \dfrac{A_{w,inner} + A_{w,outer}\left[\left(1 - 0.303\dfrac{P_{max}}{r_{outer}}\right) + 5(1 - 0.303(0.378{\dfrac{P_{max}}{r_{outer}}}^{2} + 0.25\dfrac{P_{max}}{r_{outer}})\right]}{A_{strand0}} \\ 0.33 \leq \dfrac{P_{max}}{r_{outer}} < 0.66 \\ \dfrac{A_{w,inner} + A_{w,outer}\left[\left(0.9 - 0.539(\dfrac{P_{max}}{r_{outer}} - 0.33)\right) + 5(1 - 0.303(0.378{\dfrac{P_{max}}{r_{outer}}}^{2} + 0.25\dfrac{P_{max}}{r_{outer}})\right]}{A_{strand0}} \\ \dfrac{P_{max}}{r_{outer}} > 0.66 \\ \dfrac{A_{w,inner} + A_{w,outer}\left[\left(0.9 - 0.539(\dfrac{P_{max}}{r_{outer}} - 0.33)\right) + 5(0.9 - 0.539\left(0.378{\dfrac{P_{max}}{r_{outer}}}^{2} + 0.25\dfrac{P_{max}}{r_{outer}}\right) - 0.33))\right]}{A_{strand0}} \end{cases}$$

$$a'_{Acor}\left(\frac{P_{max}}{r_{outer}}\right) = \begin{cases} \dfrac{P_{max}}{r_{outer}} < 0.66 \\ \dfrac{A_{w,inner} + 5A_{w,outer}\left[1 - 0.303(0.378{\dfrac{P_{max}}{r_{outer}}}^{2} + 0.25\dfrac{P_{max}}{r_{outer}})\right]}{A_{strand0}} \\ \dfrac{P_{max}}{r_{outer}} > 0.66 \\ \dfrac{A_{w,inner} + 5A_{w,outer}\left[1 - 0.539(\left(0.378{\dfrac{P_{max}}{r_{outer}}}^{2} + 0.25\dfrac{P_{max}}{r_{outer}}\right) - 0.33)\right]}{A_{strand0}} \end{cases}$$

$$P_{av} = r_{outer}(0.387\left(\frac{P_{max}}{r_{outer}}\right)^{2} + 0.25\frac{P_{max}}{r_{outer}}$$

$$\varepsilon_{pu,cor} = \left[(1 - 3.03\frac{P_{max}}{r_{outer}})(\varepsilon_{pu,0} - \varepsilon_{py,0})\right] + \varepsilon_{py,0} \qquad 0.00 \leq \frac{P_{max}}{r_{outer}} < 0.33$$

$$\varepsilon_{pu,cor} = \left[(1 - 0.599(\frac{P_{max}}{r_{outer}} - 0.33)\right] \varepsilon_{pu,0} \qquad 0.33 \leq \frac{P_{max}}{r_{outer}} < 2$$

$$E'_{p,0} = \frac{f_{py,0} - f_{pp,0}}{\varepsilon_{py,0} - \varepsilon_{pp,0}}$$

$$E"_{p,0} = \frac{f_{pu,0} - f_{py,0}}{\varepsilon_{pu,0} - \varepsilon_{py,0}}$$

$$A_{w,corr} = \left[(1 - 0.303\frac{P_{max}}{r_{outer}})A_{w,0}\right] \qquad 0.00 \leq \frac{P_{max}}{r_{outer}} < 0.33$$

$$A_{w,corr} = \left[(0.9 - 0.539(\frac{P_{max}}{r_{outer}} - 0.33)A_{w,0}\right] \qquad 0.00 \leq \frac{P_{max}}{r_{outer}} < 2$$

$f_{pp,0}$ is strength in correspondence of the proportional limit

$\varepsilon_{pp,0}$ is strain in correspondence of proportional limit

$f_{py,0}$ is yielding strength

$\varepsilon_{py,0}$ is yielding strain

$f_{pu,0}$ is ultimate strength

$\varepsilon_{pu,0}$ is ultimate strain

The ratio of maximum corrosion (P_{max}) to the outer wire radius (r_{outer}) for the most severely corroded wire and five wires exhibiting average corrosion in our study was determined to be 0.351 and 0.134, respectively. Additionally, the cross-sectional area of the most corroded wire was estimated to be 12.65 mm^2, while the area of the wires with average corrosion depth was calculated at 13.66 mm^2. In comparison, the uncorroded outer wire had an area of 14.25 mm^2. Consequently, the corroded strand diameter was estimated to be 11.05 mm, which was utilized as the corroded strand diameter in section 4.1.3. Furthermore, based on the estimated cross-sectional loss, the transfer length was calculated and discussed in section 4.3.3.

It should be mentioned that as the precise cross-sectional loss and extent of localized corrosion require analysis through advanced technical methods, such as laser scanning, the effort to scan the strands will be done in the future to precisely know the corrosion level and distribution along the strands.

4.4 Numerical Approach

The use of numerical approaches, particularly Nonlinear Finite Element Analysis (NLFEA), plays a crucial role in evaluating the bond strength between steel and concrete in structural engineering. These sophisticated methods allow for comprehensive simulations of the complex interactions that occur between different materials, capturing the detailed nonlinear behaviour of these materials under various loading conditions and environmental influences. This capability is particularly important in understanding the impact of corrosion, which can significantly deteriorate bond strength over time and ultimately compromise the structural integrity of the material. By employing nonlinear FEA, engineers can accurately predict potential failure modes and patterns of degradation that might not be apparent through experimental methods alone. This predictive capability is essential for enhancing the reliability and safety of structural designs, supporting the optimization of material selection, and refining construction processes to create cost-effective and durable engineering solutions. Moreover, these numerical methods are valuable in developing strategies to mitigate the detrimental effects of corrosion, thereby ensuring the longevity and integrity of concrete-steel bonds, especially in challenging environments. Over the past few years, numerous researchers have focused on numerical approaches to model and understand the bond behaviour of reinforcing steel in concrete structures. Through these studies, it has been demonstrated that NLFEA provides a highly accurate representation of both material and structural behaviour. However, the reliability and accuracy of NLFEA outcomes are heavily dependent on the assumptions and parameters set during the modelling process (Belletti, Scolari, et al., 2017). Factors such as material properties, boundary conditions, and the type of load applied can significantly influence the analysis results. Therefore, it is crucial to validate these numerical methods to ensure they provide reliable predictions. One effective way to achieve this is through blind prediction exercises, where different research teams or analysts are asked to predict the outcomes of specific structural tests without prior knowledge of the actual results. By comparing these predictions with the real test outcomes and against each other, the effectiveness and precision of the NLFEA methods can be thoroughly evaluated. This process not only provides insights into the strengths and limitations of various modelling approaches but also fosters a deeper understanding of the behaviour of reinforced concrete under different conditions. Furthermore, it encourages the development of more accurate models and methodologies, enhancing the anticipative power of nonlinear finite element analysis. As a result, NLFEA serves as a powerful tool in the design and analysis of concrete structures, allowing for a more robust assessment of structural performance and the potential for optimization in design and materials usage. This contributes to safer, more efficient, and longer-lasting structures, which is a key objective in civil engineering and construction.

4.4.1 Finite Element Method Software

In this study, numerical modelling was performed using the Finite Element Software ABAQUS. To achieve a more precise representation of the specimen, which includes capturing the intricate material properties, loading conditions, interactions between the concrete and reinforcing strands, and the application of appropriate boundary conditions, a user subroutine (UMAT) was implemented. This approach was chosen over the standard material library available in ABAQUS to enhance the fidelity of the simulation. Specifically, the user-defined material (UMAT) subroutine allowed for the incorporation of the PARC_CL 2.0 crack model, will be described in section 4.4.2, which was used to suit the requirements of this research. The utilization of the UMAT subroutine, in contrast to the predefined material models in ABAQUS, provides a higher degree of flexibility and customization, facilitating the accurate modelling of the complex behaviour of the materials under various loading scenarios. This approach enabled a more detailed simulation of strand-concrete interface, crack propagation and material degradation, which are critical to understanding the performance of the composite specimen under study.

4.4.2 PARC_CL 2.0 Crack Model

The PARC_CL 2.0 model is a crack model developed to describe the behaviour of reinforced concrete elements, explained in detail in (Belletti, Scolari, et al., 2017; Belletti, Stocchi, et al., 2017; Ravasini et al., 2023b). The model integrates more advanced material constitutive relationships to account for plastic deformations. It is designed to consider hysteresis loops and plastic strains during unloading and is executed through the UMAT subroutine for use with the ABAQUS software. This model is particularly suited for analysing the static and dynamic responses of reinforced concrete components, such as slabs, structural walls, buildings, and floors, using multi-layered shell or membrane elements. The PARC_CL 2.0 model employs a fixed crack method according to total strain, characterizing two reference coordinate systems at each incorporation point: the local x,y system and the 1,2 system aligned with the principal stress directions. The edge between the 1-direction and the x-axis is denoted by Ψ, while θ_i represents the angle between the ith bar direction and the x-axis; $a_i = \theta_i - \Psi$ describes the orientation of the ith bar relative to the 1-direction. The first crack forms when the principal tensile strain in the concrete first surpasses the tensile strain limit, $\varepsilon_{t,cr}$, and the 1,2-coordinate system remains unchanged thereafter, as shown in Figure 4-33.

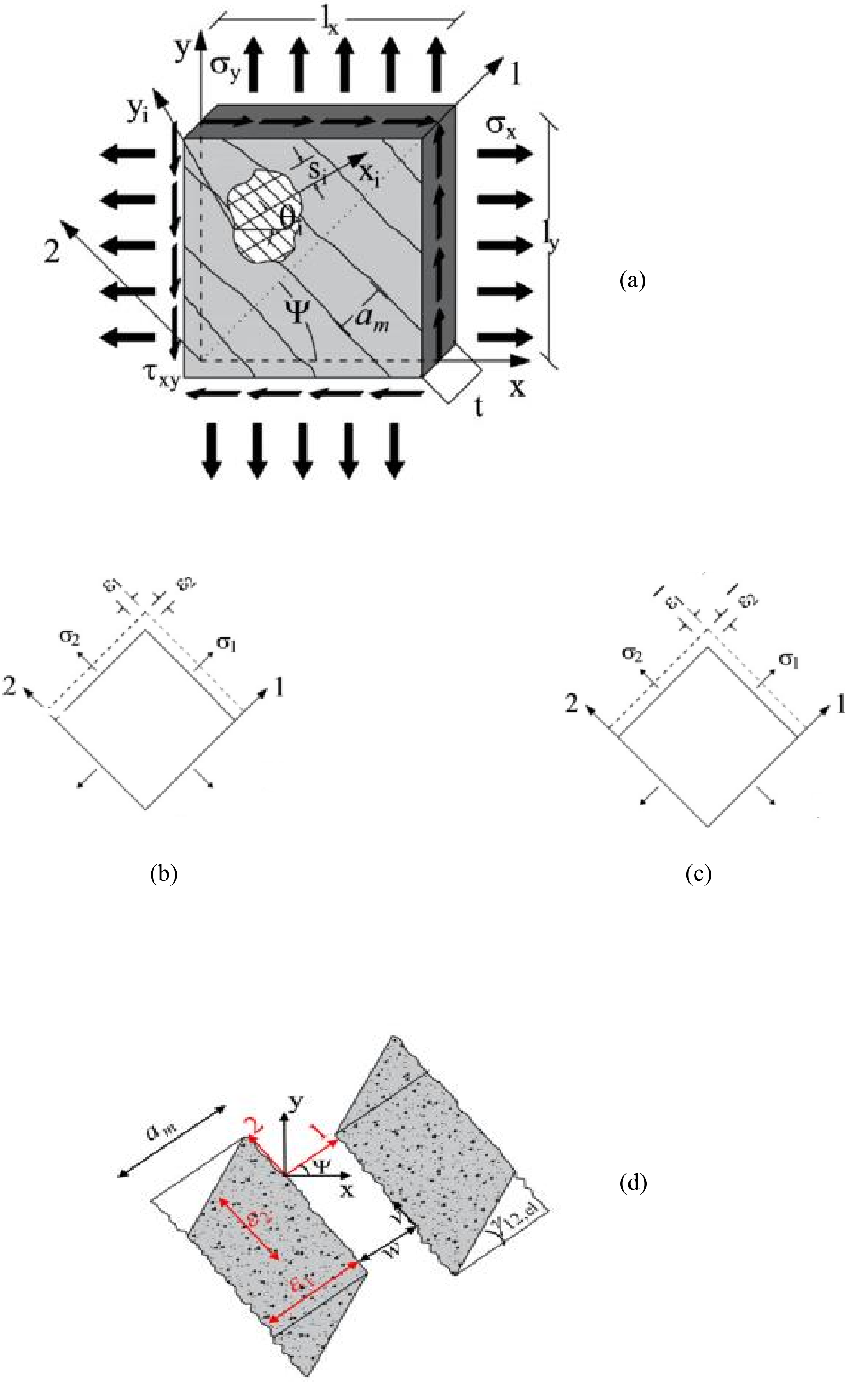
l_x
y
σ_y
1
y_i
σ_x
s_i
x_i
θ_i
2
l_y
Ψ
a_m
τ_xy
t
x
ε1
ε2
σ2
σ1
2
1
ε1
ε2
σ2
σ1
2
1
a_m
2
y
1
Ψ
x
ε2
ε1
v
w
γ12,el

(a)

(b)

(c)

(d)

Figure 4-33 _ (a) reinforced concrete membrane element subjected to plane stress state, (b) biaxial strain situation in system1,2-coordinate. (c) uniaxial strain situation in system1,2-coordinate _ stresses in both directions are about uniaxial strain while demonstrating both uniaxial and biaxial stresses, (d) crack pattern (Belletti, Scolari, et al., 2017).

4.4.2.1 Strain fields

The performance of the concrete is considered orthotropic in nature, both prior to and following cracking. The overall strains at each integration point are determined within the orthotropic 1,2-coordinate system, as shown in Equation 4-21:

$$\{\varepsilon_{1,2}\} = [T_\Psi].\{\varepsilon_{x,y}\}$$ Equation 4-21

$$\{\varepsilon_{1,2}\} = \{\varepsilon_1 \quad \varepsilon_2 \quad \gamma_{12}\}^t$$ Equation 4-22

$$\{\varepsilon_{x,y}\} = \{\varepsilon_x \quad \varepsilon_y \quad \gamma_{xy}\}^t$$ Equation 4-23

$$\varepsilon'_1 = (\varepsilon_1/1 - v^2) + (\varepsilon_2.v/1 - v^2)$$ Equation 4-24

$$\varepsilon'_2 = (\varepsilon_2/1 - v^2) + (\varepsilon_1.v/1 - v^2)$$ Equation 4-25

$$\gamma' = \gamma_{12}$$ Equation 4-26

Where:

$\{\varepsilon_{1,2}\}$ explains the biaxial strain in 1,2 coordinate system Equation 4-22, Figure 4-33b

$\{\varepsilon_{x,y}\}$ explains the biaxial strain in x,y coordinate system Equation 4-23, Figure 4-33b

$[T_\Psi]$ is transformation matrix calculated as shown in Equation 4-27

Equation 4-24, Equation 4-25 and Equation 4-26 explaining the stress-strain performance according to uniaxial strain in the 1,2-reference system, Figure 4-33c. it should be mentioned that when the first crack appears. The poison's ratio to be consider zero, having similar biaxial and uniaxial strain.

$$[T_\Psi] = \begin{bmatrix} cos^2\,\Psi & sin^2\,\Psi & cos\,\Psi.sin\,\Psi \\ sin^2\,\Psi & cos^2\,\Psi & -cos\,\Psi.sin\,\Psi \\ -2cos\,\Psi.sin\,\Psi & 2cos\,\Psi.sin\,\Psi & cos^2\,\Psi - sin^2\,\Psi \end{bmatrix}$$ Equation 4-27

4.4.2.2 Strain field regarding the steel

In finite element modelling, the steel strands positioned at the lower section of the beam are treated as beam elements. Meanwhile, the reinforcing bars placed at the upper section are modelled as being uniformly distributed within the concrete. The strain field of the steel along the reference axis of each bar is calculated by transforming the strains from the x,y-coordinate system, as illustrated in Equation (a).

$$\{\varepsilon_{x_i,y_i}\} = [T_{\vartheta}].\{\varepsilon_{x,y}\}$$

Equation 4-28

$$[T_{\Psi}] = \begin{bmatrix} cos^2\,\theta_i & sin^2\,\theta_i & cos\,\theta_i.sin\,\theta_i \\ sin^2\,\theta_i & cos^2\,\theta_i & -cos\,\theta_i.sin\,\theta_i \\ -2cos\,\theta_i.sin\,\theta_i & 2ccos\,\theta_i.sin\,\theta_i & cos^2\,\theta_i - sin^2\,\theta_i \end{bmatrix}$$

Equation 4-29

Where:

$[T_{\Psi}]$ is transformation matrix

4.4.2.3 Stress fields

The stress field for concrete and steel dedicated regarding each ith order bars x_i, y_i reference system are as following:

$$\{\sigma_{1.2}\} = \begin{Bmatrix} \sigma_1 \\ \sigma_2 \\ \tau_{12} \end{Bmatrix}$$

Equation 4-30

$$\{\sigma_{x_i,y_i}\} = \begin{Bmatrix} \sigma_{x_i} \\ \sigma_{y_i} \\ \tau_{x_i y_i} \end{Bmatrix}$$

Equation 4-31

Where:

σ_1 and σ_2 are the normal stresses in concrete in parallel to directions 1 and 2

τ_{12} shows the shear stress in concrete

σ_{x_i} is the stress parallel to the ith other of steel axis and there are not stress perpendicular to bar axis

4.4.2.4 Global stress field

The stress fields of both concrete and steel can be converted from their local reference systems to the global x, y coordinate system using Equation 4-32 and Equation 4-33.

$$\{\varepsilon_{x,y}\} = [T_{\Psi}]^t.\{\varepsilon_{1,2}\}$$

Equation 4-32

$$\{\varepsilon_{x,y}\} = [T_{\theta_i}]^t.\{\varepsilon_{x_i y_i}\}$$

Equation 4-33

Eventually, the overall stress in the x, y coordinate system is determined via supposing that the concrete and steel act as two parallel springs, as described in Eq. (14).

$$\{\varepsilon_{x,y}\} = \{\varepsilon_{x,y}\} + \sum_{i=1}^{n} \rho_i \{\sigma_{xy}\}_{s,i}$$

Equation 4-34

4.4.2.5 Numerical solution method and stiffness matrix

The introduced PARC_CL 2.0 model utilizes a tangent method, where the Jacobian matrix in the local coordinate system for each material is constructed using derivatives as shown in Equation 4-35 related to concrete and Equation 4-36 related to each ith steel order.

$$[D_{1,2}] = \begin{bmatrix} (\partial\sigma_1/\partial\varepsilon_1)1/(1-v^2) & (\partial\sigma_1/\partial\varepsilon_2)v/(1-v^2) & 0 \\ (\partial\sigma_2/\partial\varepsilon_1)v/(1-v^2) & (\partial\sigma_2/\partial\varepsilon_2)1/(1-v^2) & 0 \\ 0 & 0 & \partial\tau_{12}/\partial\gamma_{12} \end{bmatrix}$$

Equation 4-35

$$[D_{x_i y_i}] = \begin{bmatrix} \partial\sigma_{xi}/\partial\varepsilon_{xi} & 0 & 0 \\ 0 & 0 & 0 \\ 0 & 0 & 0 \end{bmatrix}$$

Equation 4-36

$$[D_{x,y}] = [T_\Psi]^t [D_{1,2}][T_\Psi] + \sum_{i=1}^{n} \rho_i [T_{\theta i}][D_{xi,yi}][T_{\theta i}]$$

Equation 4-37

The stiffness donation of concrete is treated as scant in the softening part, preventing numerical errors. Once the first crack appears, if the poison's ratio is considered as zero, the off-diagonal terms will be zero also. And eventually the global matrix is described in Equation 4-37. Nonlinear cyclic stress–strain relationships for concrete and steel, multiaxial state of stress for concrete and aggregate interlock are explained in detail in (Belletti, Scolari, et al., 2017; Belletti, Stocchi, et al., 2017).

4.4.3 Non-Linear Finite Element Analysis (NLFEA) Description

The specimens were simulated using the Finite Element software ABAQUS, incorporating the UMAT subroutine based on the PARC_CL 2.0 crack model (Belletti, Scolari, et al., 2017; Belletti, Stocchi, et al., 2017; Ravasini et al., 2023b) with the adjustments that made appropriate that code for using in our case. In these simulations, the complete geometry and material properties of the entire beam were accurately modelled, including the beam-end specimen which has been our region of interest, to replicate the conditions of the real experimental setup Figure 4-34a. The fracture energy of concrete G_f which is the energy needed to extend tensile cracks of unit area has been considered based on the model proposed by Model Code 2010 which is a function of mean concrete compressive strength, Equation 4-38.

$$G_f = 73.f_{cm}^{\ 0.18} \qquad \text{Equation 4-38}$$

The specimens were modelled to ensure a comprehensive representation of their properties. The meshing of the specimen was performed using quadratic eight-node elements, each with dimensions of 20 mm x 20 mm. This meshing strategy ensured a uniform distribution of stress and strain throughout the specimen. Given the uniform geometry of the specimen, a quadratic mesh was deemed appropriate for the analysis. The specimens were modelled as membrane elements, which allowed for in-plane deformations while restricting out-of-plane deformations. This approach was chosen to focus on modelling deformations in the direction of the applied load, and as such, shell elements, which would permit out-of-plane deformations, were not utilized in this modelling.

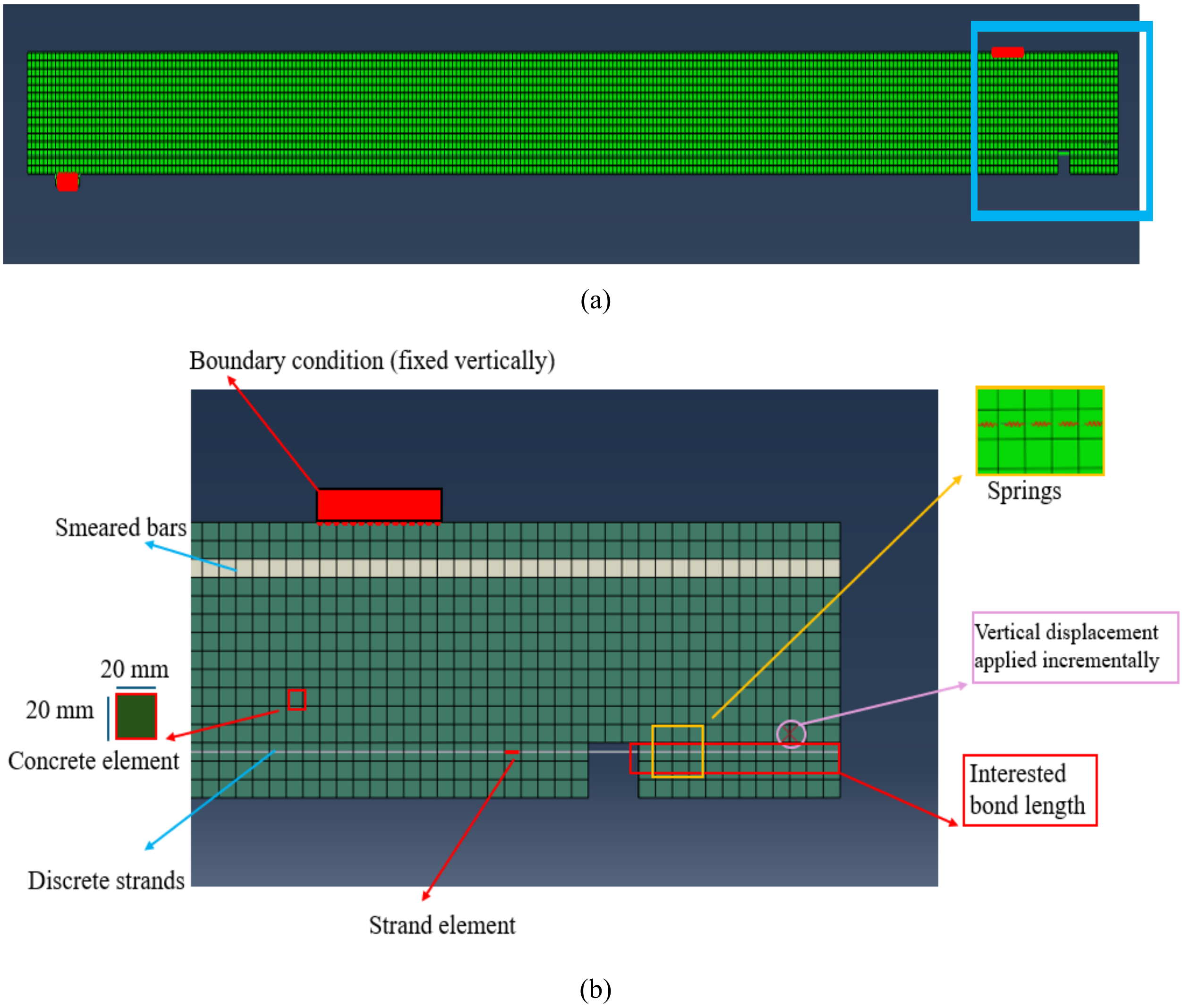

Figure 4-34 : (a) Represent the whole geometry of the PC beam and the blue box is our ROI, (b) Shows the boundary condition, smeared bar type and location, meshing of concrete and discrete strand, springs type and location, interested bond length, position where controlled displacement applied

The simulation process consisted of two primary steps. In the first step, no loading phase was applied, and the notch was not included in the model. In the second step, a notch was introduced, and the loading phase increased gradually, in accordance with the incremental loading hypothesis commonly used in Finite Element modelling. The load was applied as a point load; however, instead of being applied directly to a single node within the specimen mesh, it was distributed across four surrounding elements that were tied together. This approach was employed to prevent sudden failure, which could occur if a specific node detached due to stress localization. For material modelling, concrete and steel were assumed to exhibit elastic-plastic behaviour. The reinforcing bars (rebars) located at the top of the beam were modelled using a smeared approach. In contrast, the strands at the bottom of the beam were modelled as discrete beam elements. The interaction between the strands and the surrounding concrete was simulated by defining springs at intervals of 20 mm. These springs connected the nodes of the strands to the surrounding concrete and were given degrees of freedom parallel to the strand axis to simulate the relative slip between the strands and the concrete, which means that bond was simulated by these springs. Each strand was modelled individually, preserving its actual geometry, position, and diameter, rather than using an equivalent diameter. To accurately represent boundary conditions, only the upper part of the support has been modelled as a fixed support, while the unit weight of the beam has been set to zero, Figure 4-34. Various attempts were made to simulate the boundary conditions, such as modelling both the upper and lower support plates as fixed or simulating the entire support setup by considering the stiffness of the bars connecting the lower support beam, which was fixed to the ground, to the upper plate. The degrees of freedom for the support were determined based on the stiffness of the steel bars Figure 4-2b. However, the most optimal and realistic representation for this prestressed concrete (PC) element was achieved by modelling only the upper plate support by considering the gravity equal to zero. This approach provided a more accurate simulation of the behaviour of the PC element under realistic conditions. Furthermore, the corroded mechanical properties such as the estimated residual prestress level based on experimental data, in detail in section4.3.4, and estimated cross-section loss have been considered in the modeling of corroded condition and the uncorroded mechanical properties of specimen have been considered to model the uncorroded condition.

4.4.4 Non-Linear Finite Element Analysis (NLFEA) Results

Non-Linear Finite Element Analyses (NLFEA) were conducted to provide a more precise analysis of the prestressed concrete (PC) beam. In these analyses, multiple models were developed to investigate how the bond-slip relationship, which is affected by corrosion, influences the behaviour of beam-end specimens. Two models were analysed as uncorroded cases, using material properties and conditions corresponding to uncorroded states. The bond stress and relative slip between the strand and surrounding concrete, used as input data for the NLFEA model, were analytically calculated based on the guidelines provided in Model Code 2010 (Model Code, 2010) and the model proposed by Wang (Wang, 2023). Although the bond-slip relationship model was adjusted to fit our specific case, the calculations followed these established models. The transmission length calculated in Section 4.3.3 was applied to the model for the uncorroded case. Furthermore, one model was analysed using a reduced bond-slip relationship, as input for NLFEA model, which was estimated in Section 4.3.2 based on the model proposed by Wang (Wang, 2023). Another model was analysed using the bond-slip relationship derived from experimental data regarding the right strand in Test 2, while a further model was analysed using the bond-slip relationship based on experimental data for the left strand in Test 2. A final model was developed using the average bond-slip relationship obtained from the experimental data regarding both the right and left strands in Test 2, the bond-slip relationship which obtained in experimental effort presented in detail in section 4.1.3. The flow chart representing the procedure to reach the NLFA models is shown in Figure 4-35

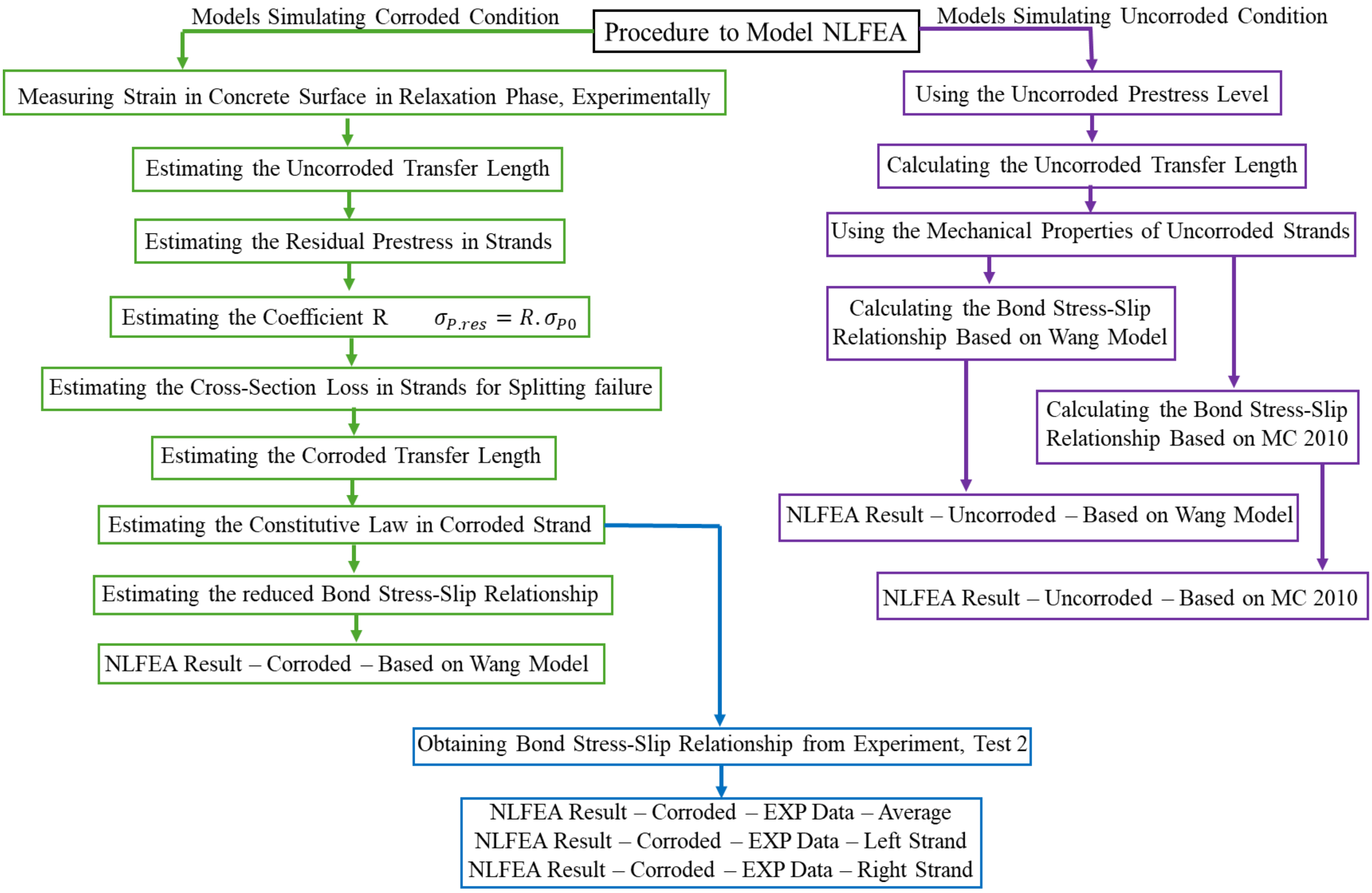

Figure 4-35 _ The flow chart representing the procedure for modelling NLFEA

It is important to note that for the models incorporating the reduced bond-slip relationship and experimental data, other parameters, such as the corrosion level, prestress level, and constitutive law of the strands, were adjusted to reflect the corroded conditions, as estimated in previous sections. The results were extracted and recorded in terms of force versus displacement at the same location where experimental force-displacement data were recorded in Test 2. A comparison between the experimental and numerical results is presented in Figure 4-36.

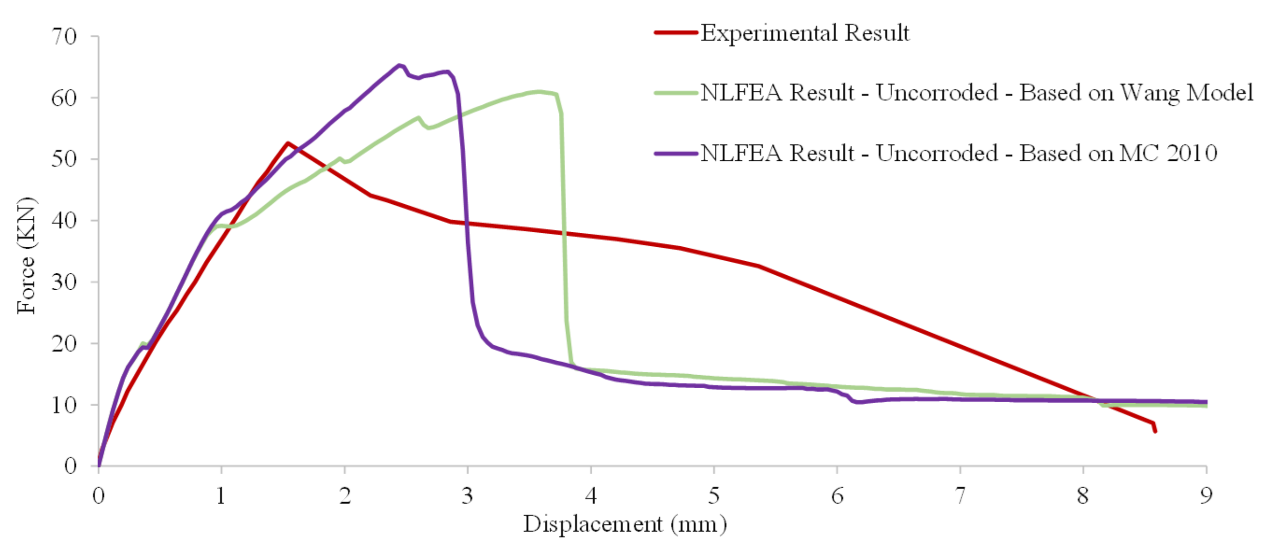

(a)

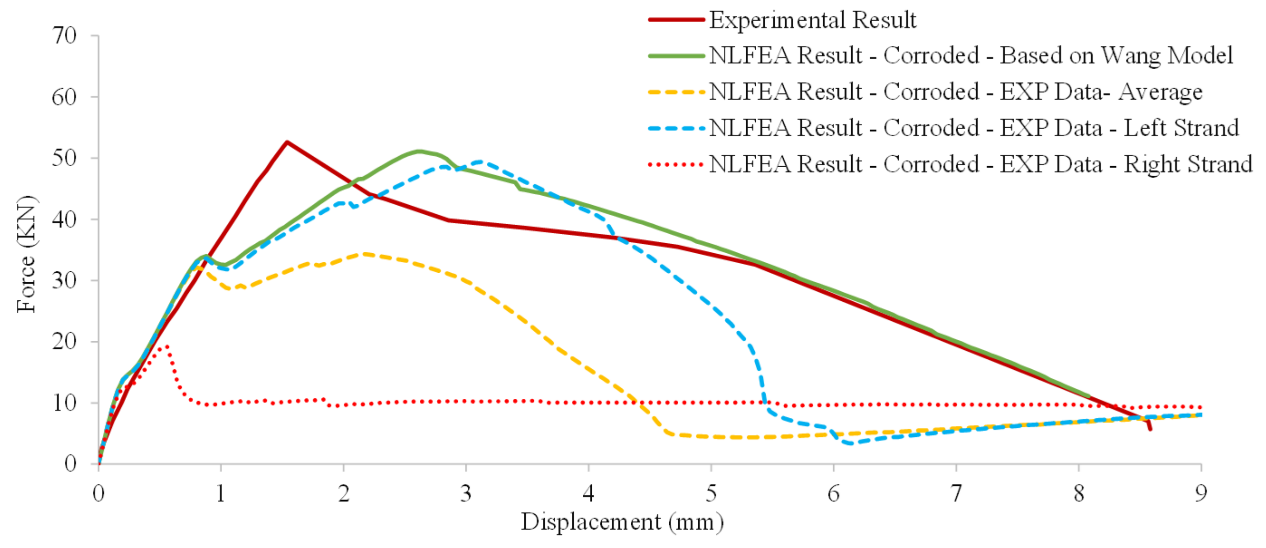

(b)

Figure 4-36 _ (a) Vertical force vs Vertical displacement graph of experimental result from test 2 and NLFA result from modelling the uncorroded PC beam-end specimen according to test 2 setup, (b) Vertical force vs Vertical displacement graph of experimental result from test 2 and NLFA result from modelling the corroded PC beam-end specimen according to test 2 setup considering different bond-slip relationship as input data in modelling

The Figure 4-36 includes several graphs, each corresponding to different experimental and numerical analyses:

The graph titled "Experimental Results" represents the data in terms of vertical force versus vertical displacement relationship at where load applied, Figure 4-37b, obtained from the experiment conducted in Test 2, described in Section 4.2.2.

The graphs titled "NLFEA Result – Uncorroded – Based on MC 2010" and "NLFEA Result – Uncorroded – Based on Wang Model" illustrate the vertical force versus vertical displacement relationship at the loading point, Figure 4-37b. These results are derived from Non-Linear Finite Element Analysis (NLFEA) using the properties of an uncorroded beam. The bond-slip relationship between the strands and the surrounding concrete was calculated based on two models: the Model Code 2010 for uncorroded rebars (Section 4.3.1) and the model proposed by Wang for uncorroded strands (Section 4.3.2). These models were used as input parameters for the analyses.

The graph titled "NLFEA Result – Corroded – Based on Wang Model" presents the vertical force versus vertical displacement data extracted from NLFEA at the same loading point. This analysis incorporates the beam properties estimated in previous sections, which pertain to the corroded beam, including factors such as prestress level, corrosion level, transfer length, and mechanical properties of the corroded strand. Moreover, the reduced bond-slip relationship due to corrosion, as detailed in Section 4.3.2, is modeled according to Wang's approach and applied as input for the analysis.

The graphs titled "NLFEA Result – Corroded – EXP Data – Average", "NLFEA Result – Corroded – EXP Data – Left Strand", and "NLFEA Result – Corroded – EXP Data – Right Strand" represent similar type of results obtained from NLFEA at the same point for the corroded beam. These graphs utilize the corroded beam properties derived in earlier sections, including prestress level, corrosion level, transfer length, and corroded strand mechanical properties. The input bond-slip relationship is applied in three ways: as the average bond-slip relationship obtained for both strands, for the left strand, and for the right strand, based on the experimental data from Test 2, as discussed in detail in Section 4.1.3.

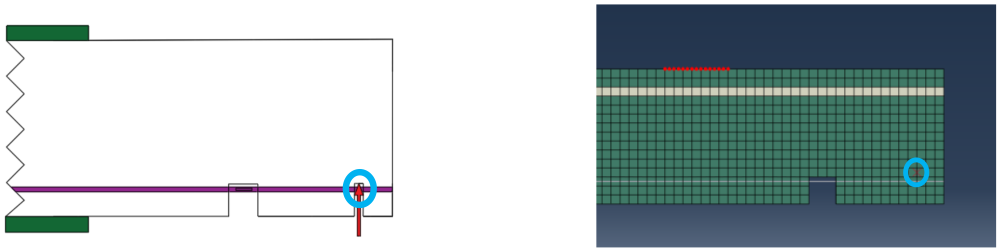

(a) (b)

Figure 4-37 _The blue circle, (a) where the experimental result recorded, (b) where the NLFA results recorded

A comparison between the NLFA results and the experimental data revealed that all models exhibited consistent beam stiffness with the experimental observations up to the creation of the first shear crack. In the uncorroded case, as expected, the NLFA models of the uncorroded beam demonstrated higher ultimate capacity compared to the real corroded prestressed concrete (PC) beam. However, the NLFA models showed more brittle failure. This behaviour is likely due to the beam reaching its threshold capacity, leading to a brittle bond loss at the strand-concrete interface.

In the case of the corroded samples, the model based on the estimated reduced bond-slip relationship closely matched the experimental stiffness before the first shear crack and showed a similar ultimate capacity to the experimental results. Additionally, the NLFA model accurately captured the residual capacity, aligning well with the experimental behaviour.

For the simulation using experimental data from the left strand, the model followed the estimated reduced bond-slip relationship up to the ultimate capacity. However, the residual capacity was slightly lower than that observed in the experimental data. The model based on the average experimental data from both strands showed similar behaviour to the other models before the first crack, but after the crack appeared, it exhibited reduced stiffness, and consequently in lower ultimate and residual capacities.

In contrast, the model using the right strand experimental data failed prematurely, with the ultimate capacity being roughly half of the experimental value. The reduced capacity in this model is attributed to the low bond-slip relationship observed for the right strand. As discussed in Section 4.1.3, this bond-slip relationship was calculated as an estimated equivalent bond using strain gauge data. To improve the accuracy of future analyses, laser scanning will be employed to precisely measure cross-sectional loss and corrosion levels in the strands. Incorporating more accurate data as input to the NLFA will enhance the model's quality. This result highlights the sensitivity of NLFA models to bond strength at the strand-concrete interface, particularly in corroded PC beams.

Furthermore, the crack patterns obtained from the nonlinear finite element analysis (NLFA) have been documented, and the experimental crack patterns have also been recorded using digital image correlation (DIC) analysis. In the Figure 4-38, the initial shear cracks, as well as the progression of shear and splitting cracks at the point of failure in the NLFA, will be presented. Moreover, the shear cracks observed at maximum load capacity and the splitting failure mode will be illustrated.

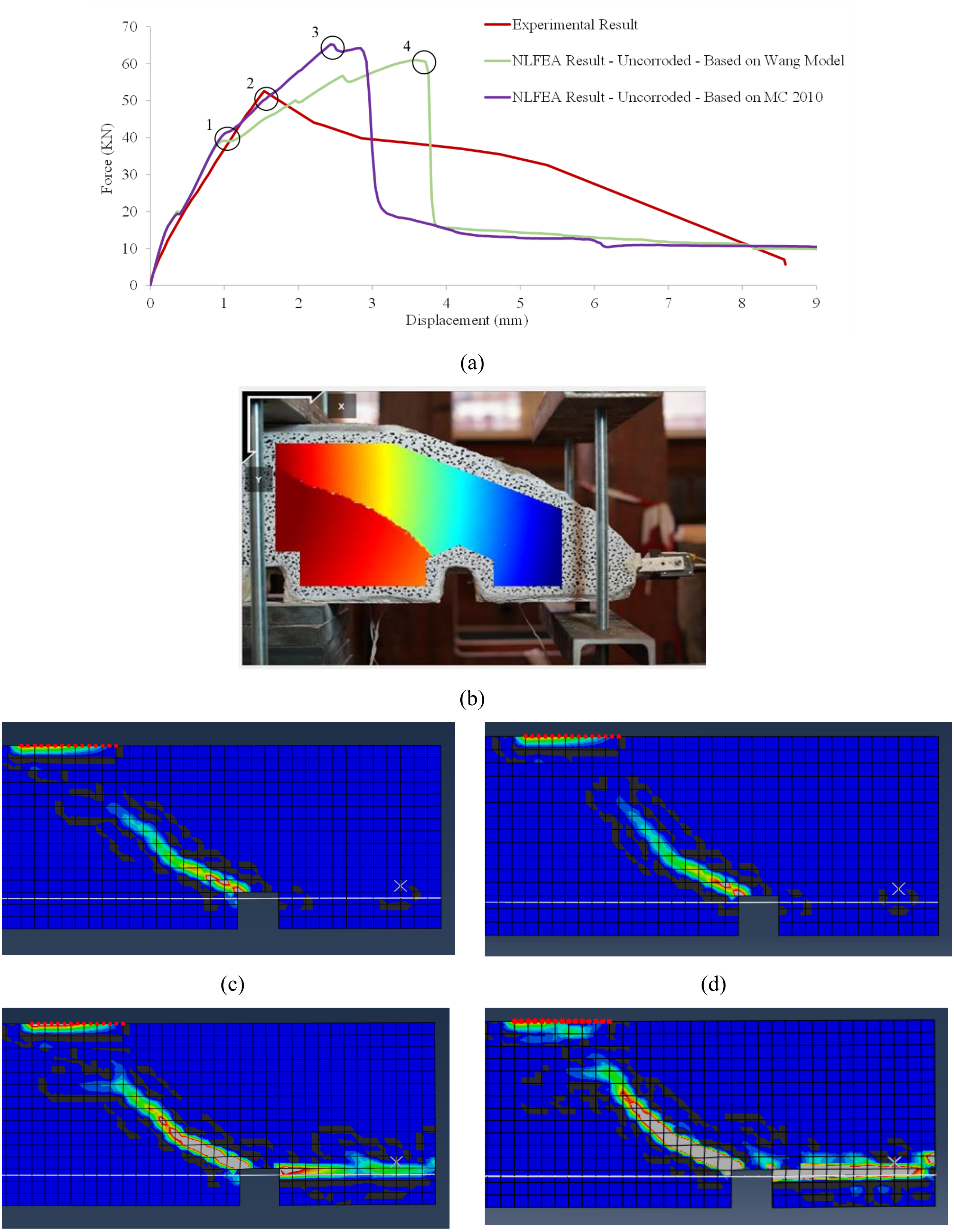
Force (KN)
Displacement (mm)
0
10
20
30
40
50
60
70
0
1
2
3
4
5
6
7
8
9
1
2
3
4
Experimental Result
NLFEA Result - Uncorroded - Based on Wang Model
NLFEA Result - Uncorroded - Based on MC 2010
X
Y

(a)

(b)

(c)

(d)

(e)

(f)

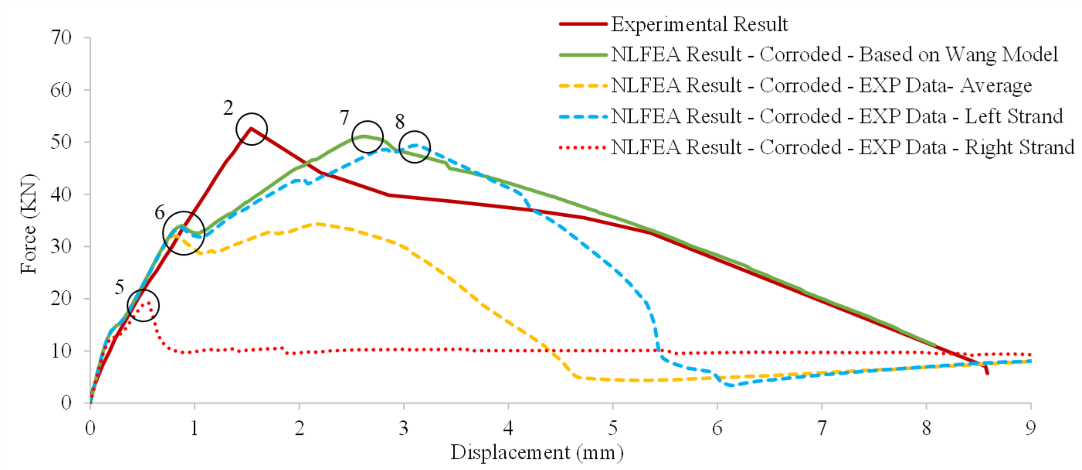
Experimental Result
NLFEA Result - Corroded - Based on Wang Model
NLFEA Result - Corroded - EXP Data- Average
NLFEA Result - Corroded - EXP Data - Left Strand
NLFEA Result - Corroded - EXP Data - Right Strand
Force (KN)
70
60
50
40
30
20
10
0
Displacement (mm)
0
1
2
3
4
5
6
7
8
9
2
7
8
6
5

(g)

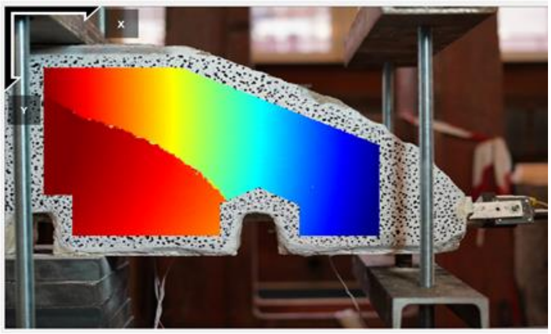

(h)

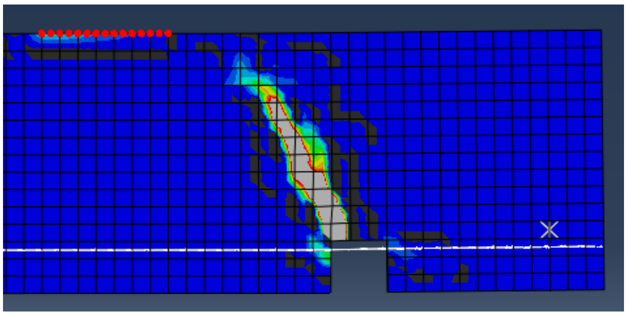

(i)

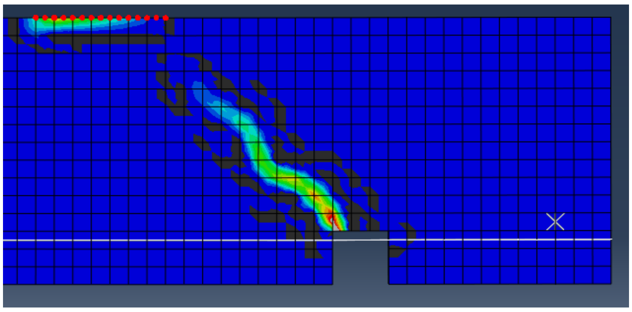

(j)

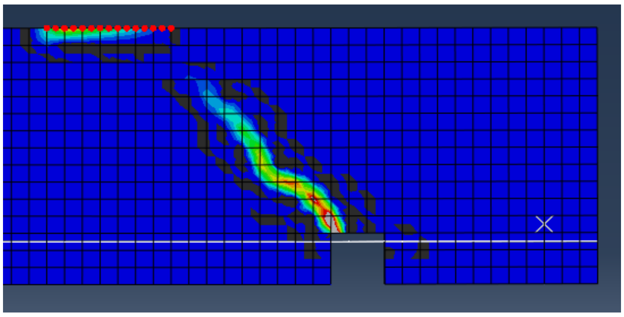

(k)

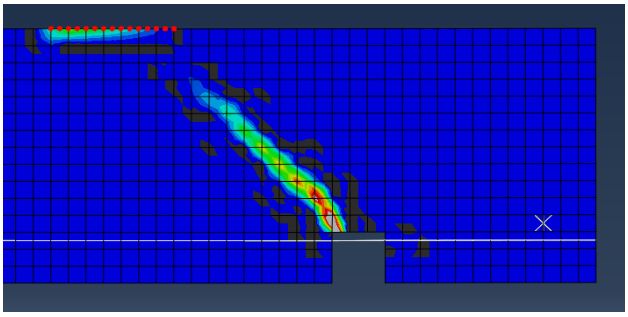

(l)

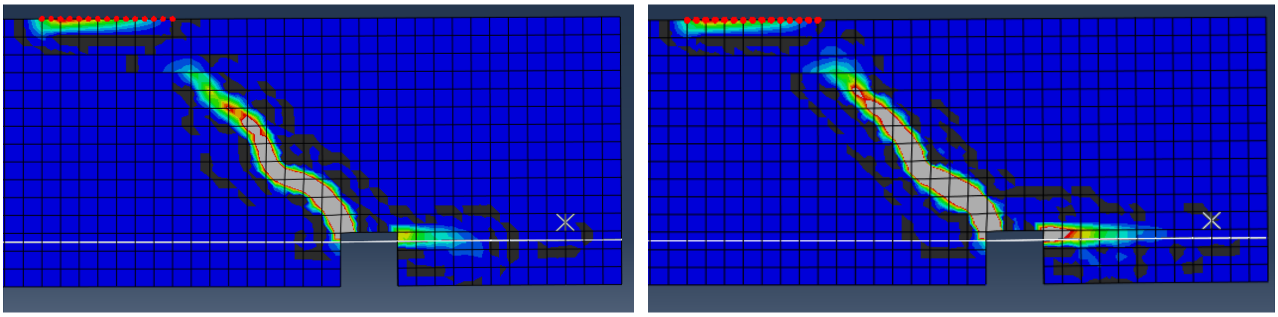

(m) (n)

Figure 4-38 _ (a) Representing the points that cracks recorded in the uncorroded models and experimental DIC, (b) The shear crack recorded by DIC at the maximum load (point 2), (c) The initial shear crack in “NLFA Result – Uncorroded – Based on MC 2010” (point 1), (d) The initial shear crack in “NLFA Result – Uncorroded – Based on Wang Model” (point 1), (e) The shear crack and initial splitting crack at the maximum load in “NLFA Result – Uncorroded – Based on MC 2010” (point3), (f) The shear crack and initial splitting crack at the maximum load in “NLFA Result – Uncorroded – Based on Wang Model” (point 4), (g) Representing the points that cracks recorded in the corroded models and experimental DIC, (h) Similar to (b), (i) Crack at the failure in "NLFA Result – Corroded – EXP Data – Right Strand" (point 5), (j) The initial shear crack in "NLFA Result – Corroded – Based on Wang Model" (point 6), (k) The initial shear crack in "NLFA Result – Corroded – EXP Data – Left Strand" (point 6), (l) The initial shear crack in "NLFA Result – Corroded – EXP Data – Average" (point 6), (m) The shear crack and initial splitting crack at the maximum load in "NLFA Result – Corroded – Based on Wang Model" (point 7), (n) The shear crack and initial splitting crack at the maximum load in NLFA Result – Corroded – EXP Data – Left Strand" (point 8).

The Nonlinear Finite Analysis (NLFA) enabled the identification of the precise moment when the specimen experienced its first crack, a determination that was not possible through Digital Image Correlation (DIC) analysis. This limitation arises because DIC analysis is capable of detecting cracks that appear on the concrete surface, while the initial crack originated internally within the concrete and propagated from the strand-concrete interface. Additionally, as expected, DIC analysis successfully identified the appearance of shear cracks on the concrete surface immediately following the maximum load. Correspondingly, NLFA revealed the presence of shear cracks within the concrete, exhibiting the same inclination as the experimentally observed shear cracks, except for the model "NLFA Result – Corroded – EXP Data – Right Strand," where the inconsistency has been discussed previously. Furthermore, NLFA detected the initiation of splitting cracks, which were also observed through DIC analysis once they reached the concrete surface Figure 4-24. By combination of the DIC analyses and NLFA it could be observed that the cracks start from the strand-concrete interface and with an inclination they reach to the concrete surface. These crack patterns ultimately led to the specimen's splitting failure. It should be also mentioned that by using more advanced techniques such as laser scanner to recognize better the exact cross-section loss and corrosion distribution the NLFA could be improved.

5 Conclusion

This thesis presents results of an experimental campaign conducted at Politecnico di Torino, focusing on three beam-end specimens extracted from a full-scale prestressed concrete beam without stirrups. The beam, which had been in service for over a decade as part of a thermal power plant, experienced repeated cycles of wetting and drying with marine water, leading to natural chloride-induced corrosion.

Devices and instrumentations were used to monitor the strain and relative slip behaviour of the corroded prestressed strands under loading. According to these recordings, the bond strength at the strand-concrete interface and the corresponding bond stress-slip relationship were calculated. Moreover, an analytical bond stress-slip relationship was estimated, considering the level of residual prestress and the cross-sectional loss due to corrosion in corroded strands. Both relationships were further evaluated. Additionally, bond strength considering uncorroded case has been estimated analytically to understand the impact of corrosion on bond behaviour.

The findings clearly demonstrated that corrosion significantly reduces bond strength in Prestressed Concrete (PC) beams, which directly affects their load-bearing capacity. To complement the experimental data, Digital Image Correlation (DIC) technique was employed to monitor displacement distribution on the concrete surface corresponding to each loading step, as well as crack initiation and propagation patterns. Furthermore, Nonlinear Finite Element Analyses (NLFEA) were carried out to simulate the performance of both corroded and uncorroded beam-end specimens, based on the experimental test setup. As expected, the uncorroded models exhibited higher ultimate capacity compared to their corroded counterparts. The NLFEA results showed reasonable agreement with experimental observations in terms of load-bearing capacity and stiffness, demonstrating the detrimental effect of bond degradation on structural performance. Both DIC and NLFEA revealed similar crack propagation patterns, with cracks initiating as shear cracks and progressing to splitting cracks, ultimately leading to splitting failure.

However, it is worth noting that one numerical model, which used experimental data from the right strand in second test, showed reduced consistency with the other results, likely due to insufficient detail in assessing the exact level and distribution of corrosion along the strand.

Future research should focus on more advanced techniques such as laser scanning to obtain more accurate data on corrosion distribution along the strands, especially related to the corrosion morphology. This will enhance the accuracy of both analytical analyses and numerical simulations of bond behaviour and structural performance in corroded Prestressed Concrete (PC) beams.

6 References

Akademia Baru, P., Ghani, A. F. A., Ali, M. B., Dharmalingam, S., & Mahmud, J. (2016). Digital Image Correlation (DIC) Technique in Measuring Strain Using Opensource Platform Ncorr. *Journal of Advanced Research in Applied Mechanics ISSN*, *26*(1), 10–21.

Almusallam, A. A., Al-Gahtani, A. S., Aziz, A. R., & Rasheeduzzafar. (1996). Effect of reinforcement corrosion on bond strength. *Construction and Building Materials*, *10*(2), 123–129. https://doi.org/10.1016/0950-0618(95)00077-1

Anaya, P., Martín-Pérez, B., Rodríguez, J., & Andrade, C. (2022). Transfer length of corroded wires in prestressed concrete members. *Structural Concrete*, *23*(1), 154–171. https://doi.org/10.1002/suco.202100265

Belletti, B., Rodríguez, J., Andrade, C., Franceschini, L., Sánchez Montero, J., & Vecchi, F. (2020). Experimental tests on shear capacity of naturally corroded prestressed beams. *Structural Concrete*, *21*(5), 1777–1793. https://doi.org/10.1002/suco.202000205

Belletti, B., Scolari, M., & Vecchi, F. (2017). PARC_CL 2.0 crack model for NLFEA of reinforced concrete structures under cyclic loadings. *Computers and Structures*, *191*, 165–179. https://doi.org/10.1016/j.compstruc.2017.06.008

Belletti, B., Stocchi, A., Scolari, M., & Vecchi, F. (2017). Validation of the PARC_CL 2.0 crack model for the assessment of the nonlinear behaviour of RC structures subjected to seismic action: SMART 2013 shaking table test simulation. *Engineering Structures*, *150*, 759–773. https://doi.org/10.1016/j.engstruct.2017.07.058

Blomfors, M., Zandi, K., Lundgren, K., & Coronelli, D. (2018). Engineering bond model for corroded reinforcement. *Engineering Structures*, *156*, 394–410. https://doi.org/10.1016/j.engstruct.2017.11.030

Dang, C. N., Murray, C. D., Floyd, R. W., Micah Hale, W., & Martí-Vargas, J. R. (2014a). Analysis of bond stress distribution for prestressing strand by Standard Test for Strand Bond. *Engineering Structures*, *72*, 152–159. https://doi.org/10.1016/j.engstruct.2014.04.040

Dang, C. N., Murray, C. D., Floyd, R. W., Micah Hale, W., & Martí-Vargas, J. R. (2014b). Analysis of bond stress distribution for prestressing strand by Standard Test for Strand Bond. *Engineering Structures*, *72*, 152–159. https://doi.org/10.1016/j.engstruct.2014.04.040

de Assis, E. B., & Evangelista Junior, F. (2017). Development of Digital Image Correlation tool to determine displacements and strains in mechanical testing. *Proceedings of the XXXVIII Iberian Latin American Congress on Computational Methods in Engineering*, *February*. https://doi.org/10.20906/cps/cilamce2017-1207

Focacci, F., Nanni, A., & Bakis, C. E. (2000). Local Bond-Slip Relationship for FRP Reinforcement in Concrete. *Journal of Composites for Construction*, *4*(1), 24–31. https://doi.org/10.1061/(asce)1090-0268(2000)4:1(24)

Franceschini, L., Belletti, B., Tondolo, F., & Sanchez Montero, J. (2023). A simplified stress–strain relationship for the mechanical behaviour of corroded prestressing strands: The SCPS-model. *Structural Concrete*, *24*(1), 189–210. https://doi.org/10.1002/suco.202200170

Hanjari, K. Z., Coronelli, D., & Lundgren, K. (2011a). Bond capacity of severely corroded bars with corroded stirrups. *Magazine of Concrete Research*, *63*(12), 953–968. https://doi.org/10.1680/macr.10.00200

Hanjari, K. Z., Coronelli, D., & Lundgren, K. (2011b). Severely corroded reinforced concrete with cover cracking: Part 2. anchorage capacity. *RILEM Bookseries*, *5*, 207–216. https://doi.org/10.1007/978-94-007-0677-4_14

Li, F., & Yuan, Y. (2013). Effects of corrosion on bond behaviour between steel strand and concrete. *Construction and Building Materials*, *38*, 413–422. https://doi.org/10.1016/j.conbuildmat.2012.08.008

Li, H., Yang, Y., Li, C. H., Wang, X., & Tang, H. (2024). A new analytical model for bond strength between corroded steel strand and concrete. *Scientific Reports*, *14*(1), 1–14. https://doi.org/10.1038/s41598-024-62763-z

Lundgren, K. (2005a). Bond between ribbed bars and concrete. Part 1: Modified model. *Magazine of Concrete Research*, *57*(7), 371–382. https://doi.org/10.1680/macr.2005.57.7.371

Lundgren, K. (2005b). Bond between ribbed bars and concrete. Part 2: The effect of corrosion. *Magazine of Concrete Research*, *57*(7), 383–395. https://doi.org/10.1680/macr.2005.57.7.383

Lundgren, K., & Gylltoft, K. (2000). Model for the bond between concrete and reinforcement. *Magazine of Concrete Research*, *52*(1), 53–63. https://doi.org/10.1680/macr.2000.52.1.53

Lundgren, K., Kettil, P., Hanjari, K. Z., Schlune, H., & Roman, A. S. S. (2012). Analytical model for the bond-slip behaviour of corroded ribbed reinforcement. *Structure and Infrastructure Engineering*, *8*(2), 157–169. https://doi.org/10.1080/15732470903446993

Lundgren, K., Robuschi, S., & Zandi, K. (2019). Methodology for Testing Rebar-Concrete Bond in Specimens from Decommissioned Structures. *International Journal of Concrete Structures and Materials*, *13*(1). https://doi.org/10.1186/s40069-019-0350-3

Lundgren, K., Tahershamsi, M., Zandi, K., & Plos, M. (2015). Tests on anchorage of naturally corroded reinforcement in concrete. *Materials and Structures/Materiaux et Constructions*, *48*(7), 2009–2022. https://doi.org/10.1617/s11527-014-0290-y

Mancini, G., & Tondolo, F. (2014). Effect of bond degradation due to corrosion - A literature survey. *Structural Concrete*, *15*(3), 408–418. https://doi.org/10.1002/suco.201300009

Martí-Vargas, J. R., Serna, P., & Hale, W. M. (2013). Strand bond performance in prestressed concrete accounting for bond slip. *Engineering Structures*, *51*, 236–244. https://doi.org/10.1016/j.engstruct.2013.01.023

McCormick, N., & Lord, J. (2010). Digital image correlation. *Materials Today*, *13*(12), 52–54. https://doi.org/10.1016/S1369-7021(10)70235-2

Miano, A., Bernardi, P., Calcavecchia, B., Iacovazzo, P., Mele, A., Ravasini, S., Safabakhsh, A., Ludovico, M. Di, Prota, A., & Belletti, B. (2024). *SEISMIC FRAGILITY CURVES ASSESSMENT OF CORRODED R.C. BRIDGES*.

Micozzi, F., Poeta, A., Gioiella, L., Natali, A., Celati, S., Mazzatura, I., Salvatore, W., Meoni, A., Ierimonti, L., Venanzi, I., Ubertini, F., Ranaldo, A., D'Amato, M., Cattaneo, S., Pettorruso, C., Quaglini, V., Rossi, D., Titton, M., & Dall'Asta, A. (2023). SAFOTEB project: towards new approaches for the reliability assessment of existing prestressed bridge. *Ce/Papers*, *6*(5), 43–48. https://doi.org/10.1002/cepa.2193

Model Code. (2010). *fib Model Code for Concrete Structures 2010*.

Puppio, M. L., Sassu, M., & Safabakhsh, A. (2023). Damage and restoration of historical urban walls: literature review and case of studies. *Frattura Ed Integrita Strutturale*, *17*(65), 194–207. https://doi.org/10.3221/IGF-ESIS.65.13

Ravasini et al. (2023a). *Ravasini, Franceschini, Belletti - 2023 - Simplified analytical method for moment-curvature response of corroded prestressed concrete(2)*.

Ravasini, S., Vecchi, F., Belletti, B., & Muttoni, A. (2023b). Verification of deflections and cracking of RC flat slabs with numerical and analytical approaches. *Engineering Structures*, *284*. https://doi.org/10.1016/j.engstruct.2023.115926

Rinaldi, Z., Imperatore, S., & Valente, C. (2010). Experimental evaluation of the flexural behaviour of corroded P/C beams. *Construction and Building Materials*, *24*(11), 2267–2278. https://doi.org/10.1016/j.conbuildmat.2010.04.029

Safabakhsh, A. (2024). *Pushover analyses of existing bridges subjected to scouring effect*.

Safabakhsh, A., Ravasini, S., Belletti, B., Bernardi, P., Michelini, E., Miano, A., Mele, A., Iacovazzo, P., Di Ludovico, M., & Prota, A. (2024). *SEISMIC VULNERABILITY ASSESSMENT OF EXISTING REINFORCED CONCRETE BRIDGES*.

Sarhan, M. M., Hadi, M. N. S., & Teh, L. H. (2018). Bond behaviour of steel plate reinforced concrete beams. *Construction and Building Materials*, *189*, 751–756. https://doi.org/10.1016/j.conbuildmat.2018.09.024

Syll, A. S., Aburano, T., & Kanakubo, T. (2021). Bond strength degradation in concrete cracked by expansion agent filled pipes. *Structural Concrete*, *22*(5), 3156–3172. https://doi.org/10.1002/suco.202000764

Syll, A. S., & Kanakubo, T. (2022). Residual bond strength in reinforced concrete cracked by expansion agent filled pipe simulating rebar corrosion. *Case Studies in Construction Materials*, *17*. https://doi.org/10.1016/j.cscm.2022.e01565

Wang, L. (2023). *Strand Corrosion in Prestressed Concrete Structures*. https://doi.org/https://doi.org/10.1007/978-981-99-2054-9

Wang, L., Yi, J., Zhang, J., Jiang, Y., & Zhang, X. (2017). Effect of corrosion-induced crack on the bond between strand and concrete. *Construction and Building Materials*, *153*, 598–606. https://doi.org/10.1016/j.conbuildmat.2017.07.113

Zandi, K., & Lundgren, K. (2015). *Concrete-Innovation and Design, fib Symposium*.

Zhang, R., Castel, A., & François, R. (2009). Serviceability Limit State criteria based on steel-concrete bond loss for corroded reinforced concrete in chloride environment. *Materials and Structures/Materiaux et Constructions*, *42*(10), 1407–1421. https://doi.org/10.1617/s11527-008-9460-0

Zheng, Y., Zheng, S. S., Yang, L., Dong, L. G., & Zhang, Y. B. (2022). Experimental study and analytical model of the bond behaviour of corroded reinforcing steel bars in concrete. *Construction and Building Materials*, *327*(February), 126991. https://doi.org/10.1016/j.conbuildmat.2022.126991

Zhu, W., François, R., Coronelli, D., & Cleland, D. (2013). Effect of corrosion of reinforcement on the mechanical behaviour of highly corroded RC beams. *Engineering Structures*, *56*, 544–554. https://doi.org/10.1016/j.engstruct.2013.04.017